Prompt Photons in Photoproduction using the ZEUS detector at HERA

Joanna Hamilton McKenzie

Dept. of Physics & Astronomy

University of Glasgow,

Glasgow

July 2005

Submitted as part of the requirements for the degree of

Doctor of Philosophy

Abstract

Measurements have been made of prompt photons in photoproduction at the ZEUS detector at HERA. Cross sections are presented for the inclusive and photon plus jet processes using the full HERA-I dataset, a total of 121 pb^{-1}. The statistics-based background subtraction is improved by the use of real photons from a Deeply Virtual Compton Scattering process, which allow for more accurate modelling of the behaviour of photons in the detector without contamination from neutral mesons. In the photon plus jet process, the cross sections with respect to E_T^{jet} and η^{jet} are presented for the first time at ZEUS in the photoproduction regime. Comparisons are also made to a suggested new method which relies on the Barrel Presampler to remove background from neutral mesons, and which may provide a means of extending the analysis to regions with prohibitively low statistics under the current method.

For Dave

and for my family:

Mum, Dad, Gillian, Andrew, Stephen and Catherine.

Thesis Outline

Chapter 1 provides a brief introduction, beginning with a brief description of the development of particle physics. An outline of the prompt photon process and the reasons for study is given, and finally the two possible methods for selecting prompt photon events are outlined.

Chapter 2 deals with the theory necessary for an understanding of this thesis. A brief introduction is given, followed by a brief description of the kinematics of electron proton, *ep*, scattering, and the kinematics of the HERA set-up. The quark parton model and QCD, the theory which governs the strong force, are introduced. Finally, prompt photon processes are described and recent research in the field of prompt photons is discussed.

In Chapter 3, the HERA ring and experiments are described, before moving on to a detailed discussion of the ZEUS detector set-up where relevant to the current analysis. The calorimeter and tracking systems are described, as is the trigger system.

Chapter 4 describes the Monte Carlo programs used in the analysis. An introduction is given first to event generators in general and then to PYTHIA and HERWIG, the specific event generators used in this analysis. Details about the PYTHIA, HERWIG and single-particle Monte Carlo samples used are given. The detector simulation through which the simulated events must pass is then described, as is the method for calculating acceptance corrections. Efficiencies and purities for the measurement are presented.

In Chapter 5, the method of selecting prompt photon events and the precise cuts used are described. The ZEUS-standard programs used in the analysis are described, after which each cut in the analysis is described in detail. The photon, jet and y_{JB} correction routines are also described in detail in this chapter.

In Chapter 6, the method by which the neutral meson background is removed from the signal is detailed, including a description of the processes forming the background and corrections applied. The use of Deeply Virtual Compton Scattered photons is described, and the possibility of using the barrel presampler discussed. Finally the completed subtraction method is summarised.

Chapter 7 contains the results from the inclusive prompt photon analysis. The acceptance corrections are displayed, followed by an analysis of the systematic errors. The cross sections are then presented and compared to Monte Carlo samples. Comparisons are also drawn to the previous ZEUS analysis.

Chapter 8 contains the results of the photon plus jet analysis in a similar structure to Chapter 7. In this chapter, the second selection method is described and a comparison is made to the results from that analysis, as well as to the Monte Carlo samples.

Chapter 9 concludes the analyses.

Appendix A provides a summary of work done by a team of ZEUS physicists in order to identify and remove the causes of large amounts of radiation in the ZEUS detector after the HERA upgrade of 2000-2002, focussing particularly on work by the CTD team including the author, and its relevance to the overall effort.

Appendix B provides an in-depth description of the π^0 correction method, which is new to this analysis.

Acknowledgements

In life as well as in research, nothing is done in isolation. It would be impossible to list everyone who has played a part in the years which have culminated in this thesis, and without whom I could never have come this far.

My gratitude goes firstly to my supervisors, Peter Bussey and David Saxon. Between them they have been invaluable guides throughout the progress of this analysis, and their wisdom and experience has been indispensable.

The Glasgow group based at ZEUS over the past four years were my first port of call throughout my time in Hamburg. Therefore I'd like to thank all the members of the Glasgow ZEUS group over the past three years: Anna Lupi, Claudia Glasman, Mairi Bell, and Stephen Hanlon, who have all now left the group, and the current group members, James Ferrando and Billy Dunne, in the latter case for reminding me how far I've come since the beginning of my time at ZEUS. To members of the Glasgow PPE group, who were my assistance in times of trouble when working at Glasgow, my gratitude, especially to Morag Buron-Lyon, Andrew Pickford and Andrew MacGregor.

Further thanks must go to the wider ZEUS-UK group. Firstly to Richard Hall-Winton and Mark Sutton, from whom I learned my first lessons about the HERA accelerator, the detectors, the politics and the people, and particularly the ZEUS software setup. Both were also invaluable when it came to the CTD, whether it was background studies, on-call work and general maintenance, or the DQM shifts. The UK postgrads and postdocs were my contact with civilisation, my friends, and, sometimes, my sole link with sanity for the 18 months I was in Hamburg. To Claire for cheerful assistance even under pressure, to Tim for entertainment, to John for selfless giving, to Eileen, Andrew and Heidi for music, to Jo for girlie nights, to Chris for sci-ed assistence, to James for interesting nights out, and to Matt, Matt, Sunil and

Chris. Mention must also go to Susan Ketels, an ever-cheerful assistant when dealing with a strange land became too much.

The QCD group at ZEUS were a constant reminder that somewhere after all programs have been de-bugged and all mistakes and misunderstandings have been rectified, physics can be done. The QCD group was also the place where I could truly experience the multi-national nature of ZEUS, and make friends from outside the UK.

To Mum and Dad, for putting up with me when things are hard as well as when they're good, for taking my mail when I moved away and providing a bed when I returned, for keeping in touch, for worrying when I was ill, and for providing news of all at home. For Gillian, for allowing me to share your room when I returned, and for helping me to deal with a certain crisis involving a mobile phone. For Andrew, for visiting me in Hamburg, and for Stephen and Catherine, for, if nothing else, never forgetting me, even when I was a long time out of sight. To my extended family: I love you all, and I will never and have never forgotten you, even if I may not have spoken to you for a while.

Finally, thanks go to Dave. It was hard, sometimes, but we managed it. Here's to success in your research and to a long and happy life together.

Contents

List of Figures

List of Tables

Chapter 1

Introduction

Studying the universe has been a preoccupation for mankind since records began. The earliest civilisations studied astronomy, often having the ability to predict astronomical events with impressive accuracy. Recent times have brought technological achievements that our early ancestors could never have dreamed of, and naturally our quest to understand the universe has taken advantage of these achievements. The launch of the Hubble Space telescope allows astronomers to view the cosmos without the distorting effects of our atmosphere, while high energy accelerators such as HERA, LEP and the Tevatron have provided unprecedented insights into the very small. Electronics are being used to greater effect, and computing power has revolutionised the way science works. This is, perhaps, best seen in the field of particle physics, where supercomputers and networks have, in recent years, taken the place of photographic film and human eyes.

1.1 Introduction to particle physics

At the turn of the last century, Rutherford's scattering experiment successfully advanced our understanding of the structure of the atom by scattering alpha particles from gold foil. Modern High Energy Physics (HEP) experiments use the same principle to probe matter on ever-smaller scales: the higher the energy an experiment can reach, the smaller the scale at which matter can be examined.

Synchrotron accelerators accelerate charged particles to high energies. These, along with fixed target experiments–in which a material to be studied is placed in the path of a beam of high-energy particles–provide data on matter, increasing our understanding of how matter interacts under these conditions. The first synchrotron accelerators to provide collisions between high energy particles used electrons and positrons. These leptons are fundamental and cannot be further divided into smaller particles, which gives rise to very clean events in which the initial state is well-defined.

Synchrotron accelerators can also accelerate hadrons. These are non-fundamental, being made up of constituent *partons*. It is these which take part in many interactions, not the hadron, and the initial state may therefore carry any fraction of the momentum of the incoming hadron. The information gained from such experiments, along with the study of cosmic ray interactions and solar neutrinos, for example, has been compiled into the very successful Standard Model of particle physics.

More details about the theory of the strong force and the Standard Model are given in chapter 2.

1.2 Introduction to ZEUS and HERA

The Deutches Elektronen SYnchrotron or DESY laboratory is situated in Hamburg, Germany. Among other facilities, DESY provides the Hadron-Elektron Ring Anlage, or HERA, a unique synchrotron accelerator which provides collisions between hadrons and leptons, in this case between protons and electrons or positrons.

Hadrons are composite particles, whereas leptons have no known substructure. The high mass of the hadrons allows HERA to reach higher centre-of-mass energies than would be possible with just a lepton beam, while the leptons provide a clean, well-understood probe of the hadrons. This unique set-up has allowed HERA to provide significant data on the structure of the proton, providing invaluable aid to future hadron colliders such as the Tevatron in Chicago and the LHC, currently under construction in Switzerland.

There are four experiments situated around the HERA ring. HERA-B and HERMES are nuclear physics experiments, which insert probes into the HERA beams. At H1 and ZEUS, the two beams are brought into collision, providing *ep* interactions for study.

ZEUS is situated in HERA's south hall. The name ZEUS refers both to the detector and to the collaboration of physicists who work there. The detector itself is large, over three stories high, and consists of a variety of different individual detectors which each respond to a different property of an incident particle. Most notable are the tracking detectors, in which the path of a charged particle may be determined, and the calorimeter, which responds to the energy of a particle regardless of whether or not it carries charge. A complex computing system is used to combine the output from each detector into an overall picture of an event.

Further details of the detector are given in chapter 3, along with more information about the HERA facility at DESY.

1.3 Introduction to prompt photons

A great problem with the study of hadronic matter is that we cannot observe a free quark, since individual quarks are always bound into a composite particle. When a quark is released from the proton by the interaction with the lepton beam, it very quickly begins the process of hadronisation in which other hadrons are drawn around it, forming a *jet* of particles. Although it is made up of many particles, the particles remain essentially collinear, making it difficult for a detector to resolve the details of the particles in the jet. For that reason, jets are often treated as single entities.

A prompt photon event is an event in which a high-E_T photon emerges directly from the lepton-proton scatter. Because it emerges cleanly as a singly-produced particle, a prompt photon provides a direct probe of the underlying interaction. We can observe the product of the interaction itself, without the blurring which is observed in multi-particle jets.

While identifying events with the photon signature is fairly straightforward in principle, the method is complicated by background to the prompt photon process. Neutral mesons, notably the π^0, can decay to photons and produce a similar signal in the detector to a prompt photon event. These mesons contaminate the signal of prompt photon events, and for the analysis to truly measure prompt photons they should be removed.

It is not possible to remove such events by placing a direct cut on the data. Still, their contribution is much reduced by requiring that the observed photons be well isolated from all other energy sources in the calorimeter. It is then further reduced by studying the shape of the observed shower in the calorimeter. Since neutral mesons decay to multiple photons, their signal appears to be noticeably wider and less peaked in one spot than a prompt photon signal. By modelling this difference using simulated photons and neutral mesons, a statistics-based subtraction may be used to provide values for the number of prompt photon events. The full method is described in detail in chapter 6.

The results for the prompt photon analysis are presented through a measurement of the 'cross section'. Any dependence on the detector set-up is removed by a process of corrections based on Monte Carlo simulations. This allows comparisons to be drawn between results taken with different detectors.

This thesis deals with two prompt photon analyses. The inclusive prompt photon analysis makes no requirement on any content of the event except that a prompt photon is seen in the detector. In this case, the cross sections are measured with regard to the transverse energy of the photon, E_T^γ, and the pseudorapidity of the photon, η^γ, where

$$\eta = -\log\tan\theta/2 \tag{1.1}$$

Pseudorapidity is a measure of angle, and is chosen such that a negative η means that the particle is detected in the rear of the detector, while a positive value occurs in the forward region. ZEUS defines the forward direction as the direction of the proton beam provided by HERA.

The second prompt photon analysis considered here is of a photon accompanied by a jet. In this analysis, the requirement is made that one jet which satisfies certain energy and angle criteria is found in the detector alongside the photon. Events which contain two or more such jets are rejected. There are four cross sections which are measured for this process. As in the inclusive case, the cross sections may be measured with respect to E_T^γ and η^γ. It is also possible to measure them with respect to the jet variables, E_T^{jet} and η^{jet}, representing, as before, the transverse energy and pseudorapidity.

Cross section measurements at HERA are generally measured in picobarns, pb^{-1}, and are represented by $d\sigma/dX$, where X represents the variable with which the cross section is varying, in this case E_T or η for the photon or jet.

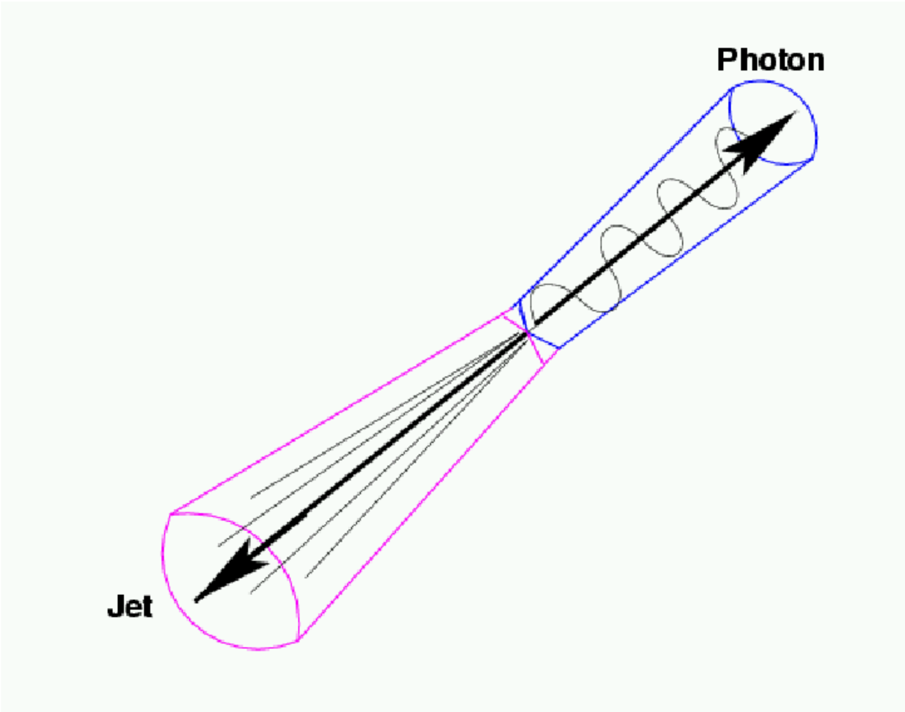

Figure 1.1: The 'dijet' method of selecting prompt photon events uses a jet-finder to find dijet events. One of the two jets is then required to look like a photon: it should be mostly contained in the electromagnetic calorimeter and contain no tracks. The shower shape method finds the photon and jet independently, using an electron finder to locate the photon and a jet finder for the jet.

1.4 Selection methods for prompt photon events

The method for selecting prompt photon events at HERA experiments is as follows. After a basic event selection which ensures an inclusive photoproduction (or DIS) event sample, an electron finder is run without a track requirement. This selects electromagnetic clusters in the calorimeter. Electrons and positrons are then removed by a no-track veto. Background subtraction of other events that may generate an acceptable signal, such as the photon decay from neutral mesons, are reduced firstly by an energy-based isolation requirement which uses a cone in $\eta - \phi$, and secondly by an off-line subtraction process, described in more detail in chapter 6.

There have been some concerns raised in the past that the cone algorithm used to ensure the energy isolation of the photon from this method is not infrared safe; that is, the emission of very soft particles can affect the result of the algorithm. Although it may be possible to use a variation on the K_T jet algorithm, described in section 5.7.1, which is infrared safe due to the modulation of the cone according to the transverse momentum of the jet (or photon), to ensure the isolation of the photon, this is not straightforward and is yet to be used in a published analysis.

To attempt to get round this problem, a new method of selecting prompt photon events has been proposed by my ZEUS colleagues [1]. Instead of using an electron finder, the new method uses the K_T algorithm to select a 'photon jet' [1], that is, a photon selected by a jet finder, as illustrated by figure 1.1. By placing cuts on the 'jet' to ensure that most of the energy is neutral and electromagnetic, this algorithm can be used to select electromagnetic clusters in an infrared-safe way. However, this method also collects neutral electromagnetic clusters due to neutral mesons and their decays, and the details of this analysis method do not allow for the same background subtraction based on shower shapes as the previous method. Instead, the new ZEUS Barrel Presampler is used in an effort to remove these background events.

This reliance on the Barrel Presampler (BPRE: see section 3.6.2) restricts this new method to data gathered after 1999, since that is when the BPRE was installed. Further, this method is only useful for the photon + jet analysis, it cannot be used for an inclusive sample due to its reliance on an initial dijet selection. It is also true that using the BPRE cannot entirely remove the background, it can only reduce the dominance of the background events. Therefore

[1] The term 'photon jet' is used to refer to the object identified by the jet finder and displaying the characteristics of a photon candidate. It is not intended to imply that the photon has the characteristics of a jet, as a true prompt photon consists of just one particle.

any cross-section measured using the dijet method includes a contribution from π^0's, an effect which will be particularly important at low-E_T.

On the other hand, the statistical subtraction which is necessary for the shower shape analysis restricts the range of the analysis to where there are sufficient statistics. At high E_T, for example, the statistics prevent the shower shape method from drawing reliable conclusions. The dijet method may allow the analysis of prompt photon events to be taken into regions such as this where statistics are severely limited. A comparison with the older analysis method is vital to ensure that the two methods are consistent.

Chapter 2

Theory

2.1 Introduction

The progress of particle physics over the past century or so is recorded in the development of the so-called Standard Model of particle physics. In the Standard Model, the particles which exist may be described in terms of matter and force. Matter is split into hadronic and leptonic particles, each of which are susceptible to different forces. The four forces are the strong and weak nuclear forces, electromagnetism and gravity. It is postulated that the most basic action of a force occurs by means of a gauge boson, which interacts with a specific property of a given particle.

The four fundamental forces each act on a different property of matter. The strong nuclear force acts on *colour*, which is possessed by hadrons, including the *gluons* which mediate the strong force. Hadronic matter is composed of quarks, which usually carry a colour charge. Quarks cannot be observed singularly, but only combined into hadrons, bound into colour-neutral particles by the gluons which mediate the strong force. The electromagnetic force acts on the charge of a particle. It is mediated by the *photon*, which is itself charge-neutral.

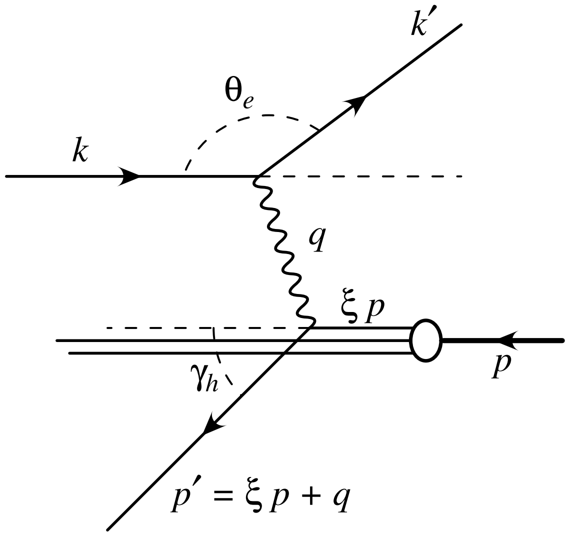

Figure 2.1: The kinematics of neutral current Deep Inelastic Scattering (DIS) at HERA.

The theory which describes the action of the electromagnetic force is Quantum Electro-Dynamics, or QED. Quantum ChromoDynamics, QCD, was developed from this theory and describes the action of the strong force. However, QCD is necessarily more complex than QED due to the possibilities for gluon self-coupling which arise from the bare fact that gluons possess colour, while photons, which are neutral, do not possess charge and therefore cannot interact. QCD and QED are described in more detail in the later sections of this chapter.

2.2 *ep* scattering

In the HERA environment, electrons or positrons are collided with protons. In this asymmetric case, the interaction, which can be either electromagnetic or weak, can be approximated to a leptonic probe of the proton. Figure 2.1 shows a typical HERA scattering process. In the case where the incoming lepton and proton have momenta k and p and are scattered to momenta k' and p' respectively, it is clear that the transferred boson has momentum $q = k - k'$. We define the *virtuality* Q^2 of the exchanged boson to be the negative of the square of the transferred momentum, that is

$$Q^2 = -q^2 = -(k - k')^2 \tag{2.1}$$

In cases where Q^2 is low, neutral current events $ep \to e + X$ are dominated by electromagnetic events in which the gauge boson is a low-virtuality photon. These events are known as *photoproduction* events, and are described in more detail in Section 2.7. In photoproduction events, the exchanged photon is nearly real. Numerically, these events dominate physics events at ZEUS.

Events with high Q^2 also occur. *Neutral current events* are events mediated by neutral bosons, which can be either a highly virtual photon or a Z^0, the massive neutral mediator of the weak force. At high Q^2 there can also occur charged current events $ep \to \nu_e + X$. These events are mediated by the charged bosons which carry the weak force, the W^+ and W^-.

The scatter between the lepton and the proton is largely a scattering at low Q^2, in which case the exchanged photon does not cause the proton to split up. High Q^2 events are termed Deep Inelastic Scattering, and in these events one quark or gluon can be resolved from the proton.

Low Q^2 inelastic events numerically dominate the events seen at HERA. Such events are termed ‘photoproduction’ events. In these, the interaction is mediated by a photon which is nearly real in nature, and the electron is not significantly deflected by the emission of the photon. As the main topic of this thesis, such events are described in further detail in section 2.7.

So-called 'diffractive' events have been extensively observed both at HERA and at hadron colliders. In diffractive scattering, the proton is almost undeflected during the course of the event, and no proton-remnant is observed in the detector. Detailed discussion of diffractive theory is not relevant to this analysis, however it is mentioned here to provide some background to the discussion of Deeply Virtual Compton Scattering events (see chapter 6).

2.3 HERA kinematics

It is possible to describe electron-proton scattering in terms of two variables, x and Q^2, where Q^2 is as defined in equation 2.1 and x is the Bjorken scaling variable, defined as

$$x = \frac{Q^2}{sy},$$

where s is the ep centre of mass energy squared,

$$s = (k + p)^2 = 4E_e E_p,$$

and y is the fraction of energy transferred to the proton from the lepton,

$$y = \frac{p.q}{p.k}.$$

In the above equations, as in section 2.2, k and p represent the initial momenta of the lepton and proton respectively, while k' is the final-state 4-momentum of the lepton.

The invariant centre of mass energy of the hadronic final state, W, may be defined via its square as follows

$$W^2 = (p + q)^2 = m_P^2 - Q^2 + 2p.q \tag{2.2}$$

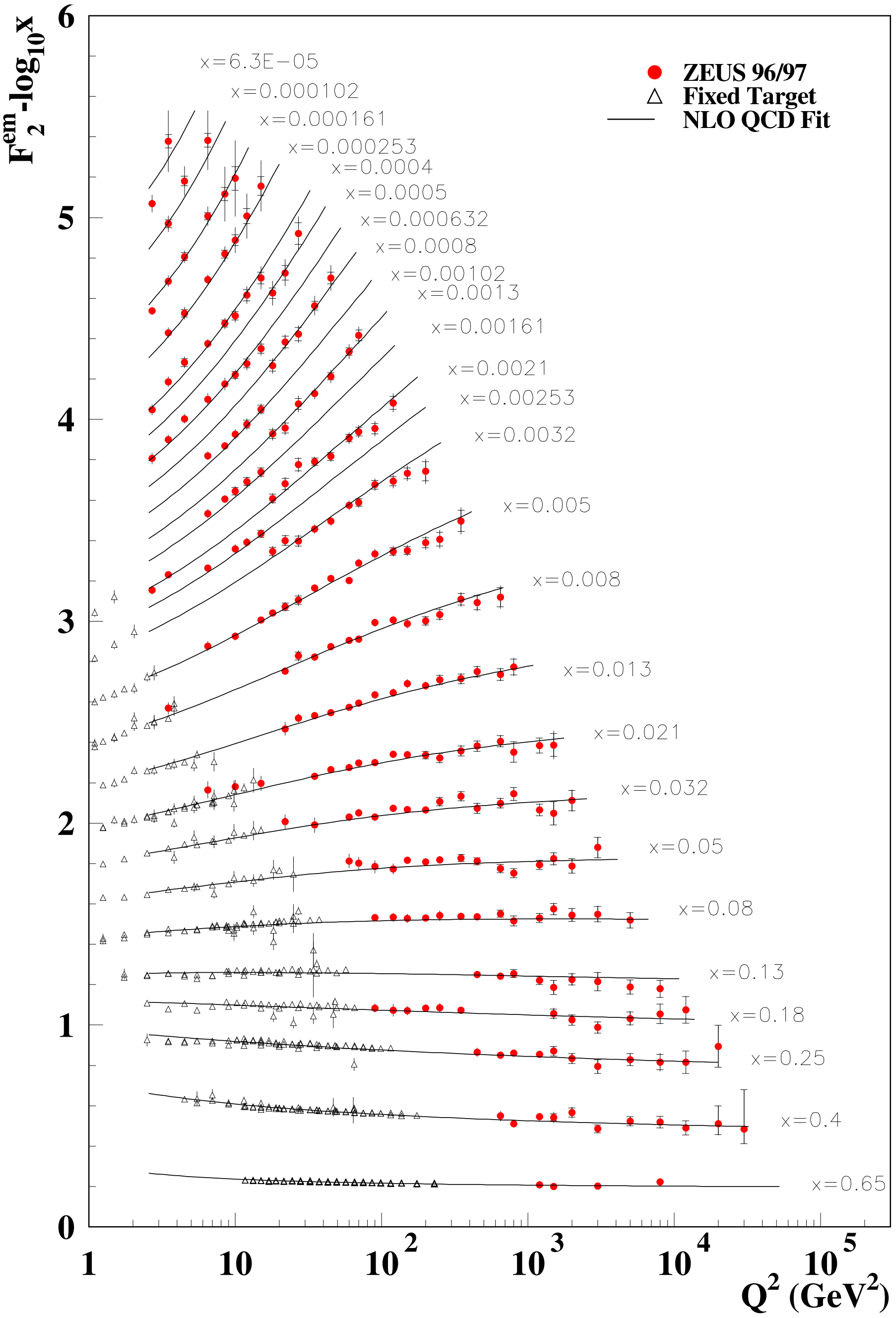

Figure 2.2: Experimental results showing F_2 versus Q^2 with the ZEUS NLO QCD fit shown. In the plot, x is fixed at the various values shown. The black points are results from the fixed-target experiments NMC, BCDM5, and E665, and the red points are from ZEUS [2].

2.4 The DIS cross section and structure function

The cross section for Deep Inelastic Scattering (DIS) can be represented as

$$d\sigma^{ep} = L_{\mu\nu} W^{\mu\nu}$$

where $L_{\mu\nu}$ is the leptonic tensor and $W^{\mu\nu}$ the hadronic.

The leptonic component is independent of the hadronic component, and is entirely calculable within Lowest Order, LO, QED:

$$L_{\mu\nu} = 2\left[k'_\mu k_\nu + k'_\nu k_\mu + \frac{q^2}{2} g_{\mu\nu}\right]$$

Here, $g_{\mu\nu}$ is the metric tensor, and the above form assumes that the mass of the electron is negligible, that is that $Q^2 >> m_e$.

In the photoproduction regime $Q^2 << M^2_{W,Z^0}$, and the interaction between the proton and the electron can be approximated to the purely electromagnetic case of a photon transfer with negligible contribution from weak bosons. In this case, the hadronic tensor $W^{\mu\nu}$ can be parametrised by two functions W_1 and W_2. We then define the proton structure functions F_1 and F_2 as

$$F_1(x, Q^2) \equiv m_P W_1(\nu, Q^2)$$

$$F_2(x, Q^2) \equiv \nu W_2(\nu, Q^2)$$

where $\nu = p.q/m_P$ is the photon energy in the rest frame of the proton. The ZEUS result showing the variation of F_2 with Q^2 is shown in figure 2.2.

These can now be used to write the DIS cross section $ep \to eX$ as

$$\frac{d^2\sigma^{ep}}{dxdQ^2} = \frac{4\pi\alpha^2}{xQ^4}\left[\frac{y^2}{2}F_1(x, Q^2) + (1-y)F_2(x, Q^2)\right]$$

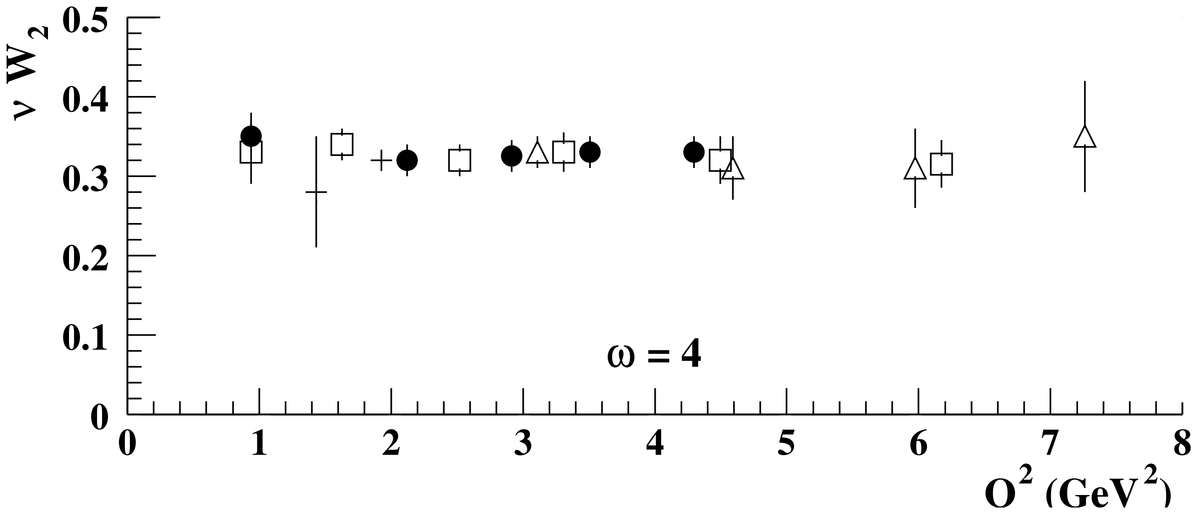

Figure 2.3: Results from SLAC demonstrate that the behaviour of F_2 tends to νW_2 and has no variation with Q^2 (on the x-axis). The results are given at $\frac{1}{\omega} = x = 0.25$. Plot modified from [3].

It is common to define the longitudinal structure function F_L as $F_L = F_2 - 2xF_1$, which allows the cross section to be re-written as

$$\frac{d^2\sigma^{ep}}{dxdQ^2} = \frac{2\pi\alpha^2}{xQ^4}\left[(1+(1-y)^2)F_2 + 2(1-y)F_L\right]$$

2.5 The quark parton model

The naïve Quark Parton Model, QPM [4], assumes that the proton is composed of point-like particles or partons. The transverse momentum which may be carried by these partons is neglected, and it is assumed that each parton carries a fraction ξ of the proton momentum in the longitudinal direction. This results in the Bjorken scaling variable x becoming equivalent to the momentum fraction ξ.

Bjorken predicted that in the limit $Q^2 \to \infty$ and $\nu \to \infty$, the cross section would depend solely on a dimensionless scaling variable, x. This was later confirmed by SLAC, as shown in figure 2.3 for the case of W_2.

In the QPM, the structure function F_2 depends on the sum of the contribution from the individual partons, so that, where the charge of parton i is indicated by e_i,

$$F_2(x, Q^2) = F_2(x) = \sum_i e_i^2 x f_i$$

$$F_1(x, Q^2) = F_1(x) = \frac{1}{2x} F_2(x)$$

This approximation includes the assumption that interactions between partons in the proton occur over much longer timescales than the photon-proton hard scatter. Here, $f_i(x)$ are the parton distribution functions, PDFs, and may be interpreted as the probability of finding parton i with momentum fraction x inside the proton. The relationship between F_1 and F_2 is called the Callan-Gross approximation, and is valid for the case that the partons in the proton are only massless, charged, spin-1/2 particles. As a result of this relation, in the naïve QPM the longitudinal structure function F_L is equal to zero.

In this approximation, the structure functions depend only on x, not on Q^2. Consequently, the DIS $ep \to eX$ can be written as:

$$\frac{d^2\sigma^{ep}}{dxdQ^2} = \frac{4\pi\alpha^2}{xQ^4} \left[xy^2 F_1(x) + (1-y) F_2(x)\right]$$

2.6 QCD

Quantum ChromoDynamics, QCD, is the theory of the strong force, which mediates between hadronic particles. While it draws on its predecessor, the very successful Quantum ElectroDynamics, QED, some fundamental differences between electromagnetic interactions and strong interactions have resulted in QCD being a rather more complex theory. One of the most no-

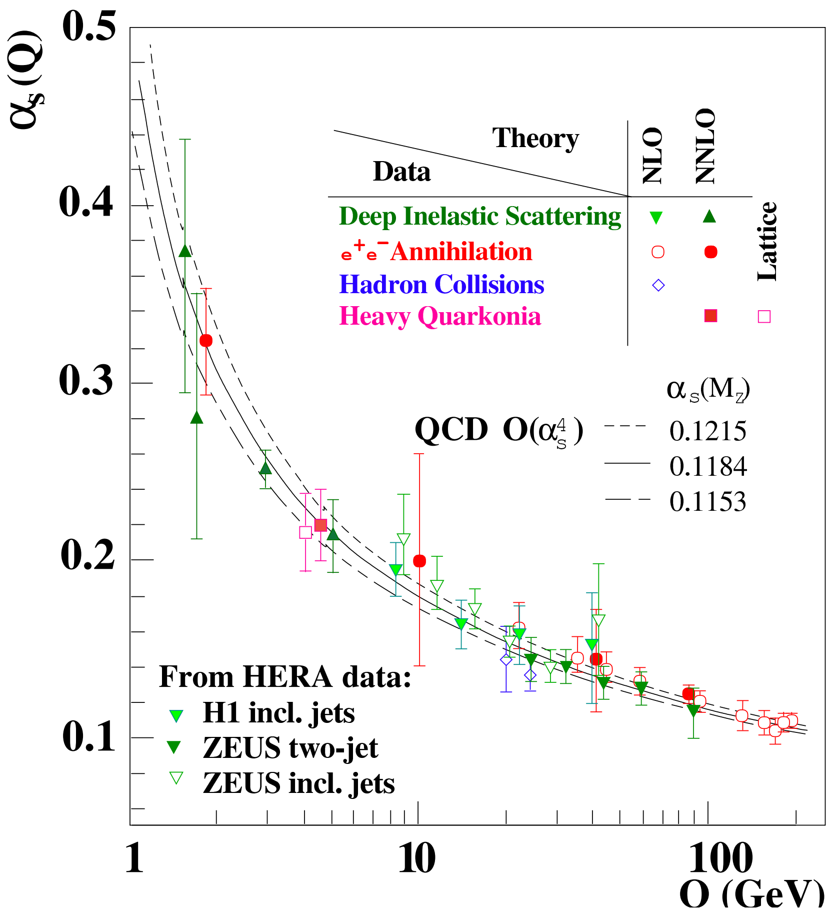

Figure 2.4: Experimental results displaying the running of α_S, the coupling of the strong force. The curves display the theory for different values of α_S. The data points display results from different experiments, including HERA. The results are consistent within errors.

table differences is that while the photons, which mediate electromagnetic interactions, have no charge, gluons, which mediate strong interactions, do possess colour. Two gluons may therefore interact with one another even in the absence of quarks.

QCD is an unbroken Yang-Mills field theory, that is, it is locally gauge invariant, and, because of gluon self-coupling, is described by a non-abelian gauge theory. In such a theory, the generators of the symmetry group are non-commutative. The gauge bosons of QCD are gluons, which are both massless and chargeless, although they are not colourless. As well as gluon self-coupling, a further difference between the two models can be found in the coupling strength. QED couples with the fine structure constant, α_e, while the coupling of the strong force, α_S, varies with energy. At leading order (LO) this coupling obeys the form

$$\frac{d\alpha_S(\mu^2)}{d\log(\mu^2)} = -b_0\alpha_S^2(\mu^2)$$

where μ^2 is an external energy scale, and the constant term b_0 is given by $b_0 = (33 - 2n_f)/12\pi$, with n_f being the number of quark flavours that are active at the scale μ^2. Experimental results displaying the running of α_S are displayed in figure 2.4.

QED is entirely renormalisable within perturbation theory, i.e. methods exist by which the infinite quantities associated with higher-order diagrams may be absorbed into the physical mass and charge. This is not true of QCD. The necessity for quarks to be confined in colour-neutral hadrons and the non-abelian nature of QCD prevent the use of perturbation theory for the full analysis of strong interactions [5]. However, at short range, the strong force displays the property of ‘asymptotic freedom’; that is, at very short distances the interaction between partons becomes weaker. We may therefore use perturbation theory safely for short distance interactions. Such processes, which include prompt photon production and the production of jets, may therefore be modelled using perturbation theory. That part of QCD which may be calculated perturbatively is known as perturbative QCD, or pQCD.

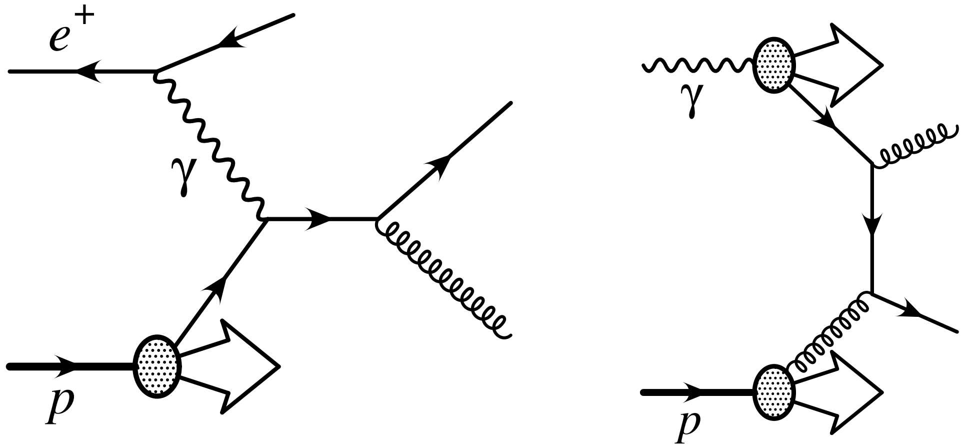

Figure 2.5: Examples of the lowest order photoproduction processes, showing the direct (left) and resolved processes.

2.7 Direct and resolved photoproduction processes

Similarly to the DIS case, the cross section in photoproduction may be written as

$$\frac{d^2\sigma^{ep}}{dydQ^2} = f_{\gamma/e}(y,Q^2)\sigma^{\gamma p}_{\mathrm{TOT}}(y,Q^2)$$

Here, $\sigma^{\gamma p}_{\mathrm{TOT}}$ is the total cross section of the process at a given centre of mass energy, and $f_{\gamma/e}$ is the photon flux, given by

$$f_{\gamma/e}(y,Q^2) = \frac{\alpha}{2\pi}\frac{1}{Q^2}[\frac{1+(1-y)^2}{y} - 2\frac{1-y}{y}\frac{Q^2_{\mathrm{min}}}{Q^2}]$$

and Q^2_{min} is the kinematic lower bound and is given by $Q^2_{\mathrm{min}} = m_e^2 y^2/(1-y)$.

Photoproduction events occur in neutral-current events which are mediated by a photon. The momentum transfer between the colliding particles is low, so that there is no contribution from Z^0 particles. Due to the nearly-real nature of the mediating photon, there are two types of process by which it may interact with the proton, known as 'direct' and 'resolved'. At lowest order in perturbation theory the diagrams for these processes form separate classes.

In direct processes, the entire photon interacts in a hard scatter with a charged component of the proton, giving a clean interaction with no photon remnant. Resolved subprocesses, on the other hand, occur when the photon briefly fluctuates into a quark-antiquark state. One of these intermediate particles can then interact with a parton from the proton. In this case, there will be a photon remnant seen in the detector; that is, particles which originate from the photon which are not directly involved in the collision. Direct and resolved processes are illustrated in figure 2.5.

We can define x_γ to be the fraction of the photon momentum which was involved in the interaction. So, for direct subprocesses x_γ is one, while for resolved processes it may take any value between zero and one at LO. Next to Leading Order, NLO, is more complex.

Photoproduction events dominate in HERA physics – the high momentum transfer seen in the DIS (Deeply Inelastic Scattering) regime is less common, as it is suppressed by a $1/Q^4$ relation, where $Q^2 = -q^2$ represents the photon virtuality, as before.

2.8 Prompt photon physics

A 'prompt' or direct photon is a useful tool to study QCD. A prompt photon process is one in which a high-p_T photon emerges directly from the QCD scattering. Here, p_T, or transverse momentum, is the component of a particle's momentum in the plane perpendicular to the beam direction, and therefore indicates the boost given to the particle by the exchanged particle. Since an outgoing photon, in contrast to quarks, is observed without any intermediate hadronisation,

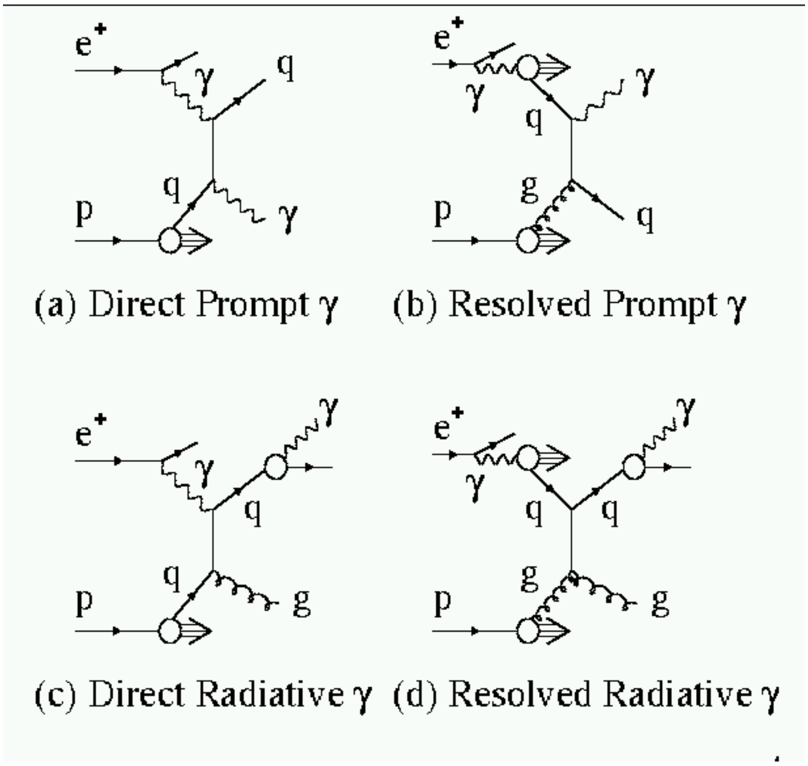

Figure 2.6: The lowest-order processes contributing to the prompt photon cross section, with direct and resolved on top and the radiative contributions arising from fragmentation shown underneath. In the direct process (a), the electron radiates a virtual photon which scatters from a quark in the proton, producing a high-p_T quark and a prompt photon. Process (b) is a resolved process in which a quark from the photon interacts with a gluon from the proton to produce a photon and a quark both at high-p_T. In the two radiative processes (c) and (d), the photon is not produced directly from the scatter, but rather radiated from a final state quark which may be produced from either a direct or resolved interaction.

it provides a particularly clean probe of the underlying QCD subprocess. The lowest-order diagrams contributing to the prompt photon process are shown in figure 2.6.

As described in section 2.7, photoproduction processes can occur via two principal mechanisms, the direct and resolved processes. Prompt photons may be produced by both processes, and examples of both are given in figure 2.6. The direct and resolved processes leading to radiative events at lowest order are also shown. These are described in more detail below.

The signal for a prompt photon event may be mimicked by jets. These may occur either through the decay of neutral mesons or through fragmentation of jets. Further, an irreducible part of the prompt photon cross section is made up of 'radiative' events. These background contributions to the prompt photon signal are described in more detail in the following paragraphs.

Neutral meson backgrounds

As well as from prompt photon events, the observed signal can also be given by neutral mesons, such as the π^0 and the η-meson. These decay to signals of multiple photons which are not prompt, since they do not carry immediate information about the QCD sub-process, except as part of the hadronisation process. Since neutral mesons are most often to be found in jets, they are to some extent suppressed by the isolation criterion. However, a residual contribution remains of approximately the same magnitude as the prompt photon signal. This must be dealt with to ensure an accurate measurement.

Fragmentation

Photons can further be produced as part of fragmentation within jets. These photons tend to be collinear with the jet, and therefore the isolation criterion also suppresses the contribution from these. Such photons are also likely to have nearby tracks due to charged particles in the jets. Ensuring that prompt photon candidates are well separated both from any tracks and from any large energy deposits means photons from this source can be discounted.

Radiative events

So-called 'radiative' events occur when an isolated high-p_T photon is produced from a final state quark. The detected photon does not originate from the QCD subprocess, but may be indistinguishable from a true prompt photon event at the detector level. The radiative component is therefore an irreducible background to the prompt photon cross section. Examples of the lowest-order radiative events are shown in figure 2.6.

Radiative events are calculable within pQCD. However, they do not carry the same information about the QCD subprocess as the 'prompt' events and are therefore secondary to the physics aim of the analysis. Modelling of these events indicates that they are of the same order as prompt photon events.

2.9 Recent prompt photon research

2.9.1 Prompt photons at DESY

Previous prompt photon results have been published by the ZEUS collaboration [6] and by the H1 collaboration [7].

In the photoproduction regime, cross sections for the inclusive process $e \pm p \to \gamma + X$ have been published and compared to PYTHIA and HERWIG Monte Carlo simulations by the ZEUS collaboration. Good agreement was discovered between both Monte Carlo models and the NLO calculations for the E_T^γ distribution. However, in the rear region of η^γ, an excess is observed

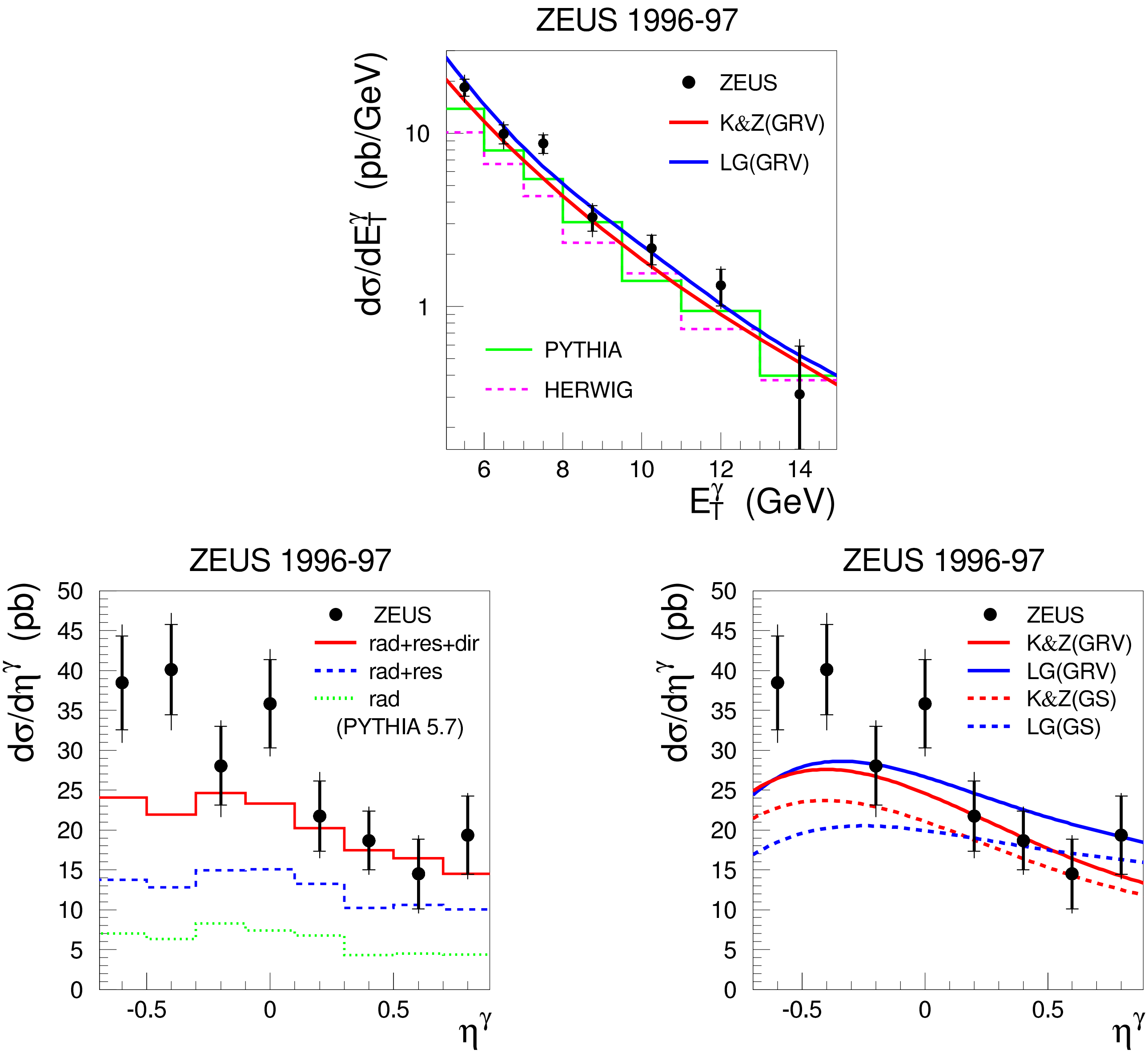

Figure 2.7: Cross sections are displayed with respect to E_T^γ and η^γ, compared to NLO calculations and PYTHIA and HERWIG Monte Carlo models. Good agreement is observed in E_T^γ, however an excess is observed in the rear region (that is, negative photon pseudorapidity, η^γ). Neither the NLO nor the Monte Carlo simulations model this excess.

in the η^γ distribution, which is not modelled by the Monte Carlo or by the NLO calculations. The results are shown in figure 2.7.

An in-depth study of the intrinsic K_T of partons in the photon was also published using photoproduction results for the $\gamma+$ jet process [8]. Since the proton and other hadronic particles are composite particles, each parton which makes up the proton will have a non-zero value of momentum, K, which is a fraction of that of the proton. Further, the partons may also possess momentum perpendicular to the momentum of the proton K_T, and a study of K_T provides significant information about the behaviour of the partons within the proton. The results of the analysis for direct photoproduction events were compared to PYTHIA Monte Carlo, which was generated with varying values of the intrinsic K_T parameter k_0. Figure 2.8 shows the result of the measurement compared to values from other experiments.

Measurements have also been made at ZEUS of prompt photons in the DIS regime [9]. The processes involved are different from those which contribute to the cross sections in photoproduction. In the DIS regime, the lowest-order prompt photon processes are first order in QED but zeroth order in QCD, that is, they are purely electromagnetic in nature. Therefore in this case it is the next-to-leading order, NLO, processes which contribute to our understanding of QCD.

In the inclusive process in DIS, it was found that the Monte Carlo models PYTHIA and HERWIG did not describe the data well. Both simulations lie significantly below the data. Scaling the Monte Carlo by a factor allows for a shape comparison, in which HERWIG achieves a better comparison than PYTHIA, although HERWIG requires a larger scaling. However, HERWIG does not well describe the Q^2 distribution of the data, which casts doubt on its modelling of the dynamics.

Comparisons to NLO calculations are only available for the photon plus jet process in

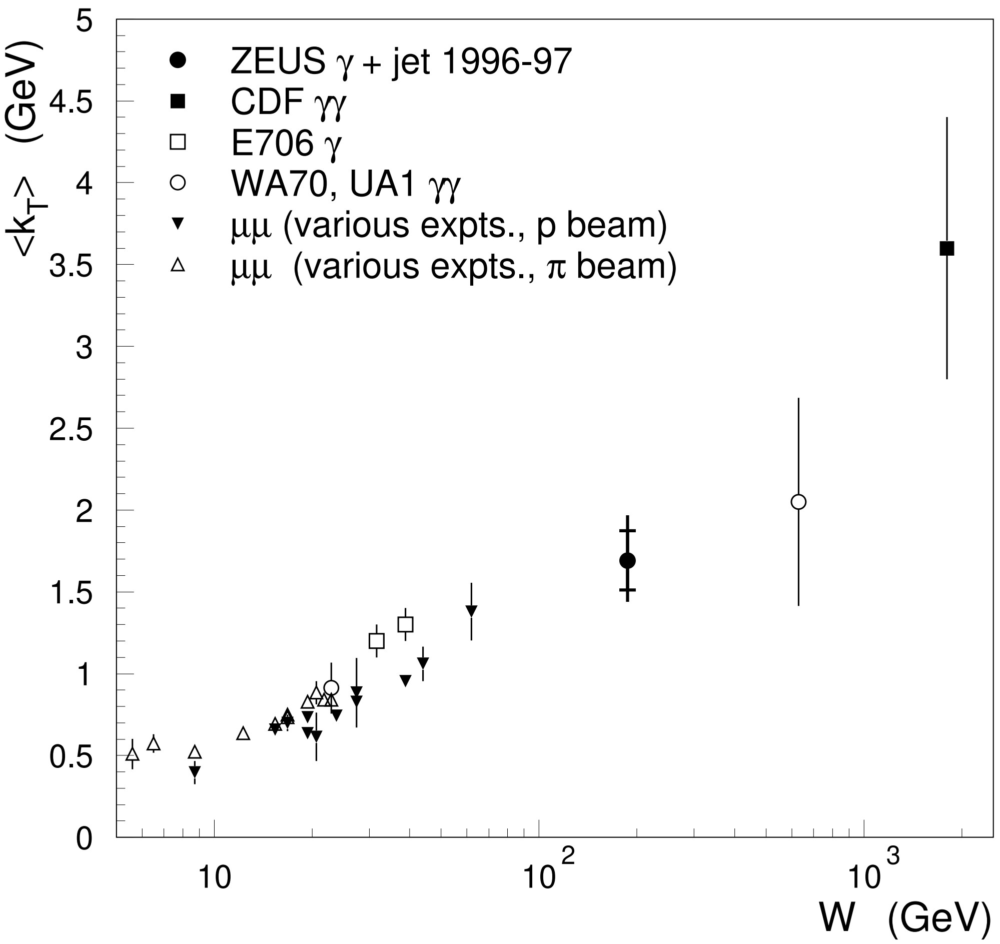

Figure 2.8: The prompt photon results for the photon plus jet process are used to extract a value for the intrinsic K_T of partons in the photon. The ZEUS result (filled circle) compares favourably with values obtained by other experiments.

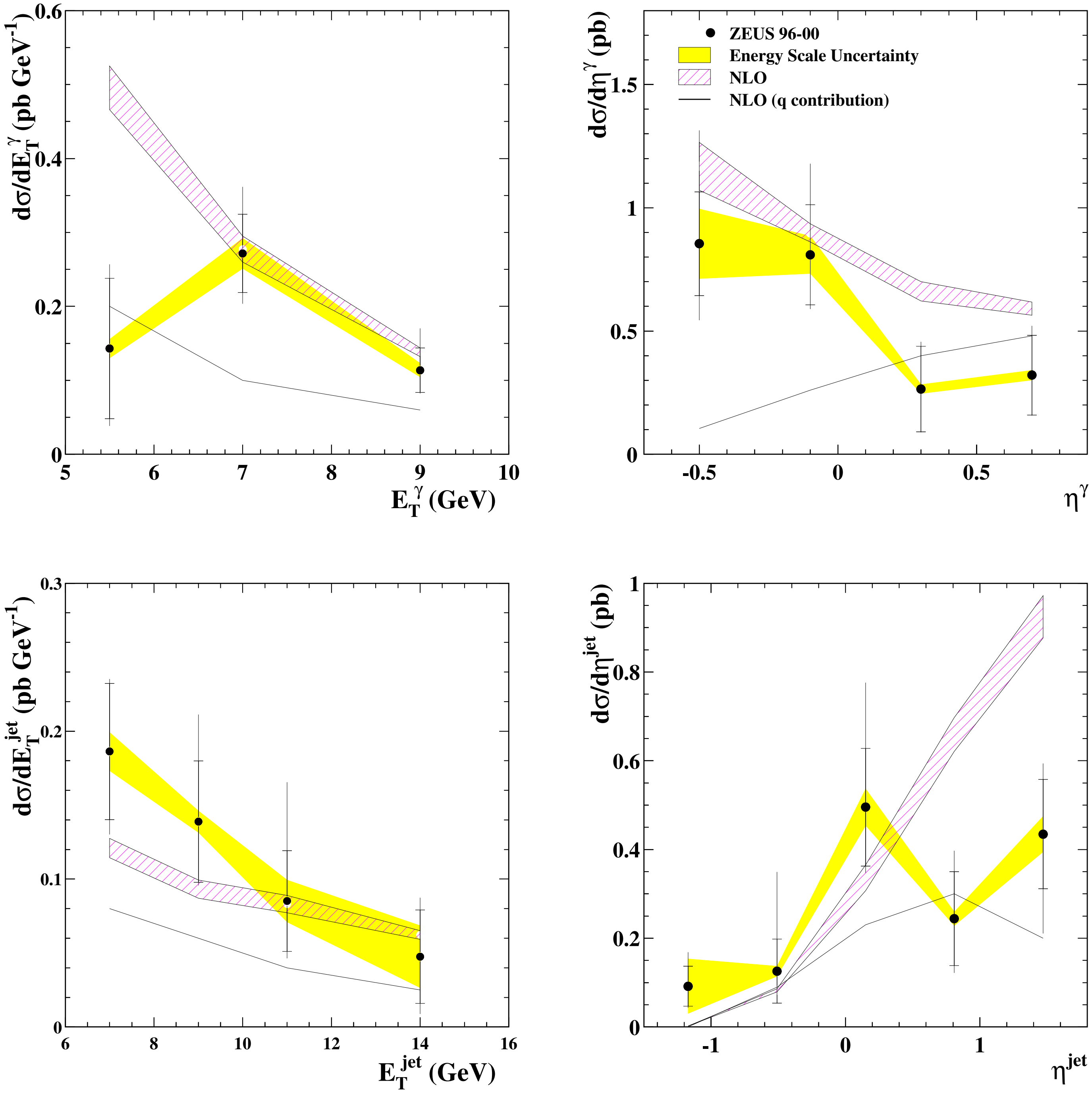

Figure 2.9: The cross sections for the prompt photon plus jet process in the DIS regime, compared to NLO calculations. The single black line displays the calculated contribution from quark-line radiation. Quantitatively, the agreement between data and calculation is good, however there are some discrepancies in shape.

DIS. Quantitatively, the NLO calculations model the data rather better than the Monte Carlo simulations. There are still some discrepancies in the shape of the distributions, however. The comparisons to NLO calculations are shown in figure 2.9.

Prompt photons in photoproduction have also been observed at H1. The method is not identical to the ZEUS method, with differences arising mainly from the differences in the detector set-up. While the methods used to subtract the neutral meson background in both experiments are similar, the H1 method uses a discriminator function, which depends on three aspects of the photon shower in the calorimeter: the depth the photon penetrates, the fraction in the highest energy cell, and the shower radius. This allows for background subtraction on an event-by-event basis rather than a statistical one.

The H1 measurement, as seen in figure 2.10, shows reasonable agreement between the data and NLO calculations. Further, the large excess observed in the distribution in the rear pseudorapidity range in the ZEUS measurement is modelled more accurately for the H1 measurement. However, a comparison between the ZEUS and H1 results, figure 2.11, shows that the measured data are in good agreement overall. When compared to Monte Carlo simulations, the excess is observed in H1 data as well as ZEUS.

2.9.2 Prompt photons at the Tevatron

The Tevatron accelerator at Fermilab in Chicago collides protons and anti-protons. This provides a much higher centre of mass and opens up the possibility for physics that could not be

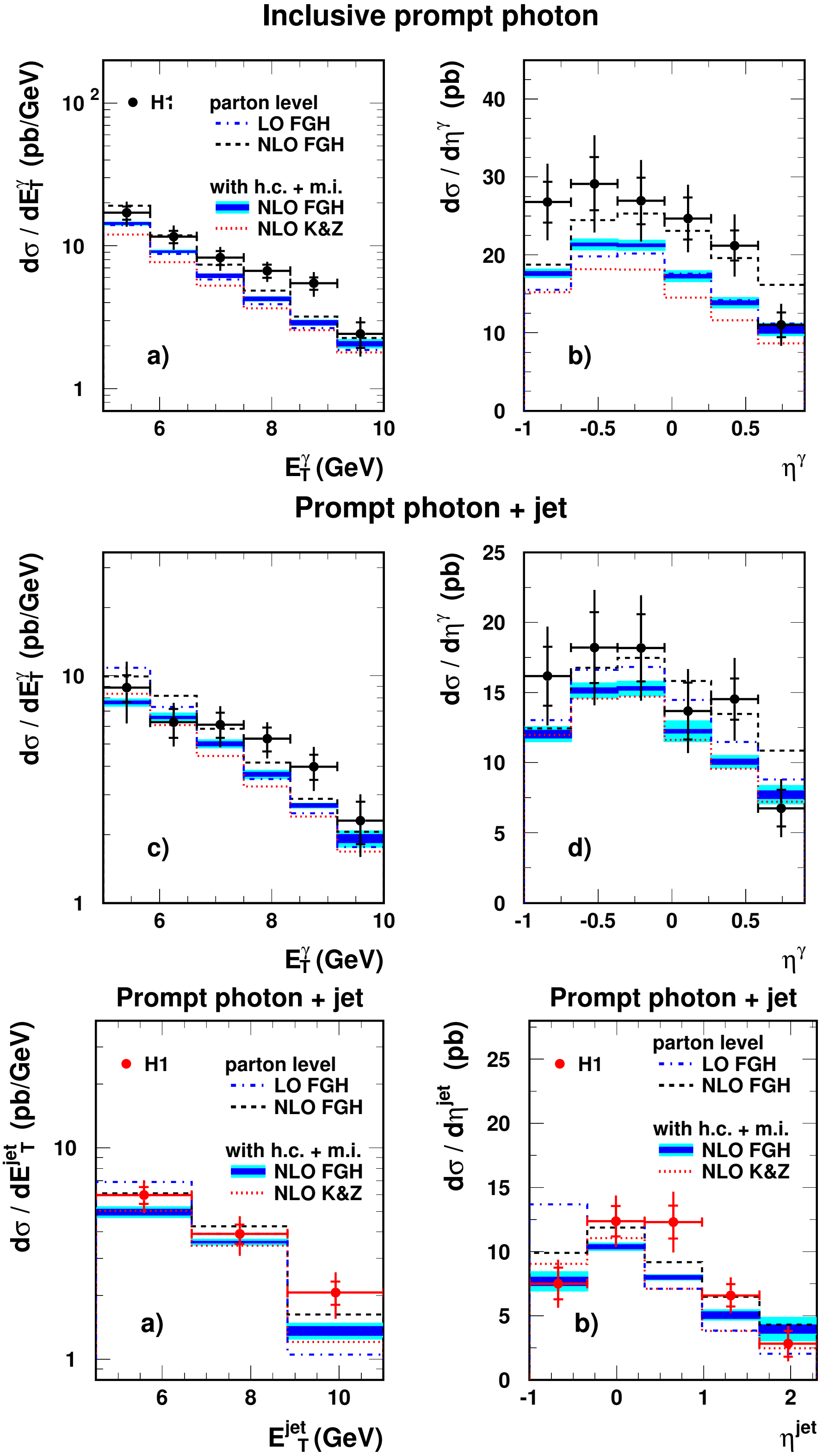

Figure 2.10: H1 cross sections compared to NLO calculations for the inclusive and the photon plus jet processes.

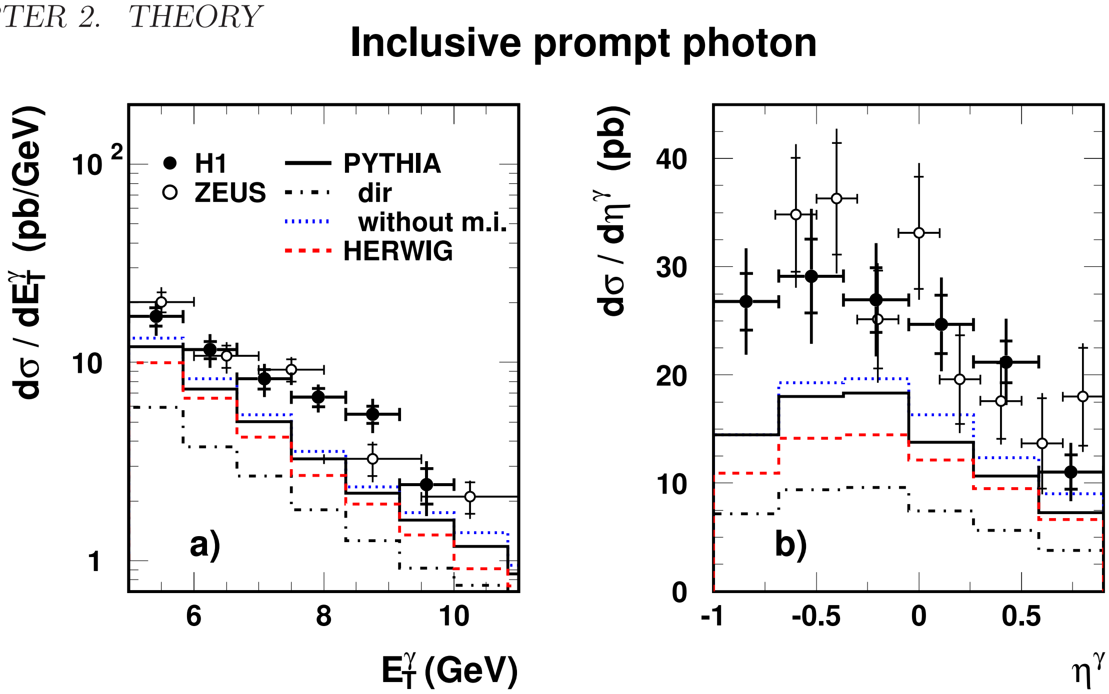

Figure 2.11: Measurements from ZEUS (open circles) and H1 (filled circles) show good agreement. The excess in data compared to the Monte Carlo simulations, PYTHIA and HERWIG, is observed in both data sets, although the ZEUS excess is perhaps slightly more pronounced.

seen at HERA. Measurements of prompt photon cross sections have been made at the Tevatron[1] by both the CDF and D0 collaborations.

Results from the D0 collaboration have been published [10] displaying the cross section for the prompt photon processes and also the ratio between the measured cross section at centre of mass energies of 630 GeV and 1800 GeV. The D0 detector allows prompt photons to be studied in the forward η region, $1.6 < |\eta^\gamma| < 2.5$ as well as the central region, $\eta^\gamma < 0.9$. The method used is similar to that used by ZEUS taking into account differences in detector set-up, however, the higher centre-of-mass energies available to the Tevatron experiments allow measurements

[1]Experiments at the Tevatron generally refer to prompt photon events as 'direct' photon events, referring to the fact that the photon comes directly from the QCD subprocess. However, since there is a type of photoproduction process which is also known as 'direct', the term 'prompt' will be used for the purpose of clarity throughout this thesis.

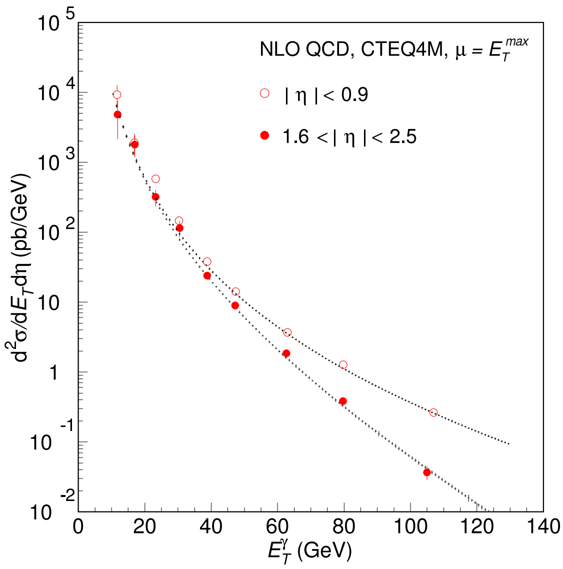

Figure 2.12: Results from the D0 collaboration for the prompt photon cross section with respect to E_T^γ, published in 1999. The open circles represent the central pseudorapidity region, while the filled circles are measurements from the forward region. The high centre-of-mass energy of the Tevatron allows the measurement to be taken at much higher values of E_T^γ than is available at HERA. Results agree in both pseudorapidity regions for low E_T^γ, however at high E_T^γ a discrepancy develops between the two regions. The curves are the calculated NLO cross sections, from a calculation by Baer, Ohnemus and Owens.

of photon E_T to over 100 GeV. The results are displayed in figure 2.12.

Comparisons between the measurements taken at the forward and central pseudorapidity regions begin to diverge at high values of E_T^γ, which is well-modelled by the NLO calculations. This is seen at energy values which are not reachable by the current analysis in HERA, although it may be possible to study higher-E_T photons with the suggested dijet method. However, the configuration of the ZEUS detector makes studying the forward region difficult, as the neutral

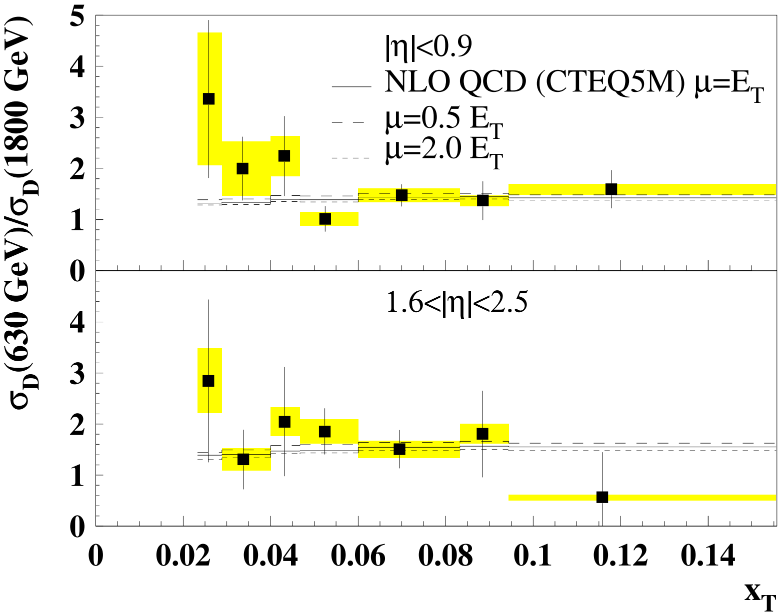

Figure 2.13: Results from the D0 collaboration displaying the ratio of prompt photon cross sections at centre-of-mass energies of 630 and 1800 GeV. The top plot refers to the central region in pseudorapidity, while the lower plot covers the forward region of $1.6 < \eta^{\gamma} < 2.5$. In both plots, the line shows NLO calculations. The effect of varying the scale factor, μ, is also shown.

meson subtraction process (described in detail in chapter 6) relies upon the projective geometry found only in the Barrel section of the ZEUS calorimeter.

More recently, D0 has published results showing the ratio between prompt photon cross sections at centre-of-mass energies of 630 GeV and 1800 GeV.

The resultant ratio is displayed in figure 2.13. Although there appears to be a systematic excess in the data as compared to the theory for low values of $x_T = \frac{2E_T}{\sqrt{s}}$, the systematic and statistical errors are of sufficient magnitude that it is impossible to conclude there is any real disagreement between the data and the theory.

The study of prompt photon processes at CDF has also been active in recent years. Vari-

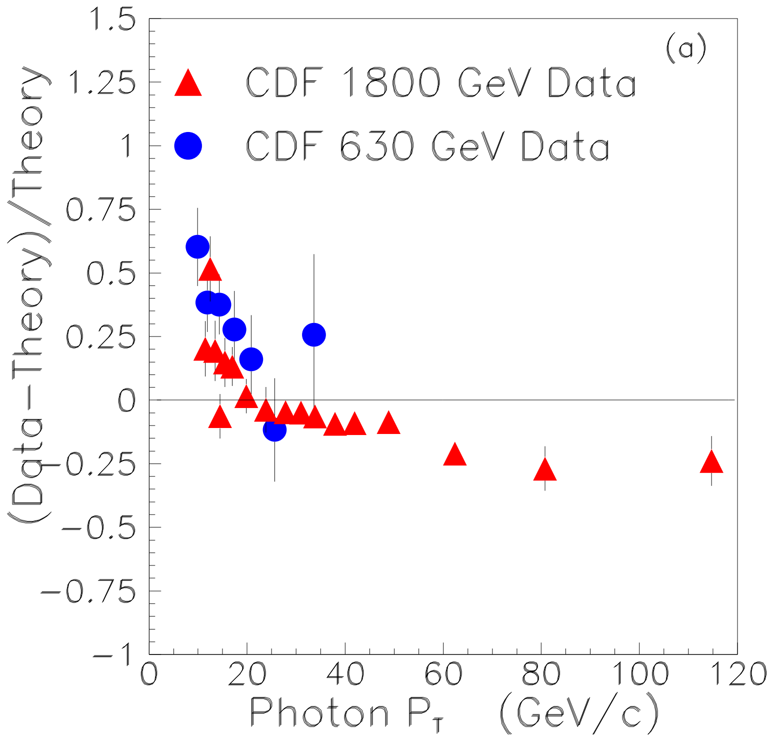

Figure 2.14: The CDF collaboration has measured the inclusive prompt photon cross section with respect to the p_T of the photon. Discrepancies between data and theory were discovered, which were particularly noticeable at low-p_T. These existed in the measurements at both $\sqrt{s} = 630\,\mathrm{GeV}$ and $1800\,\mathrm{GeV}$. The CDF measurement, unlike the similar one at D0, did not appear to lie within the experimental errors.

ous processes have been studied, including the inclusive prompt photon cross section, prompt photons with two jets or with heavy flavours (that is, jets from c- or b-quarks), and di-prompt photon events [11]. These processes are not available at HERA owing to the lower centre-of-mass energies, which restrict statistics for study of these more exotic processes.

Prompt photon cross sections at CDF were measured in 2002 [12] using the higher centre-of-mass energy available later at the Tevatron. Comparisons were made between the results at the two centre-of-mass energies, similar to those made at D0 (figure 2.13). As seen in figure 2.14, a discrepancy was observed between the theory and the data, which was particularly severe at

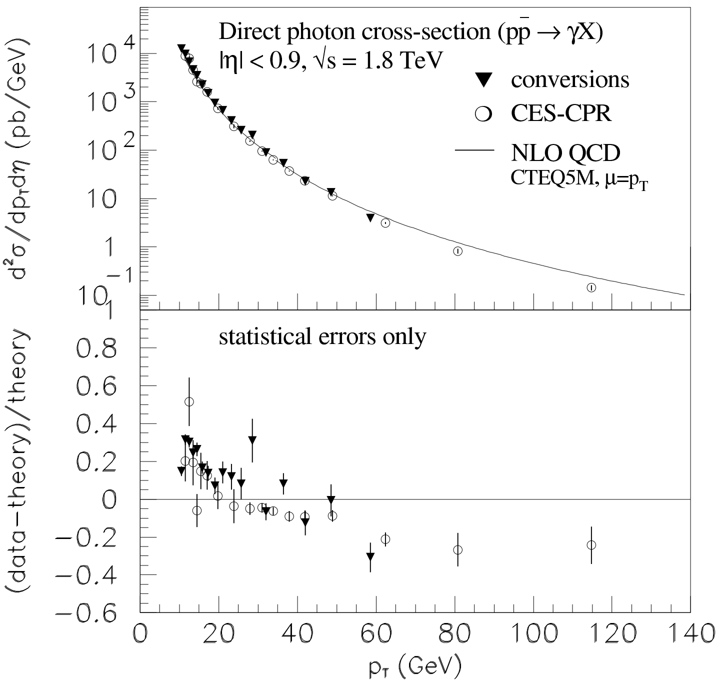

Figure 2.15: The CDF collaboration re-measures the prompt photon cross section with respect to p_T^γ. Contrary to earlier methods at CDF, this measurement uses a 'conversion probability' to discriminate between signal and background, similar to that proposed by my ZEUS colleagues (see section 1.4). Here, the cross section is compared to theoretical predictions, and the differences between data and theory can be more clearly seen from the lower plot.

low values of p_T.

Cross sections for prompt photon events were therefore re-evaluated more recently [13] at CDF using a 'conversion probability'-based method for background discrimination. The measured p_T cross section is shown in figure 2.15. This method measures only those photons which convert to an e^+e^- pair in the detector. There will therefore be tracks associated with the photon signal, which eliminates any contribution from neutral mesons, providing an independent analysis method.

The discrepancies between theory and data were much reduced in magnitude in the conversion probability measurement. However, the discrepancy at low-p_T remains, and both analyses display the same shape in p_T, despite the large differences between the two methods. This would appear to indicate the need for refinement of the theoretical calculation.

Chapter 3

The ZEUS Detector

The DESY laboratory in Hamburg is home to the HERA ring, the world's only hadron-electron colliding beam facility.

3.1 The HERA accelerator

Figure 3.1 shows the layout of the HERA accelerator and its experiments. H1 and ZEUS are situated in the north and south halls of HERA respectively, and both are colliding beam experiments. HERMES and HERA-B in the east and west halls are fixed-target experiments. HERMES studies the spin structure of the nucleon using the electron beam on a nuclear target. HERA-B, on the other hand, uses the proton beam to study CP-violation from the B-meson decay channel $B \to J/\Psi K^0$.

HERA, the Hadron-Elektron Ring Anlage, is a 6.3km circumference synchrotron accelerator. It is the world's first and only collider to provide collisions between hadrons and electrons[1]. The original design of the accelerator was to provide a lepton beam at 27.5 GeV and the proton beam

[1]The word *electrons* is here used interchangeably with positrons, unless otherwise specified.

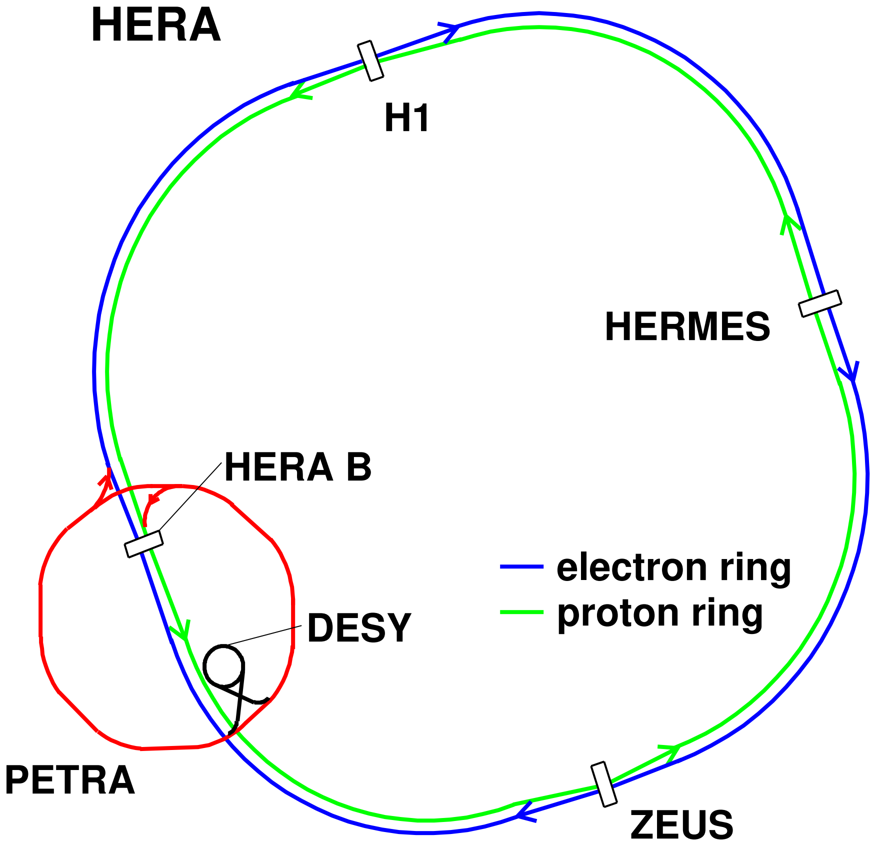

Figure 3.1: The HERA ring, displaying the four experiments and the electron and proton rings. Also shown are the DESY and PETRA pre-accelerators.

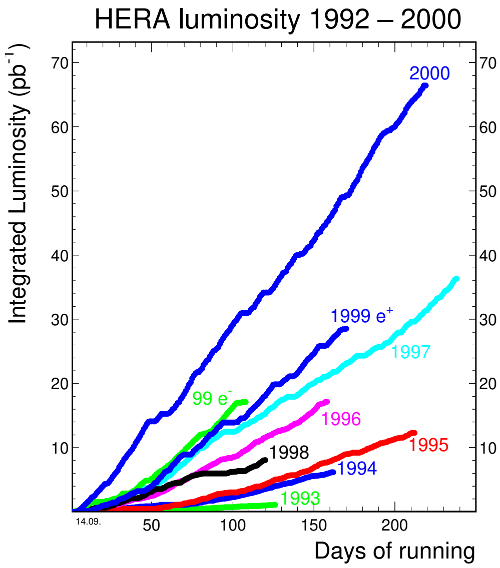

Figure 3.2: HERA luminosity for the years 1992-2000

at 820 GeV. During the upgrade in 1998 the proton beam energy was increased to 920 GeV. This provides a centre-of-mass energy $\sqrt{S}$ of 300 GeV from 1992-1997 and of 318 GeV for 1998-2000. In 2000, a long-term shutdown was begun in order to provide a luminosity upgrade.

Since its commissioning in 1992, the HERA accelerator has provided luminosity with both electrons and positrons, although the majority of HERA data has used positrons. Positron beams have a longer lifetime than electrons, since, being of positive charge, they repel any positive ions left in the beampipe, reducing the number of interactions with the beam-gas. Negatively-charged electron beams, on the other hand, will attract these ions.

In the years 1992-2000, HERA provided luminosity with both electrons and positrons. From 1992 - 1997, HERA provided collisions between protons at 820 GeV and positrons at 27.5 GeV. In 1998, the proton beam energy was increased to 920 GeV. Two years of luminosity with an electron beam was provided in 1998-99, before returning to positron running in 1999. The total integrated luminosity provided for e^+p (e^-p) collisions until 2000 was 96 pb^{-1} (17 pb^{-1}), as

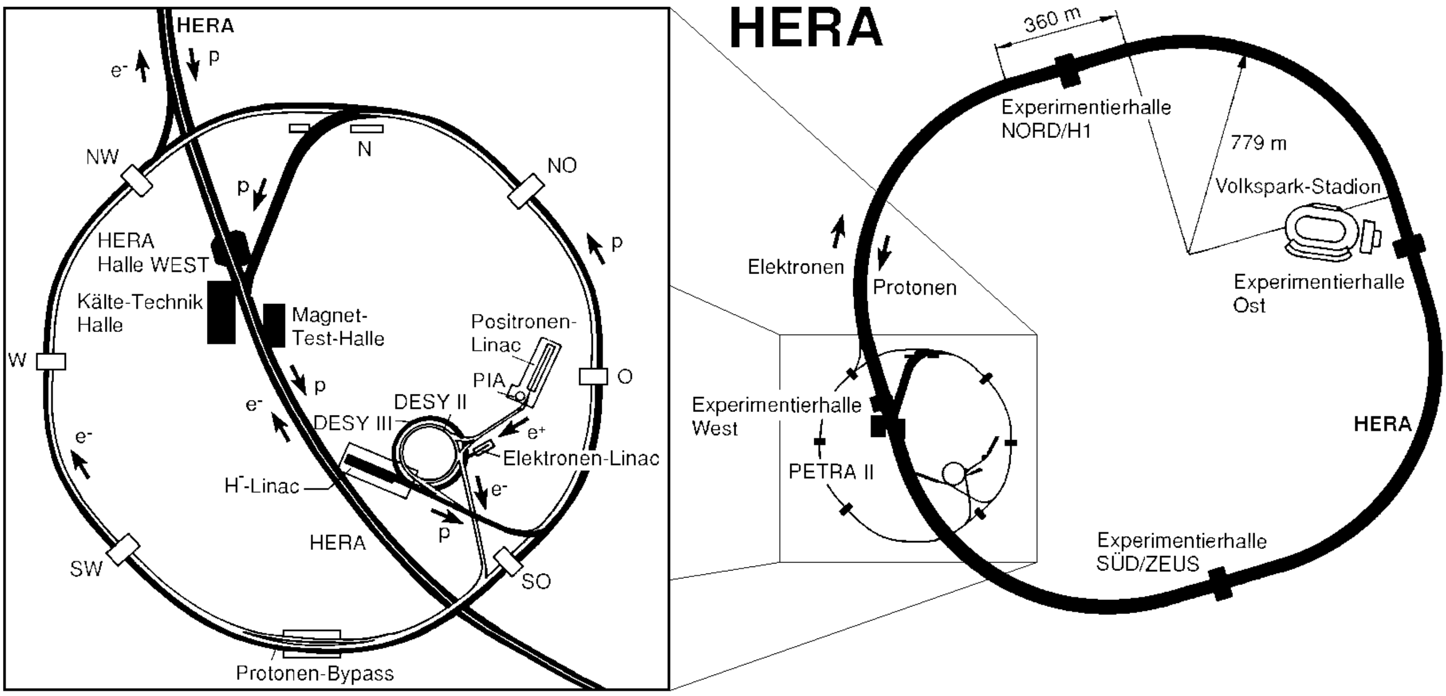

Figure 3.3: The HERA injection system, showing the LINAC systems, the DESY II and III accelerators and the PETRA accelerator.

indicated in figure 3.2.

3.2 The HERA injection system

HERA uses a two-ring storage system where leptons and protons are kept separate and are accelerated using superconducting and conventional magnets respectively. The acceleration of these particles is a multiple stage process, and leptons and hadrons are kept separate throughout. The system is shown in figure 3.3. For proton acceleration:

- H^- ions are accelerated to 50MeV using a linear accelerator (linac). They are then stored in the Positron Intensity Accumulator until a current of 60mA is accumulated.

- These are passed to the DESY III proton synchrotron, where they are stripped of their electrons by passing them through a thin foil. They are then accelerated to 7.5 GeV. At this stage they are held in 11 bunches with the same 96ns bunch spacing as the HERA ring uses.

- The protons are passed to the PETRA storage ring, which accelerates them to 40 GeV, where a maximum of 70 bunches can be stored.

- They are then injected into HERA and the process is repeated until the required number of bunches (maximum 210) are stored in HERA. Radio frequency cavities and superconducting magnets are used to accelerate the protons to their operation energy.

The lepton beam undergoes a separate but similar process. Electrons, if required, are produced directly from an electron gun, while positrons are provided using e^+e^- pair production from electron *bremsstrahlung* photons interacting on a tungsten target. These are then accelerated using LINACs I and II to 220 and 450MeV respectively, before being injected into DESY II and accelerated to 7.5 GeV. They can then be injected in 70 bunches with 96 ns spacing into PETRA's lepton-ring, where they are accelerated to 14 GeV. Finally, they are injected into the HERA ring and accelerated to their operating energy of 27.5 GeV.

HERA has a maximum storage capacity of 210 bunches. Usually, a fill will use an average of 174 paired bunches for colliding, 15 unpaired lepton and 6 unpaired proton bunches for background calibration, and 15 empty bunches, which, as well as aiding in background calibrations, also provide a safety precaution in the event of an emergency beam dump. The bunch structure is illustrated in figure 3.4.

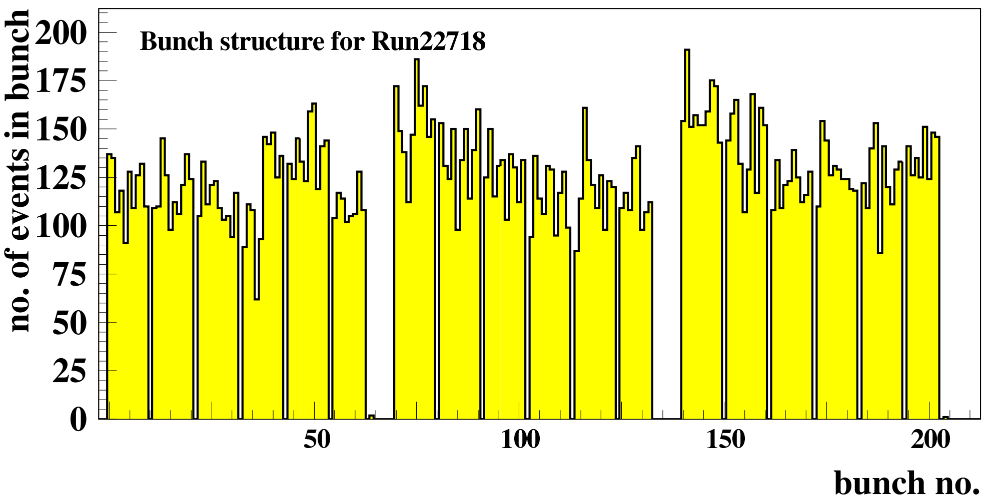

Figure 3.4: An example of the bunch structure in HERA.

3.3 The ZEUS detector

The ZEUS detector [14] measures 12 x 10 x 19 m in dimension. The asymmetric nature of *ep* collisions means that most of the detector material has to be concentrated in the proton-beam direction. Figure 3.5 is a diagram of the ZEUS detector.

The key components of the detector are as follows.

3.4 Overview of the detector

3.4.1 The ZEUS coordinate system

The coordinate system used for the ZEUS detector is right-handed. The $+z$ direction is defined by the proton beam, the $+y$ direction is upwards and the $+x$ direction is towards the centre of

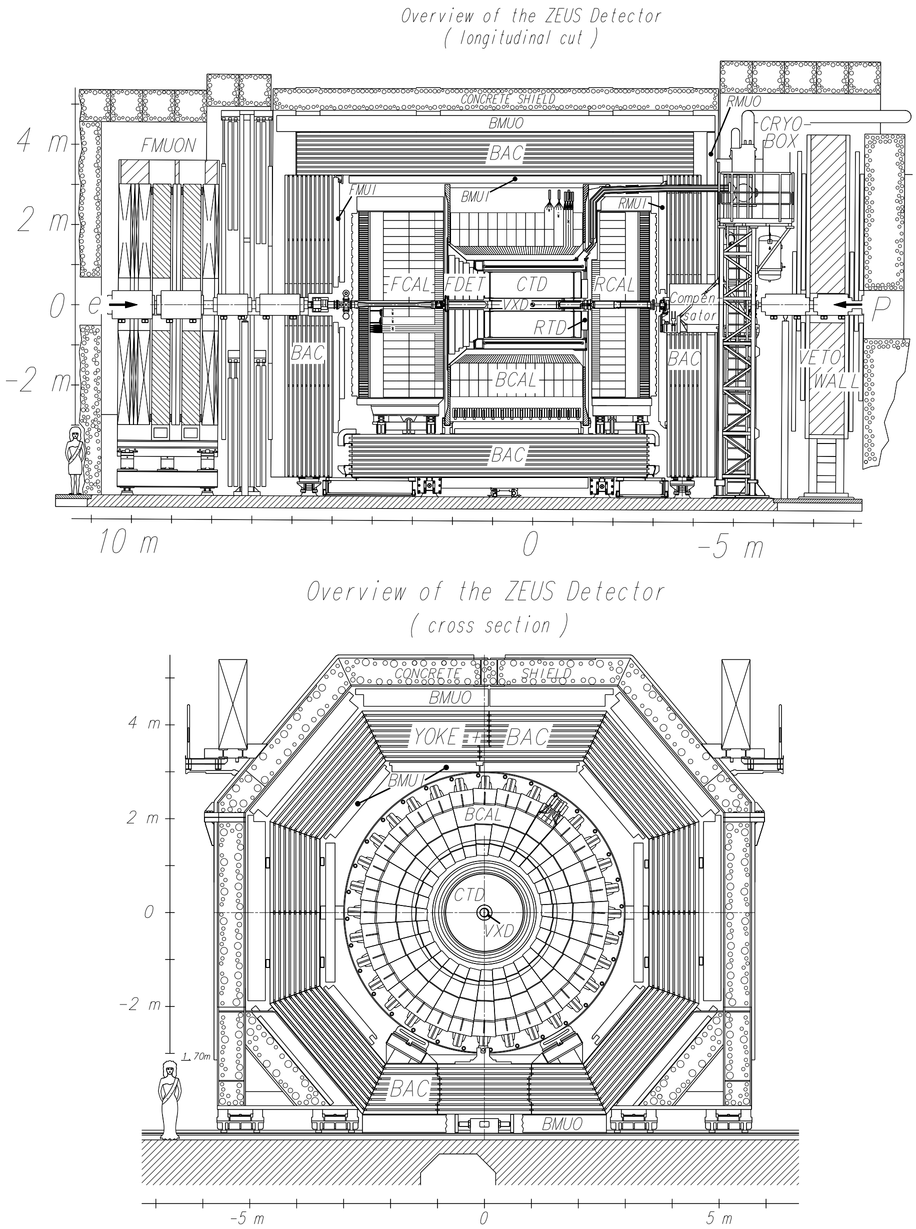

Figure 3.5: A diagram of the ZEUS detector in the $x-z$ and $x-y$ planes.

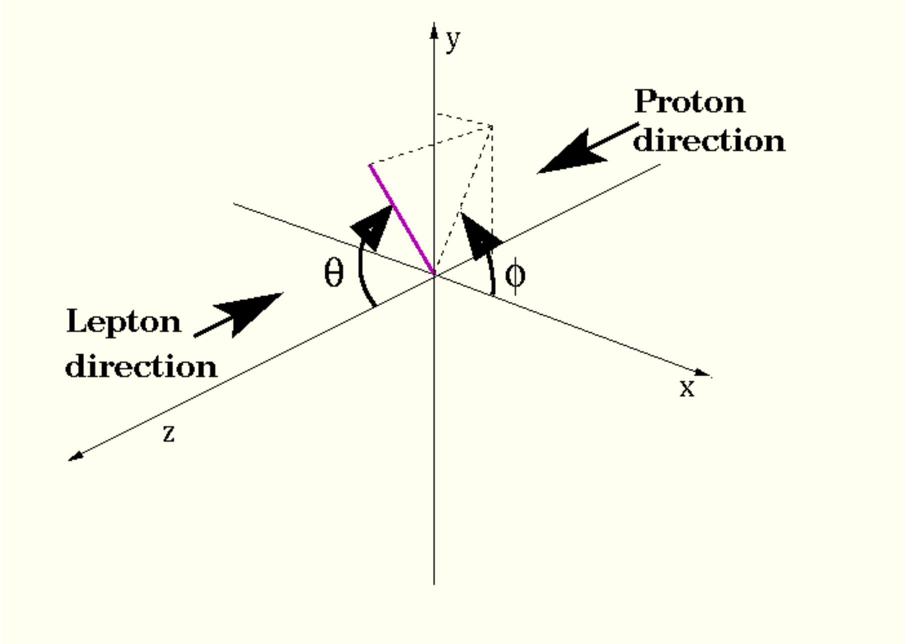

Figure 3.6: A schematic representation of the ZEUS coordinate system.

HERA. The polar angle, θ, runs from $0°$ to $180°$ forward to rear in z. The azimuthal angle, ϕ, takes 0 to lie on the x axis, and runs in the $x-y$ plane, centred on the z axis, where $0° < \phi < 360°$. This is illustrated in figure 3.6.

The nominal interaction point is $x = y = z = 0$.

3.4.2 The components

At the centre of the ZEUS detector, the tracking detectors provide detailed information about the position and momentum of charged particles. They also provide basic vertex information for an event. During the shut-down in 2000, a new MicroVertex Detector, MVD, was installed to provide more detailed primary and secondary vertex information. This was not present during the run periods included in this analysis, and thus is not described further. More information on the tracking detectors is given in section 3.5.

Beyond the tracking detectors is the Solenoid. This is a thin superconducting magnet which lies between the CTD and the Barrel Calorimeter. The solenoid provides an axial magnetic field of 1.43T, which allows momentum measurement of charged particles. The effect of this magnet on the HERA beams is reduced by the use of a powerful superconducting compensating solenoid located in the rear endcap of the iron yoke.

The Uranium CALorimeter, UCAL, lies beyond the solenoid. This is described in more detail in section 3.6. There is also the Presampler [15], which is situated between the solenoid and the UCAL. This thesis will concern itself with the Barrel Presampler, BPRE, which is therefore described in more detail in subsection 3.6.2. Beyond the UCAL is the BAcking Calorimeter, BAC. This is outwith the iron yoke. Although the majority of jet energy is contained within the UCAL, there is a certain amount of leakage which becomes significant when large jet energies are considered, in which case the BAC becomes indispensable.

Outwith the BAC are the muon detectors. These surround the detectors and provide trajectory information for high-energy muons which pass through the calorimeter.

The following sections provide details about components which play small but essential parts in this and other analyses.

3.4.3 The luminosity monitor

The luminosity measured at ZEUS is estimated using the rate of the bremsstrahlung process $ep \rightarrow ep\gamma$. The final state electron and photon are detected in coincidence at small angles from the beampipe. The luminosity monitor [16], LUMI, consists of two detectors, one to measure the electron and the other to measure the photon.

The electron detector is situated 34m from the interaction point in the $-z$ direction, while the photon detector is at -104m. Both are lead-scintillator sampling calorimeters. The HERA magnetic field deflects electrons with scattering angles < 6 mrad and energies such that $0.2E_e <$

$E'_e < 0.8E_e$ in such a way that they can leave the beampipe via a window at $z = -27$m, and are then detected by the electron calorimeter. Photons which are radiated within a cone of 0.5 mrad from the beam axis can leave the beampipe via a window at $z = -92$m and are then detected by the photon calorimeter.

Both calorimeters have an energy resolution given by

$$\frac{\sigma(E)}{E} = \frac{18\%}{\sqrt{E}}$$

where E is in GeV. However, in order to protect the photon calorimeter from damage due to synchrotron radiation, the photon calorimeter is shielded by a 1-radiation-length carbon filter. This reduces the resolution of this detector to

$$\frac{\sigma(E)}{E} = \frac{25\%}{\sqrt{E}}$$

3.5 Tracking

Tracking at ZEUS is provided by the three tracking detectors, the Central Tracking Detector, CTD, the Forward Tracking Detector, FTD, and the Rear Tracking Detector, RTD. There is also the SRTD - Small-angle Rear Tracking Detector, which records tracks close to the beampipe.

The FTD covers the angular range $7.5° < \theta < 28°$. It consists of three planar drift chambers, FTD1, FTD2, and FTD3, each of which consists of three planes of wires arranged into cells. These planes are rotated by 120° with respect to each other to allow for more accurate resolution of multiple tracks. For the period 1996-97, the TRD, Transition Radiation Detector, was interspersed between the three chambers of the FTD. This consisted of four modules located between FTD1 and FTD2 and between FTD2 and FTD3. The TRD allowed for lepton-hadron separation for particles of less than 30 GeV by detecting the transition radiation emitted when the particle passes between two media. During the luminosity upgrade which began in 2000, the TRD was replaced by the Straw Tube Tracker, STT, which should improve track resolution in this region.

The RTD covers the angular region $160° < \theta < 170°$. It is analogous to the FTD in that it is also a 3-planar drift chamber. The SRTD, Small-angle Rear Tracking Detector, provides tracking information on the scattered positron.

The combined angular acceptance of the ZEUS tracking detectors is $7.5° < \theta < 170°$.

3.5.1 The CTD

The ZEUS Central Tracking Detector, CTD [17], is a cylindrical drift chamber. It uses a combination of field and sense wires arranged in layers to provide information about the charge, momentum, and direction of a charged particle in its sensitive volume. The passage of a charged particle causes ionisation in the gas mixture. The E and B fields within the CTD, generated by an applied voltage, then cause the electrons to drift towards the sense wires, which record them as a current pulse. The location and timing of each pulse can provide information about the original particle.

The ZEUS CTD has an outer radius of 82.4 cm and an outer length of 241.0 cm, and the sensitive volume has a length of 203.0 cm, an inner radius of 19.0cm and an outer radius of 78.5 cm. It contains a gas mixture of argon, ethane, carbon dioxide and ethanol. The chamber comprises 9 'super'layers of drift cells, each cell containing 42 wires, 8 of which are sense wires while the remainder provide the required field. There are 4,608 sense wires in the CTD. The layout of these cells within the superlayers can be seen in figure 3.7.

There is a drift time associated with the reception of the signals, which is the time taken for the ionised electrons to reach the sense wire. The maximum drift time is proportional to

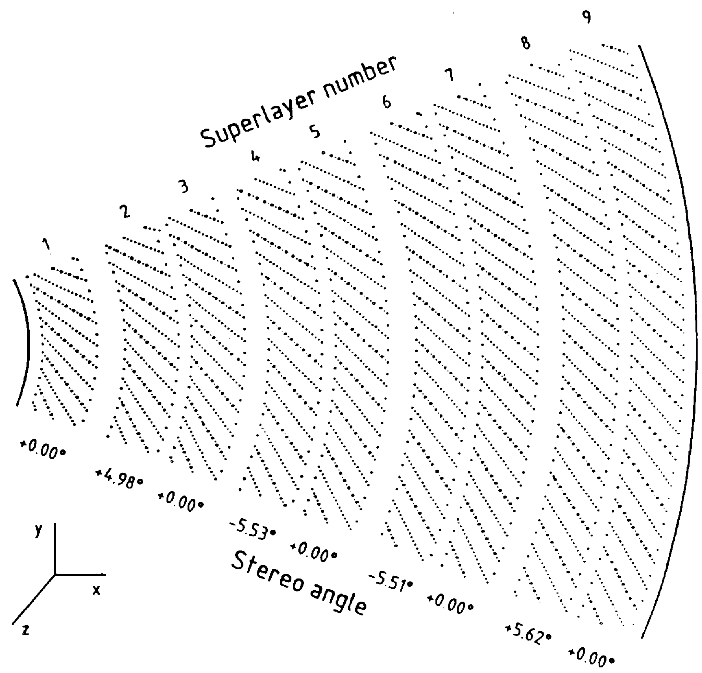

Figure 3.7: A schematic diagram showing one octant of the CTD

the maximum drift distance, and for the ZEUS CTD is about 700 ns or 7 bunch crossings.

Signals from the sense wires are gathered simultaneously by two electronic systems, the Flash Analogue to Digital Converter, fadc, system and the z-by-timing system. The z-by-timing system allows for coarse time measurements with a digitisation time of 48 ns, and provides information in z. The fadc system has a much finer digitisation of 9.6 ns, giving more detailed information. There is no z information immediately available with the fadc system. The z-by-timing system is used extensively by the ZEUS tracking triggers.

The CTD provides a high resolution of charged particles. Charged final-state hadrons and leptons are reconstructed with a spatial resolution of 190μm. The momentum resolution of the CTD is given by:

$$\frac{\sigma(p_t)}{p_t} = 0.0058p_t \oplus 0.0065 \oplus \frac{0.0014}{p_t}$$

3.6 The calorimeter and the BAC

The ZEUS Uranium CALorimeter, UCAL [18], provides measurements of energy deposited by particles. The overall structure of the UCAL is displayed in figure 3.8. This structure allows for measurements of energy, position and momentum of particles or jets, and further allows electromagnetic and hadronic particles to be distinguished.

The UCAL consists of alternating layers of 3.3mm depleted Uranium and 2.6mm plastic scintillator material. The thicknesses were chosen so that the UCAL is compensating; that is, the response to hadrons and electromagnetic particles is equal for particles of the same energy. This is particularly useful for the study of Quantum ChromoDynamics through the study of jets, since they normally contain a sizeable π^0 or γ component. Denoting the ratio of the response to electromagnetic and hadronic particles by e/h, the ZEUS calorimeter has a value $e/h = 1.00 \pm 0.05$, while a non-compensating calorimeter may have e/h in the range $1.10 \rightarrow 1.35$.

The use of scintillators and photomultiplier tubes keeps the response time to less than one bunch crossing (96 ns), which reduces pile-up effects due to information overlapping between one event and the next. The uranium absorber is an alloy consisting of 98.2% ^{238}U, 1.7% Nb and 0.2% ^{235}U, which has a density of 18.5 gcm^{-3}.

The mechanisms by which electromagnetic and hadronic particles lose energy in the calorimeter are different, which allows differentiation of the two to be made by the calorimeter. Both types of particles create *showers* in the detector and hence lose energy. The UCAL is therefore separated in the x-y plane into the electromagnetic and hadronic calorimeters. The geometry of these is illustrated in figure 3.9

Electromagnetic particles lose energy through two processes, radiation and ionisation. As the particle passes through the detector's absorbing medium, which is depleted uranium in the

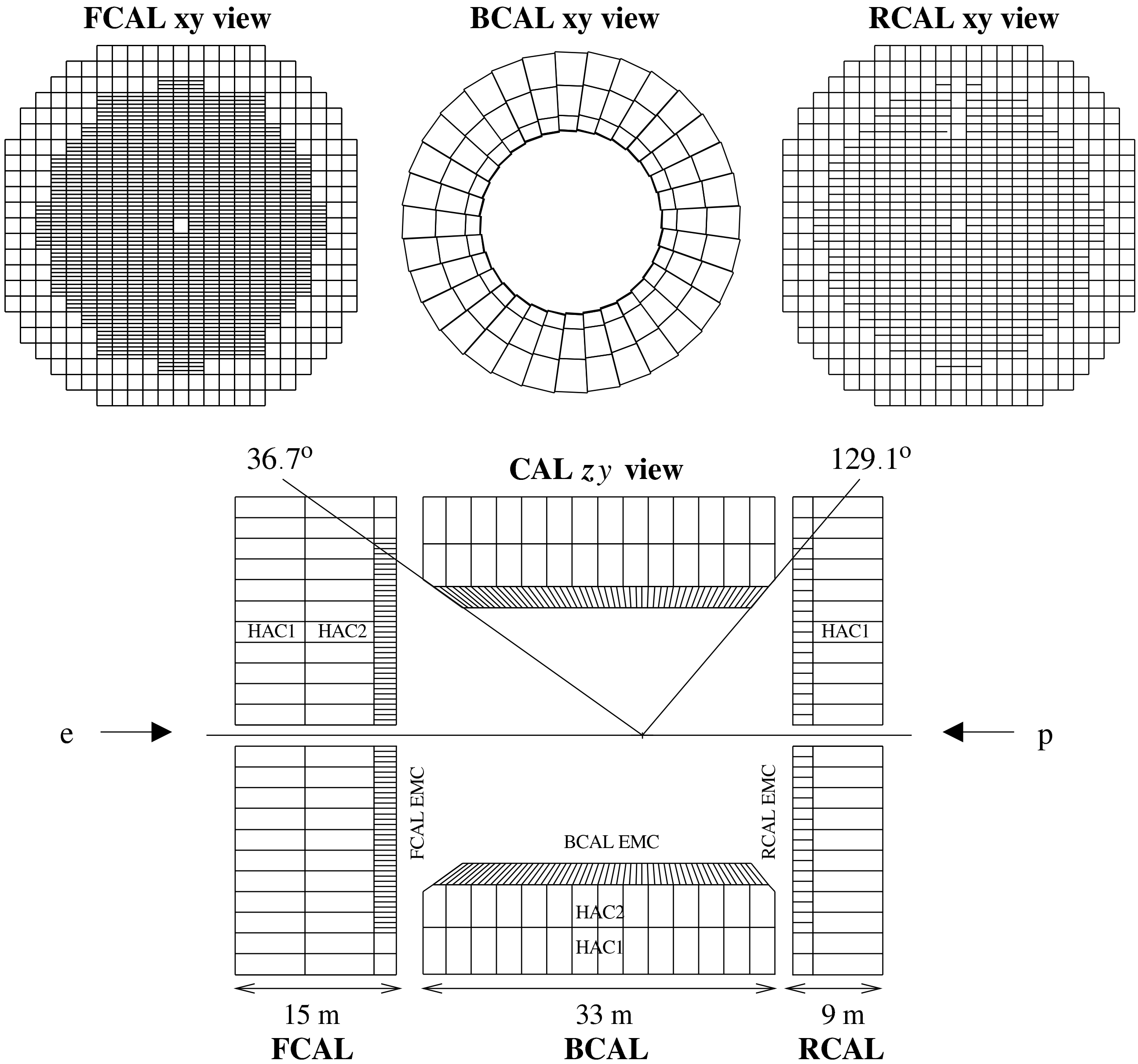

Figure 3.8: A schematic representation of the UCAL, displaying the FCAL, BCAL and RCAL and the geometry of each section. The projective geometry of the BCAL, essential to an effective background subtraction in the prompt photon analysis, is clearly visible, although it is shown in more detail in figure 3.11.

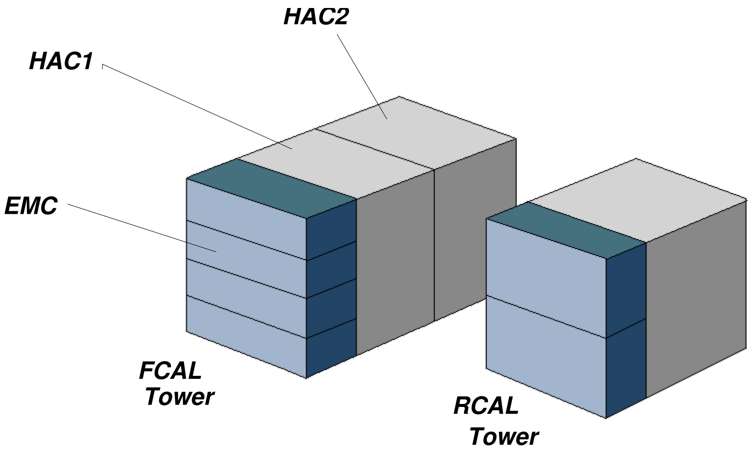

Figure 3.9: A representation of the variations in geometry comparing the hadronic and electromagnetic sections of the forward and rear UCAL.

case of the ZEUS calorimeter, the particle radiates photons, which can then split into e^+e^- pairs, causing a shower of particles in the detector. Low mass particles, such as electrons, lose most of their energy in this way.

Hadronic particles are of higher mass, and can interact with the material in the detector through the nuclear force as well as through the electromagnetic force. Thus, hadronic particles can interact with the nuclei of the absorbing material. They also form ion-electron pairs, which shower in the detector. Hadronic showers have a broader shape than electromagnetic showers, and also penetrate more deeply into the detector, since hadronic particles have a longer interaction length.

The UCAL weighs 700 tons and covers 99.8% of the total angular region. It is divided into cells, which measure 5 $\times$ 20cm for the electromagnetic calorimeter and 20 $\times$ 20cm for the hadronic calorimeter, where the finer resolution is necessary for resolution of the shallow, narrow electromagnetic showers. The calorimeter has a total of 6,000 cells. There are two photomultiplier tubes per cell, giving a total of 12,000 readout channels.

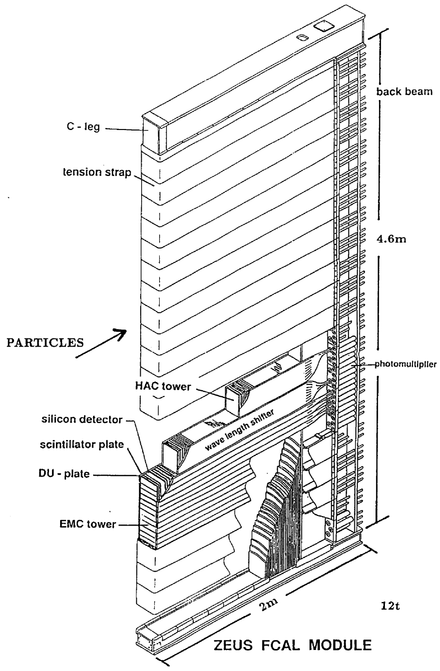

Figure 3.10: One module of the FCAL.

The calorimeter is divided into three regions, the FCAL, BCAL and RCAL in the forward, barrel and rear regions respectively. The FCAL covers an angular region of $2.6° < \theta < 36.7°$, the BCAL covers a region of $36.7° < \theta < 129.1°$, and the RCAL covers $129.1° < \theta < 176.2°$, as illustrated in figure 3.8. Each region is separated into towers longitudinally, where the electromagnetic towers have a depth of 5 radiation lengths or 1 nuclear interaction length, and the hadronic towers have a depth of between 4 and 6 nuclear interaction lengths. The length of the hadronic sections has been designed such that 90% of incident hadrons should deposit 95% of their incident energy there. Figure 3.10 shows one FCAL module.

The energy resolution of the calorimeter is optimised for jets. Based on test beam data, the energy resolution of the ZEUS UCAL is given by

$$\frac{\sigma(E)}{E} = \frac{35\%}{\sqrt{E}} \oplus 1\%$$

where E is measured in GeV. For electromagnetic particles, the UCAL provides an energy resolution given by

$$\frac{\sigma(E)}{E} = \frac{17\%}{\sqrt{E}} \oplus 1\%$$

The UCAL provides an angular resolution for jets of better than 10 mrad.

The BACking calorimeter, BAC, is located outside the UCAL and provides a means by which the extent of energy loss by leakage of high-energy particles can be estimated. While the UCAL uses Uranium as an absorbing medium, the BAC uses iron, which further provides a path for the return field from the superconducting magnets. The iron is interspersed with proportional counters. The energy resolution of the BAC is

$$\frac{\sigma(E)}{E} = \frac{100\%}{\sqrt{E}}$$

where E is in GeV.

3.6.1 The barrel calorimeter

The Barrel CALorimeter, BCAL, is used extensively in the search for prompt photons, and is thus described in more detail.

The BCAL covers an angular region of $36.7^\circ < \theta < 129.1^\circ$ and 100% of the azimuthal range. It is divided into 32 modules, each of which is rotated by 2.5° azimuthally, around an axis parallel to the beam axis and 2.3 m away from it. This, coupled with the wedge-like shape of the modules, ensures that the wavelength shifter plates do not point to the beam axis, hence preventing photons from being lost in the cracks between modules.

Each BCAL module is divided into three sections. The first, the EMC, is nearest the beampipe and is used for locating electromagnetic energy deposits. Behind this are two further hadronic sections, HAC1 and HAC2. The EMC has 53 towers, projective in polar angle, with

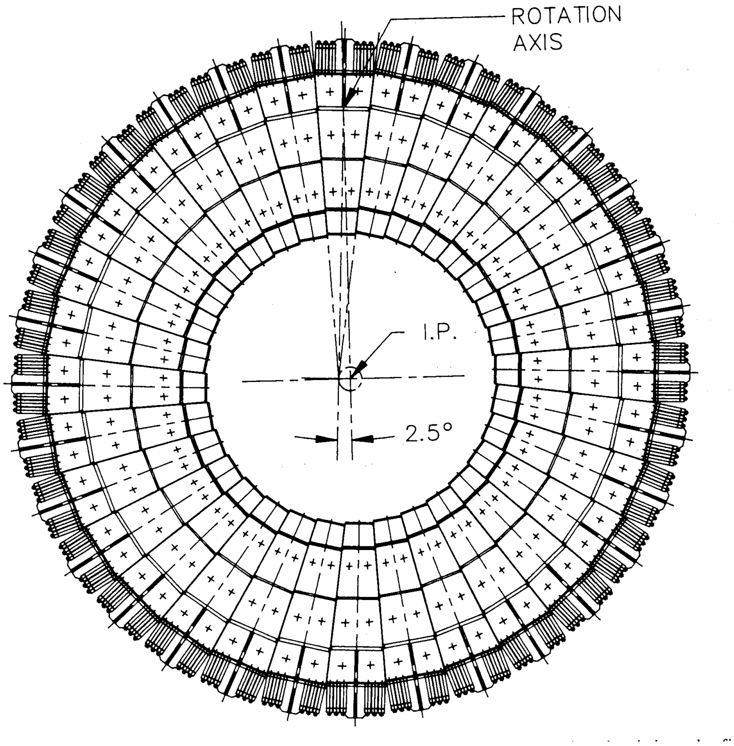

Figure 3.11: A schematic representation of the BCAL, showing the projective geometry.

dimensions of 49 × 233 mm^2 on the front face. The 14 HAC sections are non-projective.

Using projective geometry in the barrel region ensures that the plane face of each cell is oriented towards the interaction point. This minimises the risk of having particles lost in the cracks between cells. In the case of the prompt photon analysis, the projective geometry in the BCAL allows for better reconstruction of the shape of the photon signal, thus providing the necessary tools which allow discrimination between signals due to prompt photons and signals which originate from the decay of neutral mesons.

Each hadronic tower covers 4 EMC towers, excepting only the most forward tower, which covers only two. The BCAL has a depth corresponding to one nuclear interaction length.

3.6.2 The barrel presampler

A Presampler provides a link between tracking detectors and calorimeters. It allows for more accurate determination of the precise starting point of an electromagnetic shower, better distinction between a true electron and a false signal caused by the overlap of a π^0 and a charged track, and improved hadron-electron distinction. The ZEUS Barrel Presampler, BPRE, was installed in 1999 and is situated within the Barrel section of the ZEUS UCAL, although prior to this there were presampler detectors in the front and rear directions, which consist of one 5mm thick plastic scintillator read out by wavelength-shifting fibres.

The BPRE counts the number of charged particles passing through it, and hence the given signal is proportional to the energy loss of the original incident particle. Thus, the BPRE can be used to correct the measured energy for the energy loss due to dead material encountered by the particle between the interaction point and the calorimeter. The BPRE consists of 32 cassettes, each with 13 scintillator tiles, oriented along the $+z$ direction. Each cassette is aligned with one of the 32 modules of the BCAL. Each tile is 18 × 20cm and 5mm thick. The signal from the scintillator is registered by a photomultiplier tube.

3.7 The trigger system

An effective trigger system is essential for a high energy physics experiment owing to:

- the fast event rate,
- the large proportion of non-interesting events and background, and
- the limited computer-storage capability.

ZEUS uses a three-level trigger system, portrayed schematically in figure 3.12

3.7.1 First Level Trigger

The First Level Trigger, FLT, provides an initial indication of the event. The information used at the first level is very basic, and this trigger serves to reduce the 10MHz rate to below 1 kHz.

Each component has its own first-level sub-trigger which is hardware based. No component can make a decision at the first level within the bunch-crossing time of 96 ns, therefore pipelines are used which store the data for 4.4μs, corresponding to 46 bunch crossings. This use of pipelines ensures that the trigger process has small or zero deadtime, since data collection may continue while an event is being processed. Each component-based sub-trigger must reach a decision within approximately 2μs after the bunch crossing. These decisions are based on limited tracking information and some global or local energy sums from the ZEUS UCAL. The decisions from each component are passed to the Global FLT, GFLT, which must then make a decision within the 4.4μs available.

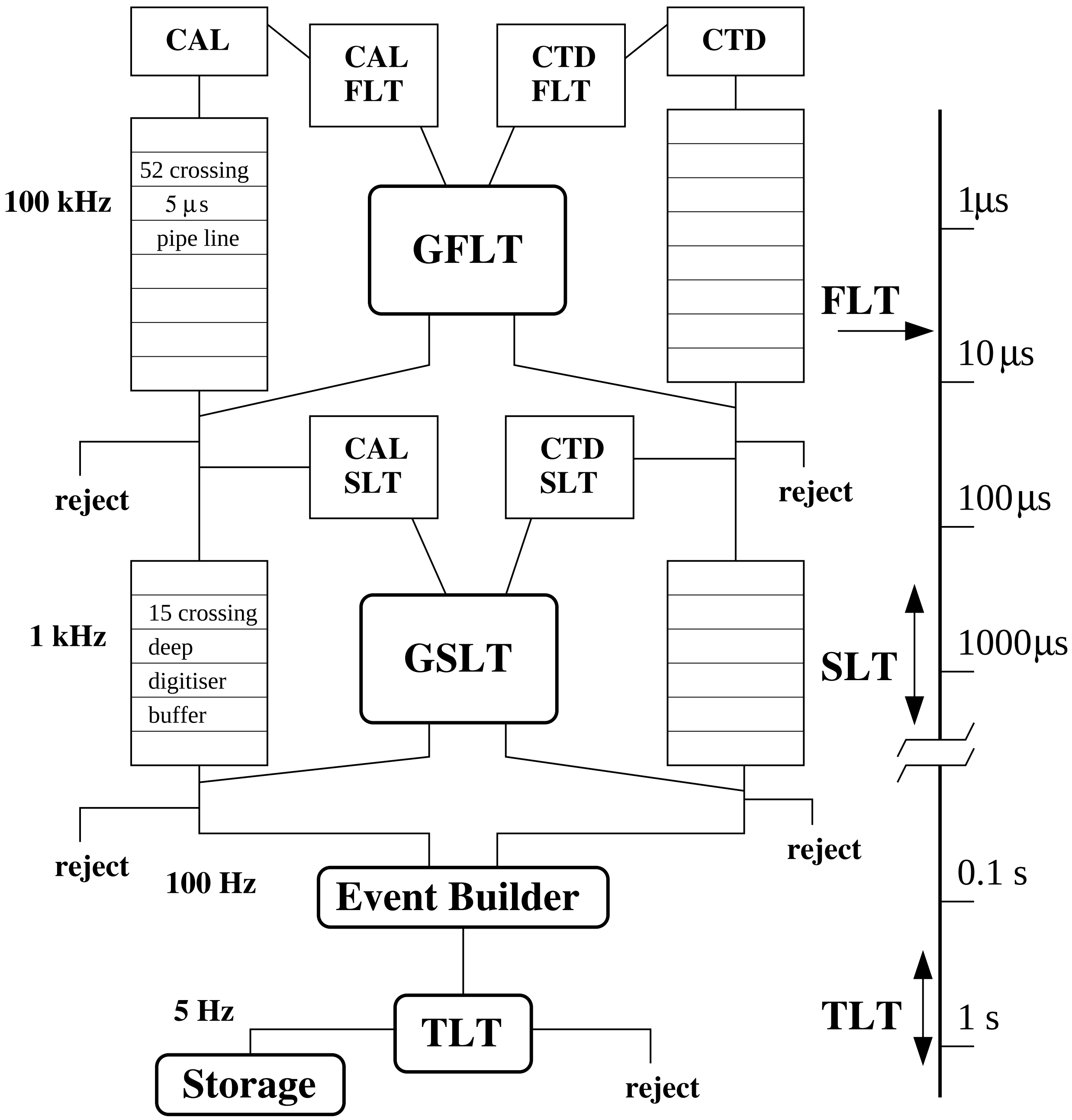

Figure 3.12: A schematic representation of the ZEUS trigger system.

This necessary speed requires a substantial compromise in selection purity. Approximately 98% of events passed at this stage are background events. The remainder are passed to the Second Level Trigger, SLT.

3.7.2 Second Level Trigger

The SLT is a software-based trigger system. Analogously to the FLT, the SLT uses component-based sub-triggers, which now have more detailed event information available on which to make a decision. The decisions of the individual component triggers are then passed to the Global SLT, GSLT. The SLT reduces the acceptance rate to approximately 100Hz from 1kHz.

The component SLTs use basic vertex information provided from tracking information as well as information from the UCAL, including timing information or energy sums, such as E_T or $E - p_Z$. The GSLT provides a decision within a few milliseconds. The decision is then passed to the Event Builder, EVB, which then combines component data into a single record of the event for use by the Third Level Trigger.

3.7.3 Third Level Trigger

The TLT is a software trigger which further reduces the rate to approximately 3-5Hz. The TLT bases its decision on the reconstructed event using a modified version of the offline reconstruction software. The TLT has information available regarding the kinematic properties of the event. It can also perform more detailed vertex-finding than is available at the SLT, and can further perform basic jet-finding. The TLT then classifies the *ep* events into physics types based on filters provided by the physics groups.

Events which pass the TLT are written to tape via a tape-robot, using a direct link-up to the DESY computer-storage centre. Each event is approximately 0.3MB.

Chapter 4

Simulation and Monte Carlo Generators

4.1 Introduction to Event Generators

A Monte Carlo program is a routine which is commonly used in many areas which rely heavily on statistical methods of simulation. Such programs use the generation of random numbers to recursively generate the time-dependence of an evolving system. In particle physics, such programs tend to be used as event generators.

In this analysis, three distinct sources of Monte Carlo are used. A prompt photon sample is obtained using PYTHIA, which models direct and resolved photoproduction processes. A cross-check is provided by means of the HERWIG Monte Carlo generator. In order to accurately model the neutral meson background, the single-particle generation facility of JetSet is used to provide a sample of simulated neutral pions, eta mesons and photons. These are an essential part of the background subtraction process. Monte Carlo samples are also used to provide acceptance corrections for the purpose of cross section measurements.

The PYTHIA and HERWIG generators contain many common features. Each assumes that the hard process may be factorised into the amplitude of the hard scattering at lowest order, initial- and final-state radiation, final state non-perturbative radiation and initial state parton evolution. The process of generating the events is broadly similar for the two generators, and may be divided into the following steps.

- Incoming partons:

  The behaviour of the incoming particles is characterised by the Parton Distribution Function, PDF, chosen by the user. For each initial hadron, one parton initiates a parton shower, while the remainder contribute to the beam remnant. Remaining partons may also be involved in multi-parton interactions.

- Initial-state showers:

  One parton from each incoming particle begins a series of branchings involving gluon radiation and gluon splitting into pairs of lower-energy partons, beginning with low-virtuality particles.

- Elementary hard sub-process:

  The hard sub-process determines the nature of the generated event. At this stage, one parton from each shower takes part in a hard interaction.

- Final state showers:

  The final-state partons undergo branching, generating final-state parton showers.

- Hadronisation:

  Final state particles generate a set of colour-neutral hadrons. This is described in more detail below.

- Decay of unstable particles:

  The resultant hadrons may undergo allowed decays until stable particles are reached.

The differences between HERWIG and PYTHIA are most notable in the treatment of perturbative radiation and non-perturbative fragmentation.

4.2 PYTHIA

The PYTHIA [19] Monte Carlo Generator is a combined generator developed from the previous JetSet and PYTHIA generators. The name PYTHIA comes from the oracle once based at Delphi, to whom the rich and powerful of the ancient world would go for answers to their problems.

In PYTHIA, the description of the fragmentation process is based on the 'Lund string model'. In this model, the long-range confinement forces – which prevent quarks and gluons from escaping as real particles – distribute the energies and flavours of generated partons between a set of hadrons, which may subsequently decay. In practice, this is implemented by linking each parton by a *string* of energy of the order $1\,\mathrm{GeVfm}^{-1}$. As the partons separate the energy of the string increases until it finally breaks, causing the production of a quark-antiquark pair. When a particular string has too little energy for further separation, the partons at either end of the strings form hadrons.

For PYTHIA, the scale, μ^2, is taken to be the mean transverse mass of the outgoing hadrons, m_T^2. That is,

$$\mu^2 = m_T^2 = \frac{1}{2}(m_1^2 + p_{T,1}^2 + m_2^2 + p_{T,2}^2)$$

with m_i and $p_{T,i}$ representing the mass and transverse momentum of parton i. The evolution of the partons in both the initial- and the final-states is ordered in terms of the virtuality of

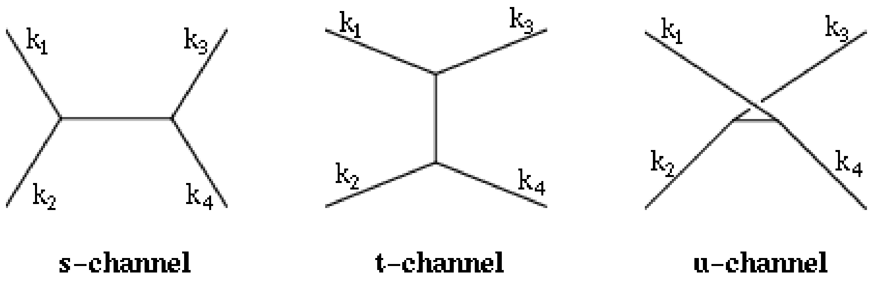

Figure 4.1: The Mandelstam variables displayed. Here, $k_1 = p_1$, $k_2 = p_2$, $k_3 = p_3$ and $k_4 = p_4$.

the parton in question.

4.3 HERWIG

HERWIG [20] stands for Hadron Emission Reactions With Interfering Gluons. In calculating the perturbative parton shower, HERWIG uses the lowest-order matrix elements and includes the effects of coherence and interfering gluons. The aim is to provide as complete a description of the underlying perturbative QCD process as possible.

The factorisation scale in HERWIG is given by

$$\mu^2 = \frac{2stu}{s^2 + t^2 + u^2}$$

where s, t and u are the Mandelstam variables for the hard scatter, defined as follows

$$s = (p_1 + p_2)^2 = (p_3 + p_4)^2$$

$$t = (p_1 - p_3)^2$$

$$u = (p_1 - p_4)^2$$

where p_i is the four-momentum of particle i. The variables are displayed in figure 4.1.

In order to avoid the resultant divergence of the cross section in the limit $p_T \rightarrow 0$, a minimum p_T cut is introduced.

In HERWIG, the parton showers are generated by a *coherent branching* algorithm. A single parton splits into multiple partons, forming leading-logarithm parton showers ordered in terms of the opening angle between them. The hadronisation process in HERWIG uses a cluster-based algorithm. That is, within the parton shower, colour-neutral clusters are formed which are fragmented into hadrons. Any cluster which is too light to decay into two hadrons is assumed to be the lightest single hadron of its flavour. Heavier clusters are allowed to decay into pairs of hadrons.

4.4 Monte Carlo samples

Monte Carlo samples for the analysis are generated using Amadeus [21]. Amadeus is a ZEUS-specific software package which provides a standard interface between the user and multiple Monte Carlo generators. The user uses control cards to customise the generated sample of Monte Carlo according to the needs of the analysis.

4.4.1 PYTHIA sample

PYTHIA version 6.1 is used to generate a sample of prompt photon events from both the direct and resolved processes. The generated sample is made up of 211.04 pb^{-1} from direct events and 202.72 pb^{-1} from resolved.

In both cases, the proton PDF is GRV94 LO and the photon PDF is SaS2D. The processes simulated are $f_i\gamma \rightarrow f_i\gamma$ for the direct case and $f_i g \rightarrow f_i\gamma$ and $f_i\bar{f}_i \rightarrow f_i\gamma$ for resolved, where f_i represents a fermion, g represents a gluon and γ represents a photon, as is usual.

4.4.2 HERWIG sample

Similarly, the HERWIG generator version 6.1 is used to provide a sample of prompt photon events from both direct and resolved photons. The sample is made up of 860.64 pb^{-1} of direct and 776.24 pb^{-1} resolved events. The proton structure was taken in terms of the GRV94 LO parton distribution function, PDF, while the photon PDF was SaSph, that is, the Schuler-Sjostrand parton distribution function [22].

PYTHIA provides a better direct comparison to the data as compared to HERWIG. PYTHIA is therefore chosen to provide the Monte Carlo comparisons and corrections by default. As a systematic check, HERWIG is used in place of PYTHIA for the energy and y_{JB} corrections and for the acceptances. In this case, the HERWIG distributions are weighted as described in section 4.4.3 to match the E_T of the photon in the data, providing a better agreement with the observed distributions.

4.4.3 Monte Carlo weighting

In order to compare the samples with the data, the Monte Carlo samples must be weighted to match the available luminosity of the data. In this analysis, in the case of the photon plus jet analysis, the samples are weighted twice. First, a fit to the x_γ distribution is performed, which provides the ratio of direct photoproduction events to resolved photoproduction events (see section 2.7). This is then taken into account, and the Monte Carlo samples are then weighted such that the area of the y_{JB} distribution is the same for Monte Carlo and data. This provides a good quantitative fit to the data. For the inclusive process, the x_γ distribution becomes essentially meaningless, as too little of the total energy in the event is taken into account in the measured variables. Therefore in the inclusive plots, the ratio of direct to resolved is taken to be the ratio of the luminosities as provided by the Monte Carlo program.

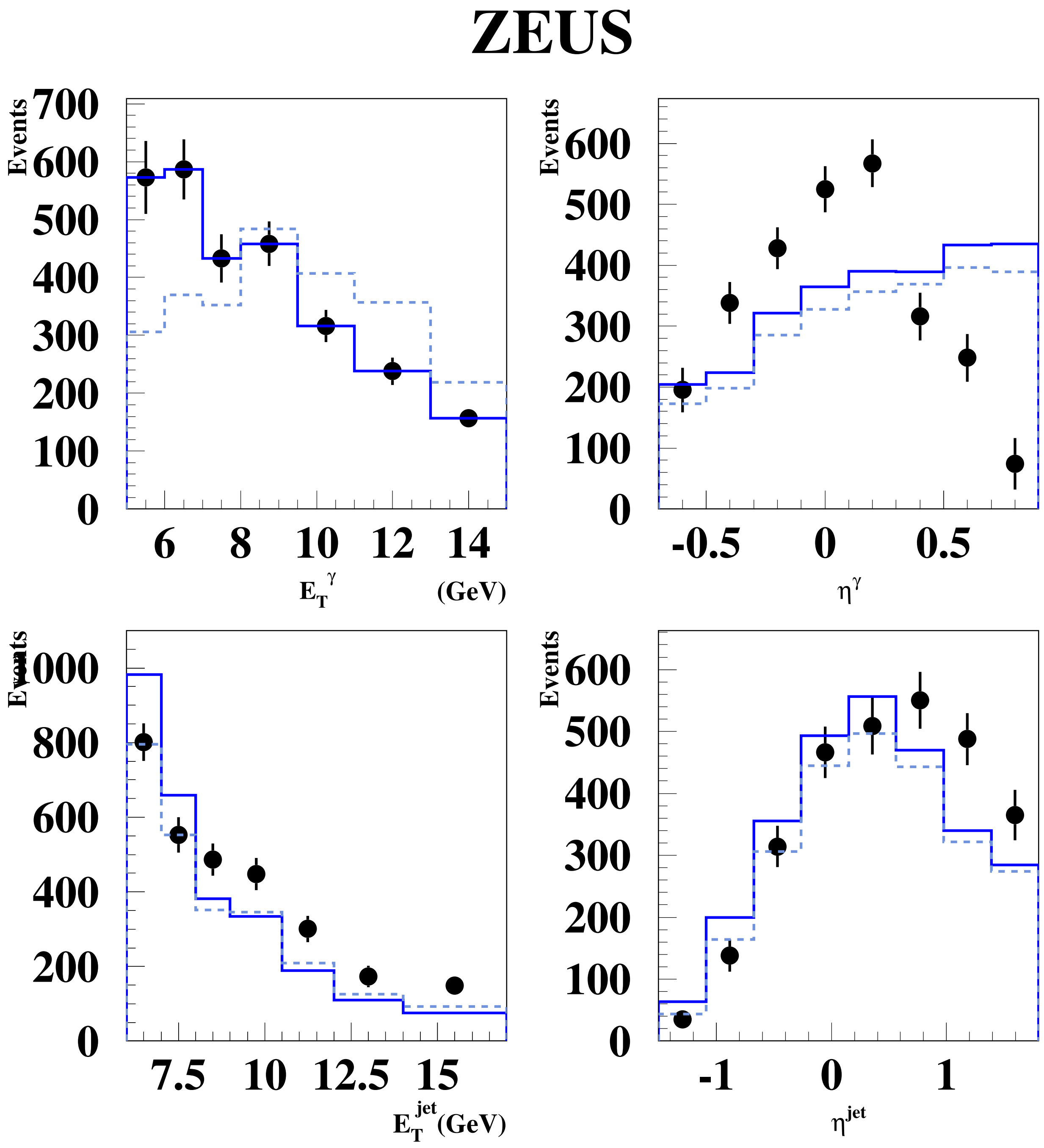

Figure 4.2: The comparison to HERWIG for E_T^γ, η^γ, $E_T^{\rm jet}$ and $\eta^{\rm jet}$, where the points show the data. The solid histogram shows the HERWIG where the histogram has been weighted in E_T^γ to match the distribution of the data. The dashed histogram shows the distribution without such weighting. The fit is sufficiently improved that the weighting is adopted for the photon plus jet analysis.

In the jet analysis only, this alone was insufficient to allow HERWIG to provide a reasonable description of the data. The HERWIG distribution was therefore further weighted such that the E_T^γ distribution of the HERWIG sample and that of the data agree. This was done by a straightforward bin-by-bin weighting. Figure 4.2 shows the effect the weighting has on the four key variables for the photon plus jet analysis: E_T^γ, η^γ, $E_T^{\rm jet}$ and $\eta^{\rm jet}$. The distributions are noticeably improved by the inclusion of the weighting factor.

4.5 Single particle Monte Carlo

A major contribution to the signal found comes from neutral mesons, as described in section 2.8. In order to discriminate between true prompt photon candidates and those that result from decays of neutral mesons, it is necessary to model the behaviour of these mesons. The details of the subtraction are given in more detail in chapter 6.

Single particle Monte Carlo samples are generated of π^0 and η mesons to model the shower behaviour of the background, and a single-γ sample is also generated to similarly model the signal. JetSet 7.4 [23] is used to generate samples with a flat distribution in E_T. An improvement to the single-γ Monte Carlo is provided by using instead the experimental DVCS data as described in chapter 6, although the single photons from JetSet remain, to be used as a cross-check.

After passing through the simulation of the detector, described in section 4.6, the single particles are weighted to match the E_T^γ spectrum of the prompt photon data. This is an approximation of the truth, as it is difficult to obtain a sample of observed isolated neutral mesons in the required energy range. However, the resultant sample achieves a fair agreement with the data in the shower shape fits, which can be seen in chapter 6.

4.6 Detector simulation

The generated events must be passed through a simulation of the detector [24] to allow the detector response to be simulated. The detector simulation for ZEUS is carried out by MOZART (MOnte carlo for ZEUS Analysis, Reconstruction and Trigger), originally based on the GEANT [25] program developed at CERN. MOZART includes a complete description of the detector with regards to the component materials and positions, and simulates the passage of a particle through the detector, taking into account the particle decay, energy loss due to dead material, and multiple scattering.

The development of hadronic showers is dealt with by the program GHEISHA, while the ZEUS trigger decision is simulated by ZGANA. The ZEUS offline and Monte Carlo chain is illustrated in figure 4.3.

ZEPHYR, the ZEUS physics reconstruction program, accepts input from either MOZART and ZGANA or from the ZEUS detector, and reconstructs the physics variables. First, the individual detector components are reconstructed, then a track-matching and vertex-finding algorithm is run. Finally, particle identification is carried out.

ZEUS event reconstruction uses the ADAMO (Aleph DAta MOdel) system, which groups the ADAMO tables into logical dataflows.

4.7 Efficiencies, purities and acceptances

In order to produce hadron-level results, it is necessary to correct the measured quantities for all detector effects. This is done using Monte Carlo samples, for which both the true value and the value after detector reconstruction are known for each event. Differences between the truth level and the measured detector-level quantities may thus be allowed for.

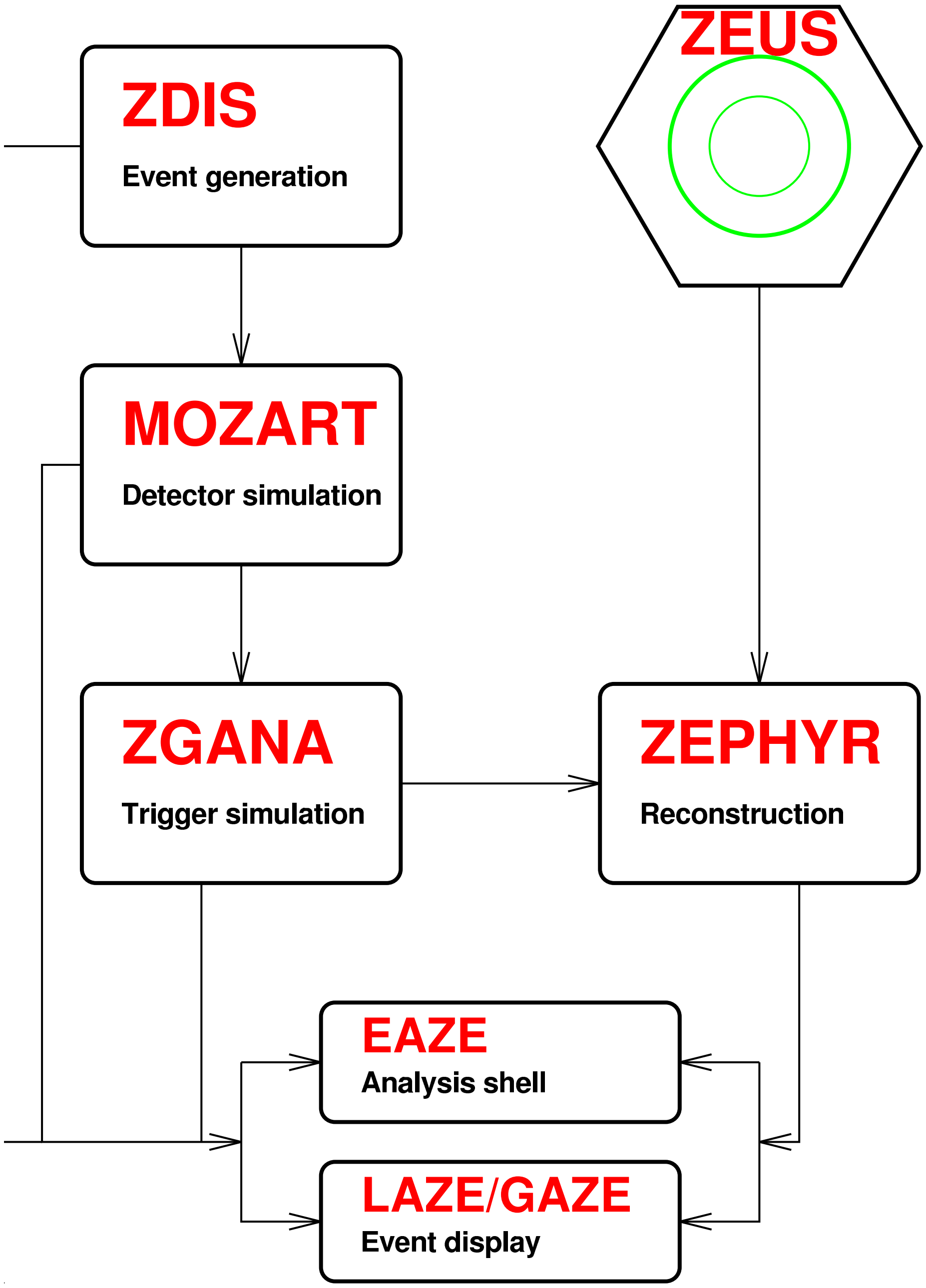

Figure 4.3: The ZEUS offline and Monte Carlo chain.

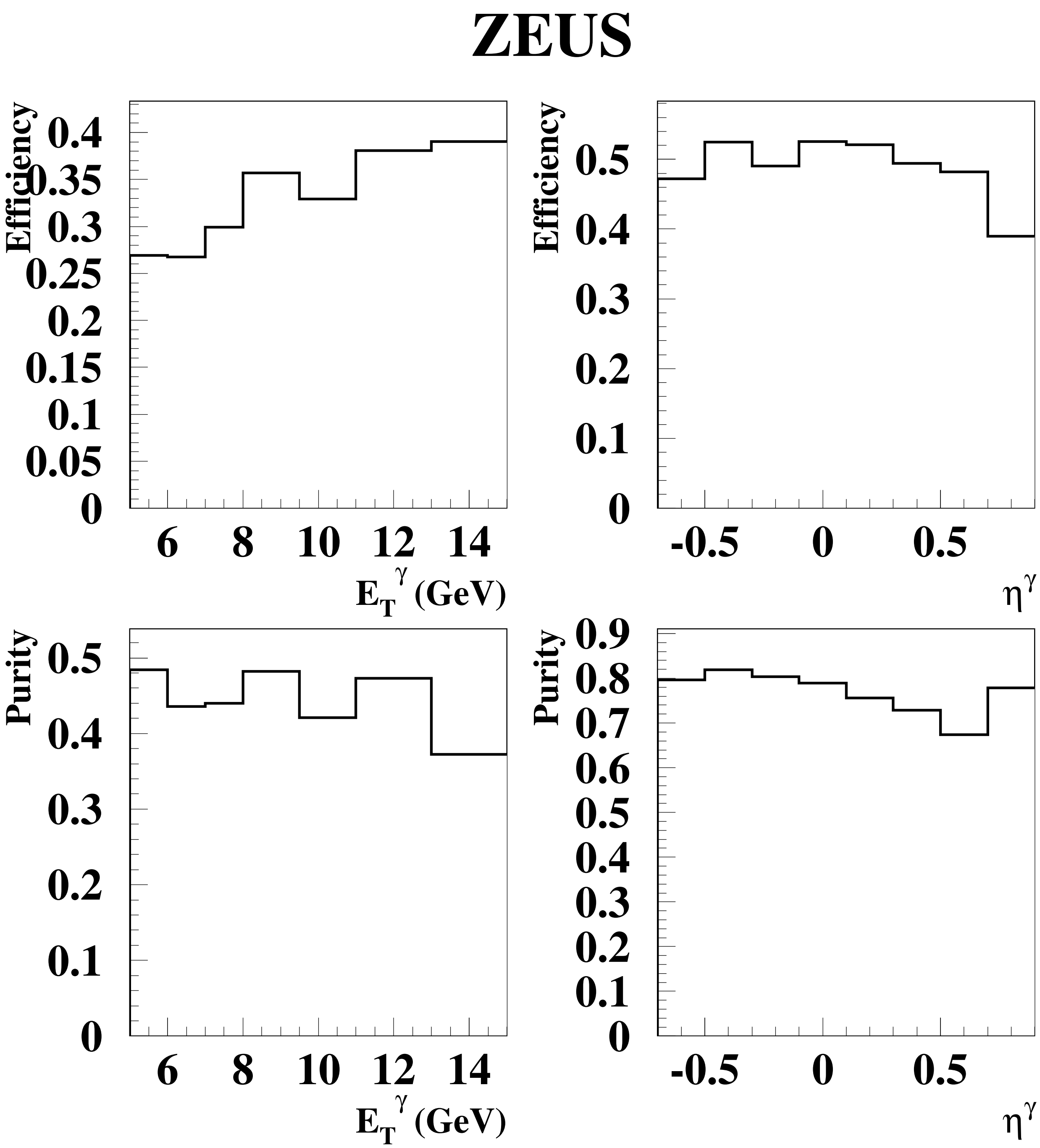

Figure 4.4: The efficiencies as calculated with respect to E_T^γ and η^γ for the inclusive analysis are shown in the top plots. The lower plots show the purities.

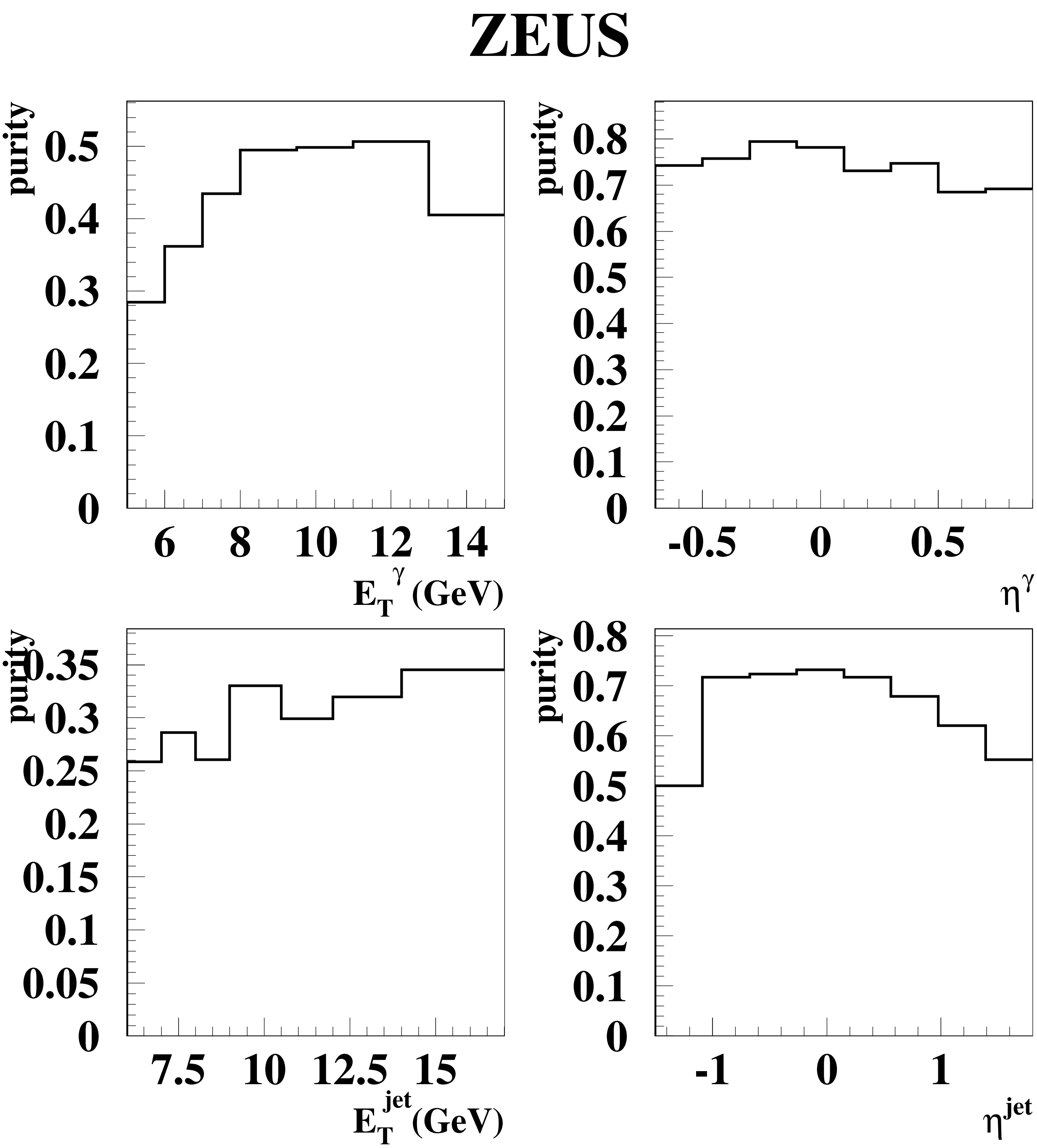

Figure 4.5: The purities as calculated with respect to E_T^{γ}, $E_T^{\rm jet}$, η^{γ} and $\eta^{\rm jet}$ for the photon plus jet analysis.

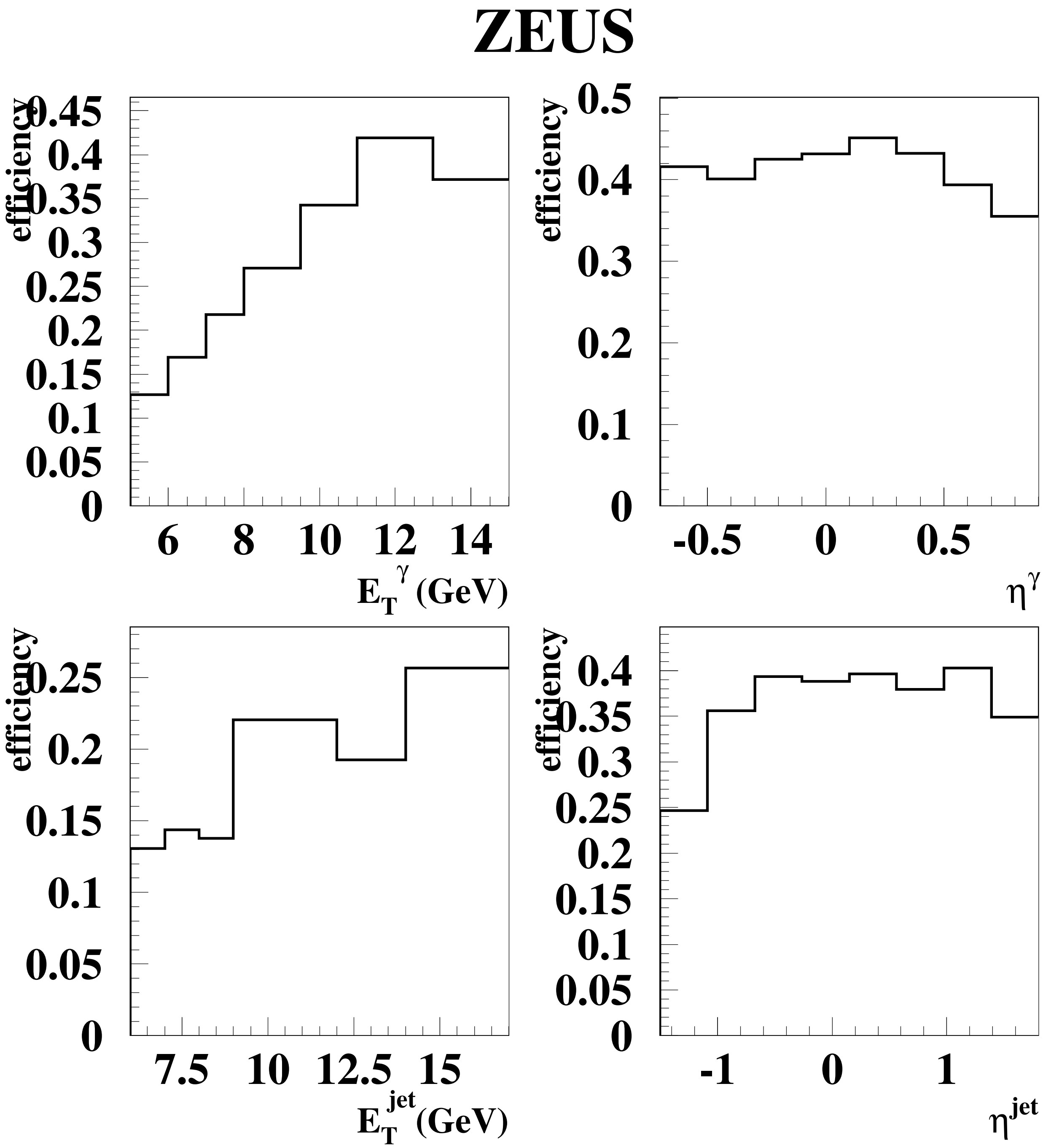

Figure 4.6: The efficiencies as calculated with respect to E_T^{γ}, $E_T^{\rm jet}$, η^{γ} and $\eta^{\rm jet}$ for the photon plus jet analysis. There are some statistical fluctuations, particularly for the jet variables.

Such corrections are known as *acceptance* corrections. They are calculated by means of the *purity* and *efficiency* of the measurement on a bin-by-bin basis for each relevant quantity.

In bin i, let G_i be the number of events generated in the bin, R_i be the number of events reconstructed in the bin, and B_i be the number of events which are both generated and reconstructed in the same bin in a Monte Carlo sample. The the efficiency of the event in bin i, e_i, is given by

$$e_i = \frac{B_i}{G_i}$$

and the purity in bin i, p_i, is given by

$$p_i = \frac{B_i}{R_i}$$

Therefore e_i measures the fraction of generated events which are reconstructed in the same bin, while p_i measures the fraction of reconstructed events which have been generated in the same bin.

The acceptance correction in bin i, A_i, is defined as

$$A_i = \frac{e_i}{p_i} \equiv \frac{R_i}{G_i}$$

Dividing the measured signal by the acceptance correction A_i corrects the measured quantities for the effects of passing through the detector.

If the statistical error on e_i is denoted by ϵ_i and the statistical error on p_i is denoted by π_i, then

$$\epsilon_i = \sqrt{\frac{(1-e_i)e_i}{G_i}}$$

and

$$\pi_i = \sqrt{\frac{(1-p_i)p_i}{R_i}}$$

The statistical error on A_i, δA_i, is therefore given by

$$\delta A_i^2 = (\frac{\epsilon_i}{p_i})^2 + (\frac{e_i \pi_i}{p^2})^2 = \frac{e_i}{G_i R_i p_i^3} \left(p_i R_i (1-e_i) + e_i G_i (1-p_i)\right)$$

The efficiencies and purities as calculated for the inclusive analysis are shown in figure 4.4. Figure 4.6 gives the efficiencies for the jet analysis, while the purities are shown in figure 4.5. As is expected, the efficiencies and purities are slightly less flat for the jet variables, which are harder to describe with Monte Carlo, than the photon variables.

Chapter 5

Event Selection and Reconstruction

The technical details of the analysis are described in this chapter. Firstly, the ZEUS-standard code which is used for the analysis is described. The different cuts placed on the data are then detailed, and the correction routines applied to the y_{JB}, E_T^{γ} and E_T^{jet} distributions are described. The control plots are shown, and the comparison between the Monte Carlo samples and the photons variables and, where appropriate, the jet variables are shown.

The cuts used in the 'dijet' analysis are given at the end of the chapter. There are some differences in the values of various cuts between the two analysis methods above and beyond the differences in the methods themselves. In order to draw a fair comparison, the cuts used in this analysis were changed to agree more completely with the dijet method for the purposes of the comparison. Elsewhere, the cuts are as detailed in the beginning of this chapter.

5.1 ZEUS standard code

Since the analyses performed at ZEUS contain many common features, it is sensible to develop tools which allow such analyses to be performed with maximum efficiency. Over the years, many such software tools have been developed. Those which are relevant to the discussion of this analysis are described in the following sections.

5.1.1 ZEUS Event Store

The Zeus Event Store, ZES, [26] is an object-oriented database of ZEUS events. Since it works by means of tags, it provides faster access to preliminary event information, allowing a fast preliminary selection of relevant events. Selection can be made at this stage according to various stored and tagged properties of the event.

Preliminary event selection is permitted using information such as the trigger bit selection, the $E - p_Z$ of the event, the presence or absence of a scattered lepton, and the $y_{\rm el}$ of the event, where

$$y_{\rm el} = 1 - (\frac{E_{e'}}{2E_e})(1 - \cos\theta_{e'})$$

Events which pass this preliminary selection process are passed to the main code for further, more detailed analysis.

5.1.2 EAZE and ORANGE

The Effortless Analysis of ZEUS Events, or EAZE [27], framework for analysis code provides a standard format which simplifies the process of writing code. There are two important parts of the structure from the perspective of the user.

The first of these is the control cards file. In this file, various preliminary calls can be made to select the data to be processed, by means of turning on standard control cards. This allows general code steering.

The second part is the user code, which is called in three stages. Initially, the code is set up and any required declarations are made. Then a second routine takes over which is run

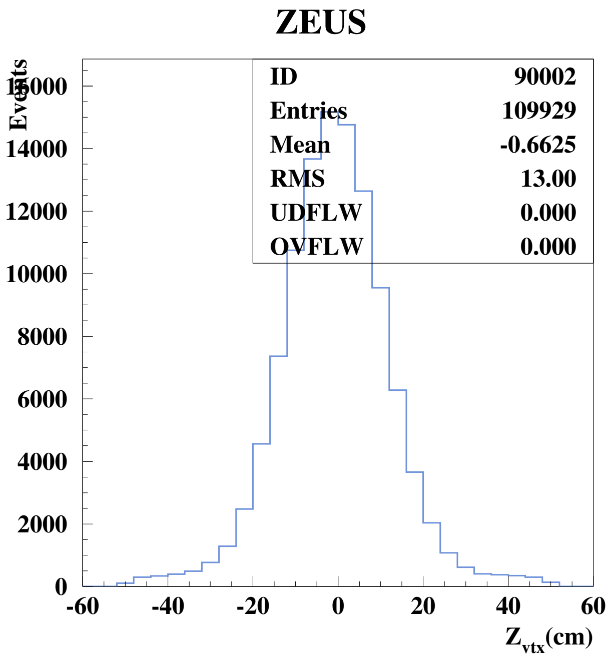

Figure 5.1: The $Z_{\rm vtx}$ distribution of the data with only cleaning cuts and broad selection cuts (such as a possible photon candidate existing in the event) applied.

over each of the data selections. This is where most of the cuts are performed and where the preliminary analysis is performed. Finally, any closing requirements are performed.

ORANGE, Overlying Routine for Analysis Ntuple GEneration [28], is a software program which works within the EAZE framework. ORANGE, however, has a more detailed set of control cards, which use standard and centrally-maintained code to begin the job of analysing the information. This substantially reduces the amount of time required to build up analysis code, and also, since the code is centrally-maintained, increases the reliability of the code used.

In this analysis, ORANGE has been used to perform the preliminary event selection and to reject known bad events.

5.2 Event selection

Preliminary cuts make use of the ZES system (see section 5.1.1). This makes a very early selection on the basis of the third level trigger selection DST bit 79. This trigger bit requires:

- Second Level Trigger bit 6 is set
- There exists an electron candidate with energy $> 3.5\,\mathrm{GeV}$ and -2 $< \eta <$ 2.

The SLT bit 6 has the following requirements:

- |Z vertex| < 60cm, or no CTD information.
- At least one good track
- (FLT28 and $E_T^{\mathrm{cone}} > 8\,\mathrm{GeV}$) OR (FLT30 and $E_T^{\mathrm{cone}} > 13\,\mathrm{GeV}$) OR (FLT39 and $E_T^{\mathrm{cone}} > 8\,\mathrm{GeV}$)

At this stage, the requirement that the measured Z_{vertex} obeys the form $-50 < Z_{\mathrm{vertex}} <$ 50cm is applied. The resulting Z_{vertex} distribution is shown in figure 5.1.

5.3 Cleaning cuts

After the preliminary selection afforded by ZES, there are still several non-*ep* events and other background events which are removed by the following selections:

- The BCAL timing is less than 10ns, rejecting PMT spark events.
- Missing p_T should be less than $10\,\mathrm{GeV}$.
- The ratio of non-vertex tracks to vertex tracks should be less than 10.

- To remove contributions from QED-Compton events, it is required that in any event with two electromagnetic clusters, the combined energy of the clusters should be less than 95% of the event energy.

The timing in the BCAL is a useful tool to remove spark events and cosmic events. If the timing registered by the BCAL is too far from the event time, then it can be assumed that the energy deposit is not related to the *ep* collision. The time of 10ns was selected after simulation by the PYTHIA Monte Carlo programme in the previous ZEUS analysis.

Cosmic events, for example, often have large amounts of missing p_T, since they do not originate from beam collisions and are detected primarily in the up-down (i.e. y) direction. Events generated by photomultiplier tube sparks or charged-current events where a neutrino takes the place of a scattered electron are also rejected by the missing-p_T cut. False events generated by PMT-sparks and beam-gas background are also reduced by the cut on the BCAL timing.

5.4 Photoproduction cuts

In order to produce a clean sample of photoproduction events, the following cuts were used:

- No DIS electron candidate

- $0.15 < y_{JB} < 0.7$

  where

$$y_{JB} = \sum_{\text{calcells}} \frac{E - p_Z}{2E_e}$$

The lower cut in y_{JB} rejects any remaining proton-gas events and other backgrounds, such as cosmic events. The upper cut removes DIS events, and also any events which include a lepton

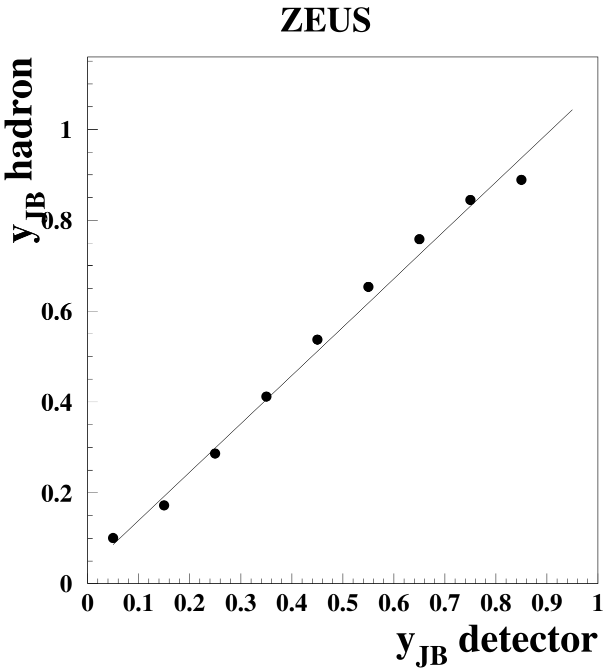

Figure 5.2: The y_{JB} distribution of the data is corrected using the fit to the points shown.

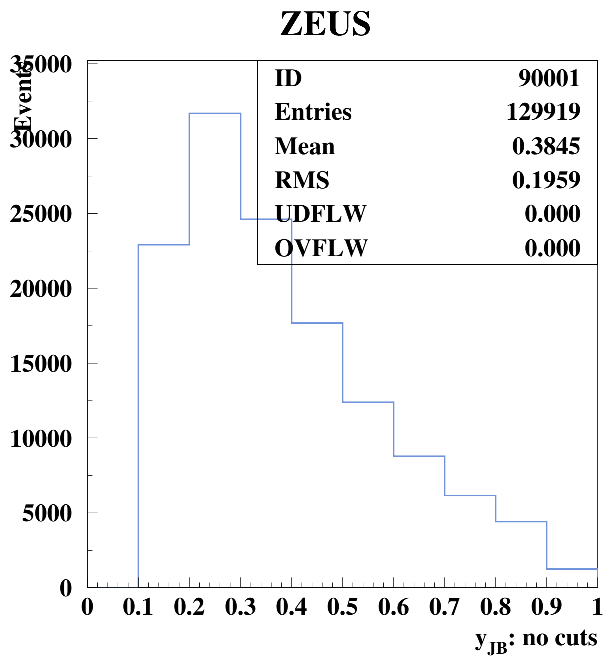

Figure 5.3: The y_{JB} distribution of the data with only cleaning cuts and broad selection cuts (such as a possible photon candidate existing in the event) applied. Cuts are placed at 0.15 and 0.7. The data have been corrected as described in the text.

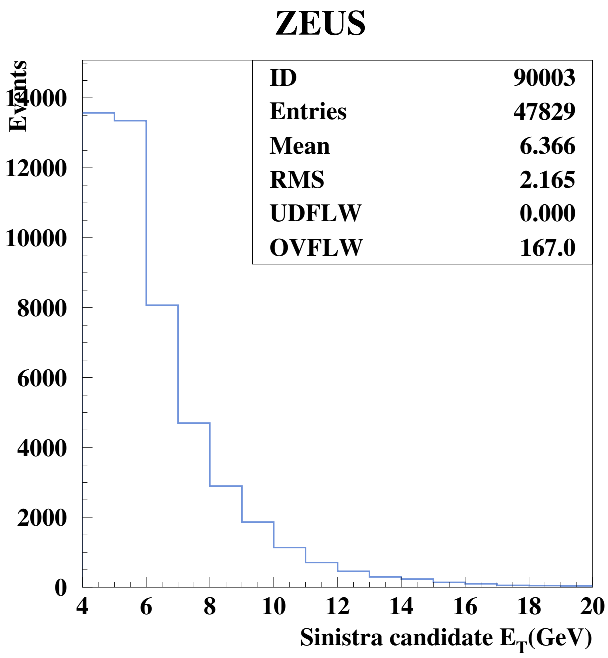

Figure 5.4: The transverse energy of electron candidates found by the Sinistra electron finder. At this stage, the y_{JB}, track and energy isolation criteria have been met.

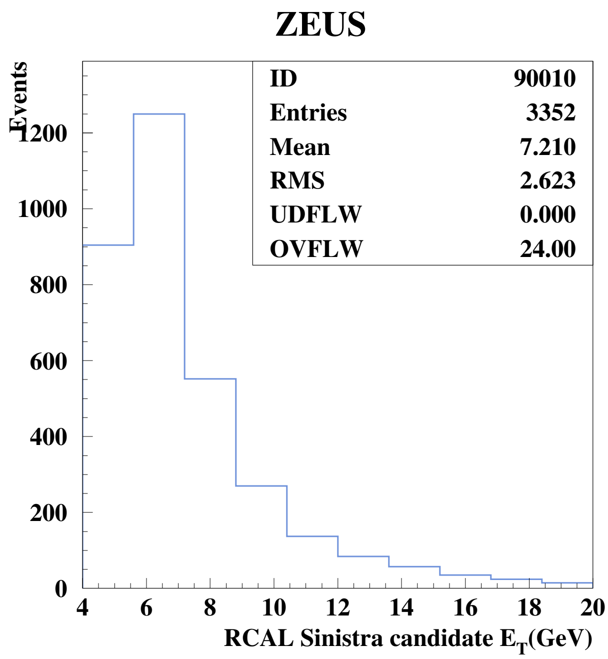

Figure 5.5: The transverse energy of electron candidates found by the Sinistra electron finder and located in the RCAL, indicating possible DIS electron candidates.

as a misidentified prompt photon.

The y_{JB} cut is applied offline, allowing for a correction to be applied based on Monte Carlo studies. Plots are created showing the 2-dimensional variation of the detector-level y_{JB} against the known hadron-level value for each bin in y_{JB}. The average value in each plot provides a point in a chart, to which a straight line is fitted, of equation

$$y_{JB}^{\mathrm{had}} = Ay_{JB}^{\mathrm{det}} + B$$

The values of A and B are extracted from the graph and provide a correction for the measured y_{JB} value, which then allows the data to be corrected.

The fit to the correction data is shown in figure 5.2. The extracted values of A and B for the y_{JB} fit are 1.07 and 0.03 respectively. Figure 5.3 shows the distribution of events in y_{JB} before the cuts are applied, but after the application of the correction.

To ensure a pure photoproduction sample, it was necessary to reject events which had the signature of a DIS event. The high-Q^2 of the transferred boson in a DIS event causes a greater momentum-transfer and hence causes a measurable deflection to the original lepton. This means that DIS events often have a high-energy scattered lepton generally located in the rear calorimeter.

The requirement which rejects DIS electron candidates was applied using the electron finder Sinistra, which allocates a probability of a given cluster being an electron. Clusters which had a greater than 90% probability of being an electron were found and tagged. If a Sinistra candidate with energy greater than 16 GeV was found in the RCAL the event was removed.

Figure 5.4 shows the distribution of E_T for lepton candidates tagged by Sinistra. Similarly, figure 5.5 gives the energy distribution of those lepton candidates which are located in the RCAL, where the DIS scattered lepton is most likely to be located.

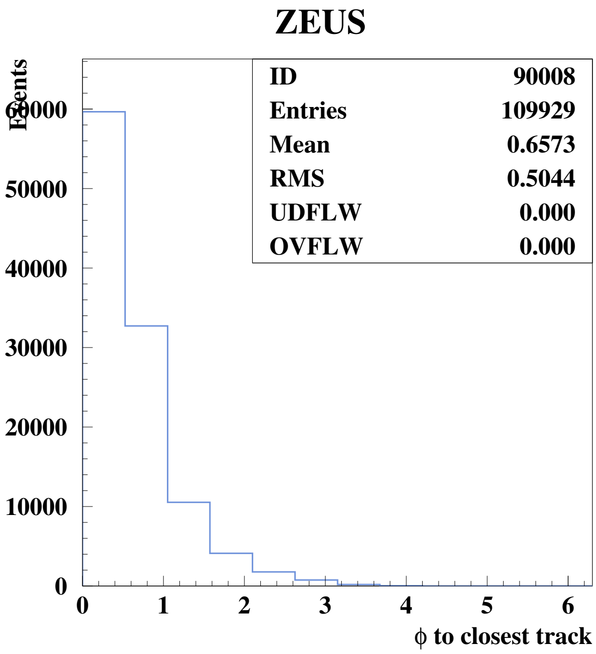

Figure 5.6: The distance in ϕ between the photon candidate and the nearest track in radians before applying the cut, which requires that the distance is greater than 0.3.

Prompt photon candidates may also discovered using the Sinistra electron finder. It is therefore important that these events are not rejected. To achieve this, only Sinistra candidates lying in the RCAL region and possessing an energy of more than 16 GeV were rejected.

The combination of these cuts ensures that there are no DIS events included in the photoproduction sample.

5.5 Photon finding

The signature of a photon in the ZEUS calorimeter is essentially the same as that of an electron. Therefore photon finding is initially performed with an electron-finder with no tracking requirement. The routine used looks for electromagnetic clusters in the ZEUS calorimeter with an energy > 4.5 GeV.

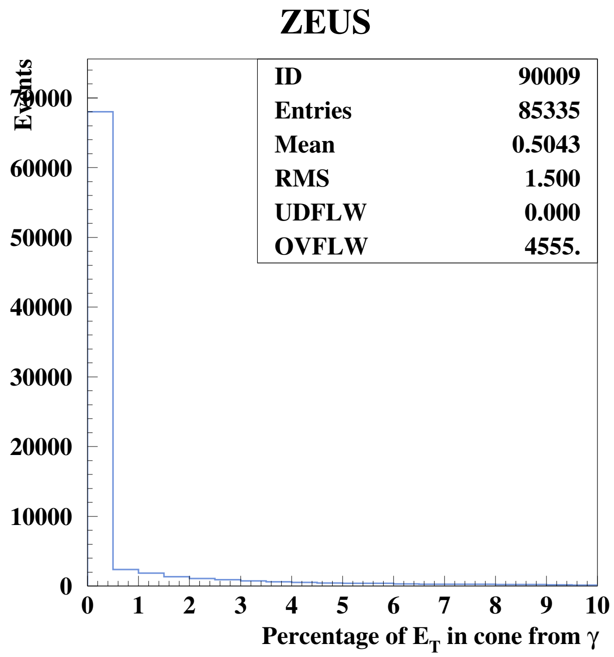

Figure 5.7: The percentage of the photon energy occupied by energy not from the photon in a unit cone around the cluster, before applying the cut. Note the large overflow.

It is then required that there is no track contained in the ZEUS CTD which lies within a cone in η-ϕ of 0.3 radians of the calorimeter deposit. This reduces the number of electrons and positrons identified by the electron finder to essentially zero. The ϕ to the closest track to the photon deposit before this cut is made is shown in figure 5.6.

To reduce the number of photons found which originate in jets of predominantly neutral particles, an energy-based isolation criterion is applied. The total energy in a unit cone around the photon candidate, excluding the photon, should be less than one tenth of the photon candidate energy. The percentage of energy that is found in the cone is displayed in figure 5.7.

The photon energy is corrected using the method described in section 5.6. After correction, the following requirements are made of the photon:

- $5 \leq E_T^{\gamma} \leq 15\,\text{GeV}$

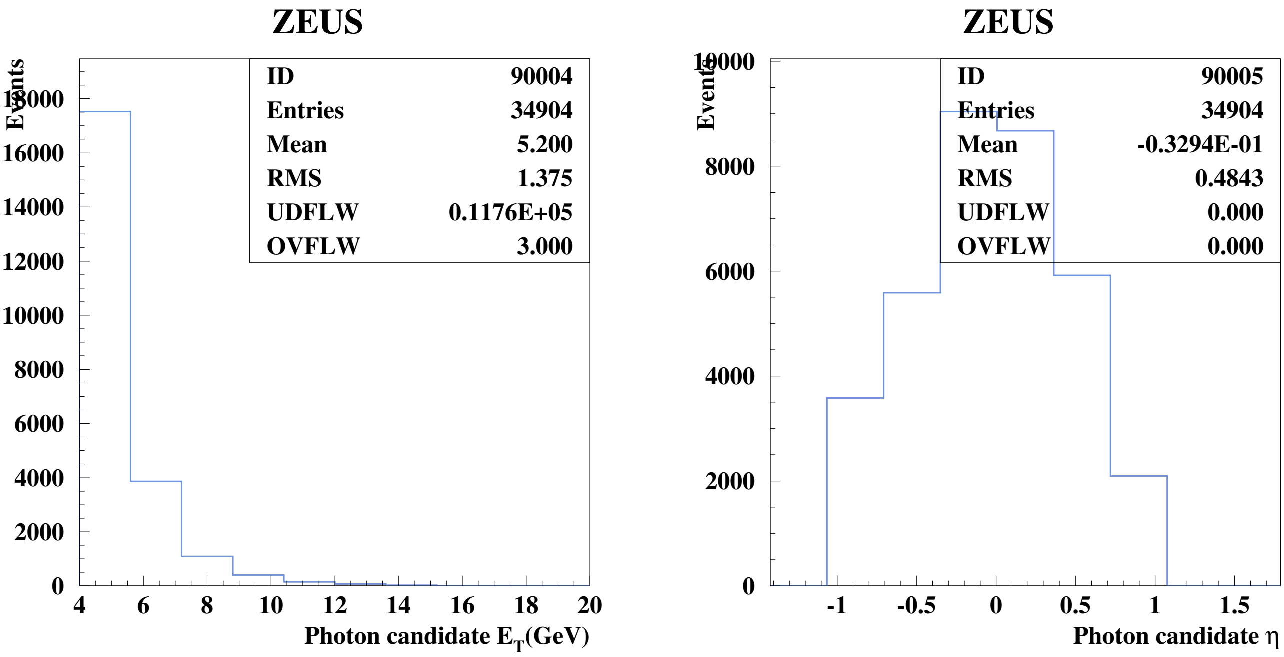

Figure 5.8: The photon E_T and η distributions with all cuts applied to the photon, but before the subtraction of neutral mesons, which are particularly influential at low-E_T^{γ}.

- -0.7 $\leq \eta^{\gamma} \leq$ 0.9

Photons which are not 'prompt', but rather originate from the decay of neutral mesons, remain in the sample at this stage, accounting for approximately 50% of the measured signal. They are removed by means of a shower-shape based subtraction process, which is described in detail in chapter 6.

Figure 5.8 shows the E_T and η of the photon candidates before the background subtraction takes place.

5.6 Photon energy correction

Monte Carlo comparisons between the parton- and detector-level photon display certain systematic shifts. Assuming that the detector is modelled accurately, the same shift can be assumed

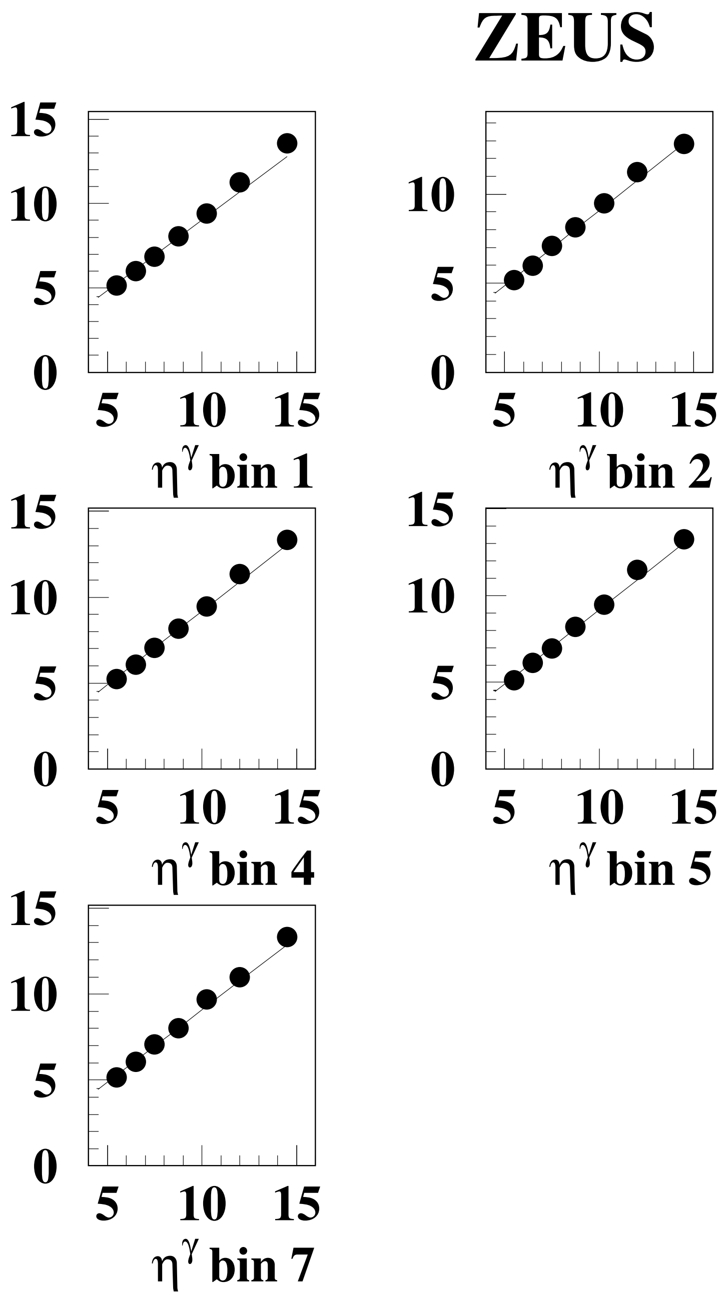

Figure 5.9: The photon E_T corrections in bins of η^γ. The straight lines provide the values of A and B for the correction. Both axes in each plot are in units of GeV.

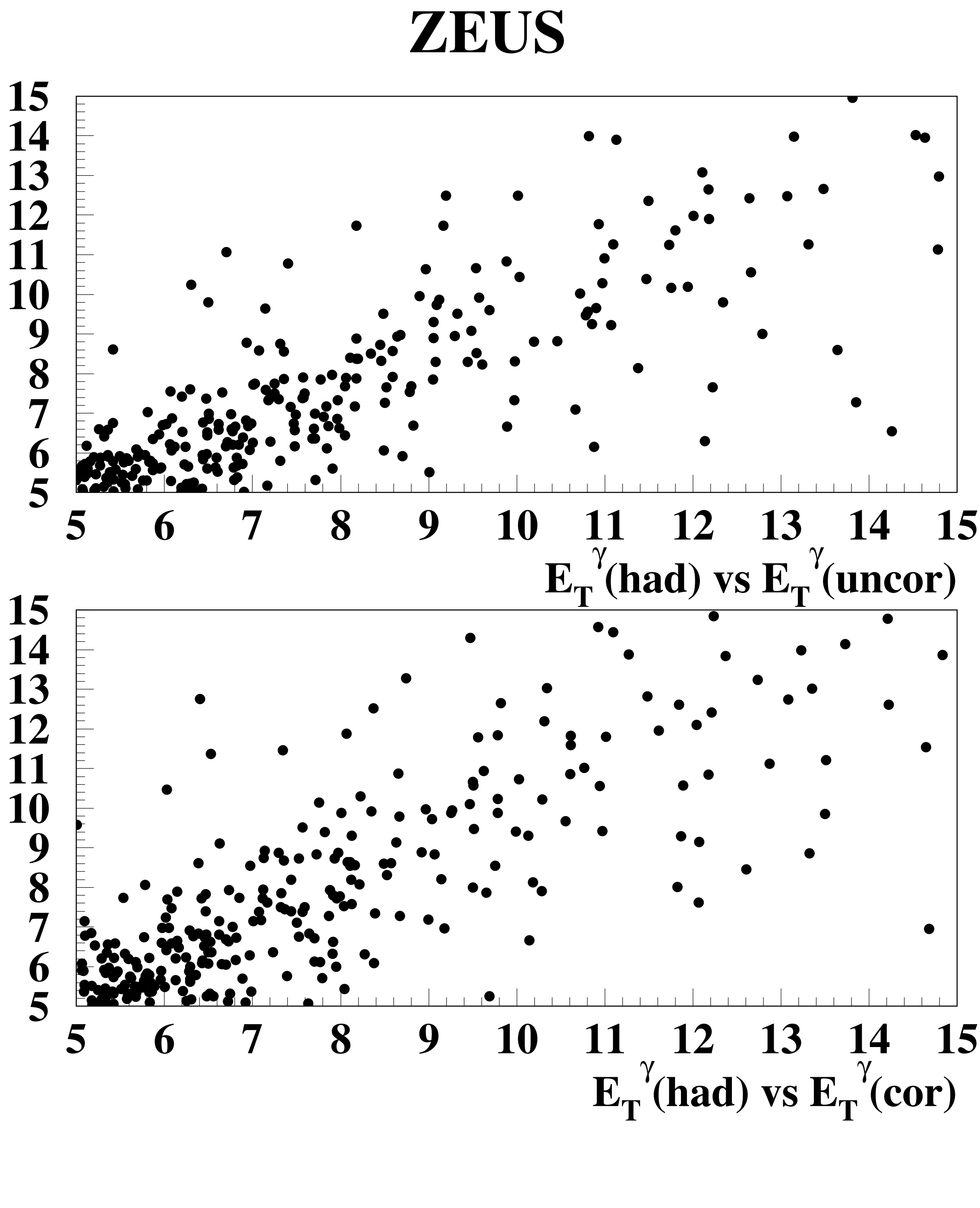

Figure 5.10: The correlation between the hadron and detector-level photon E_T before and after correction based on a PYTHIA Monte Carlo sample, as described in the text. The axes are in GeV.

η^γ **bin**	A	B
1	0.8363	0.6611
2	0.8426	0.6523
3	0.8656	0.5560
4	0.8574	0.6207
5	0.8595	0.5854
6	0.8585	0.5953
7	0.8409	0.6738
8	0.8566	0.5668

Table 5.1:

The fit parameters for the photon energy correction in bins of η^γ for the inclusive analysis.

to occur between the true energy and the detected energy in the data. Therefore the simulated events are used to generate a correction to the detected photon energy.

A comparison between hadron- and detector-level Monte Carlo reveals an η-dependence in the required energy correction. The corrections are therefore applied in bins of η. For each η-bin, a value of E_T^{det} is plotted against E_T^{had}. The resulting graph is a straight line with equation

$$E_T^{\mathrm{det}} = AE_T^{\mathrm{had}} + B$$

This provides values of A and B, and it therefore follows that

$$E_T^{\mathrm{cor}} = \frac{E_T^{\mathrm{det}} - B}{A}$$

The values found for A and B in bins of η are as shown in table 5.1 for the inclusive analysis and in table 5.2 for the jet analysis. The fitted straight lines in bins of η^γ are shown

η^γ **bin**	A	B
1	0.9377	0.0146
2	0.8638	0.6595
3	0.8699	0.7145
4	0.8639	0.7349
5	0.9315	0.1775
6	0.9028	0.3143
7	0.8843	0.5130
8	0.8607	0.6135

Table 5.2:

The fit parameters for the photon energy correction in bins of η^γ for the jet analysis.

in figure 5.9, while figure 5.10 displays the correlation between the hadron-level E_T^γ and the uncorrected detector-level E_T^γ from the Monte Carlo sample. Also shown is the comparison after the correction is applied.

5.7 Jet cuts

5.7.1 The K_T^{clus} jet finder

Jets are located with the K_T^{clus} [29] selection method. Previous prompt photon analyses at ZEUS have used a cone-based algorithm to define the jets, where a jet is made up of all particles which lie within a cone in $\eta - \phi$. However, these algorithms are not infra-red safe, and so if the particles in the jet emitted a large number of soft – that is, low E_T – particles, the number of jets found and their properties would be different. This is undesirable in a jet

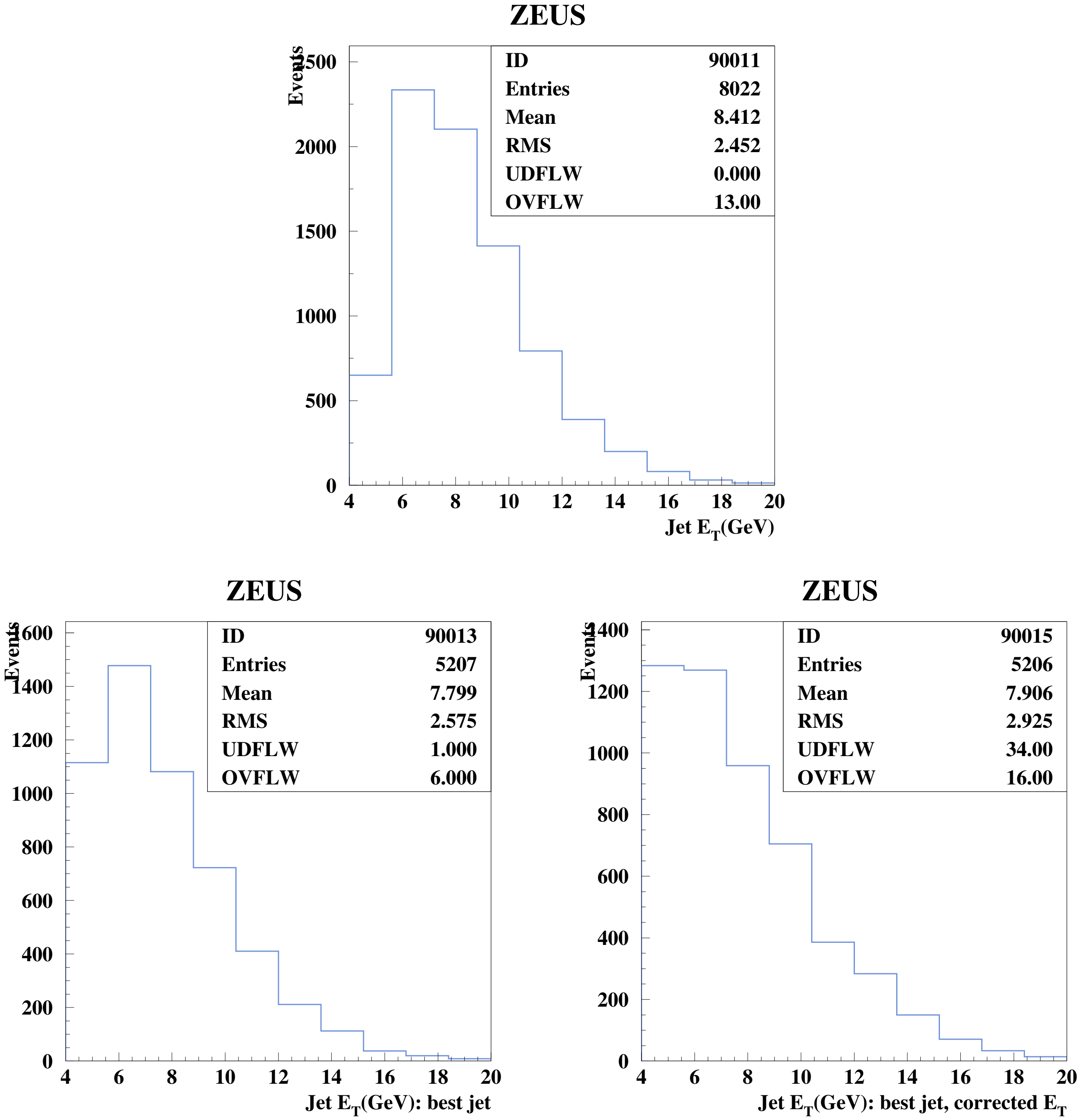

Figure 5.11: The top plot shows the distribution of $E_T^{\rm jet}$ before the best jet is selected, where only the energy of the first recorded jet is included. By comparison, the contribution from prompt photons misidentified as jets is clear, as is the effect of the minimum $E_T^{\rm jet}$ cut. Both the bottom plots have had the best jet, that is, the highest-E_T jet which is not matched to the photon, selected. The plot on the right hand side has had the energy correction applied.

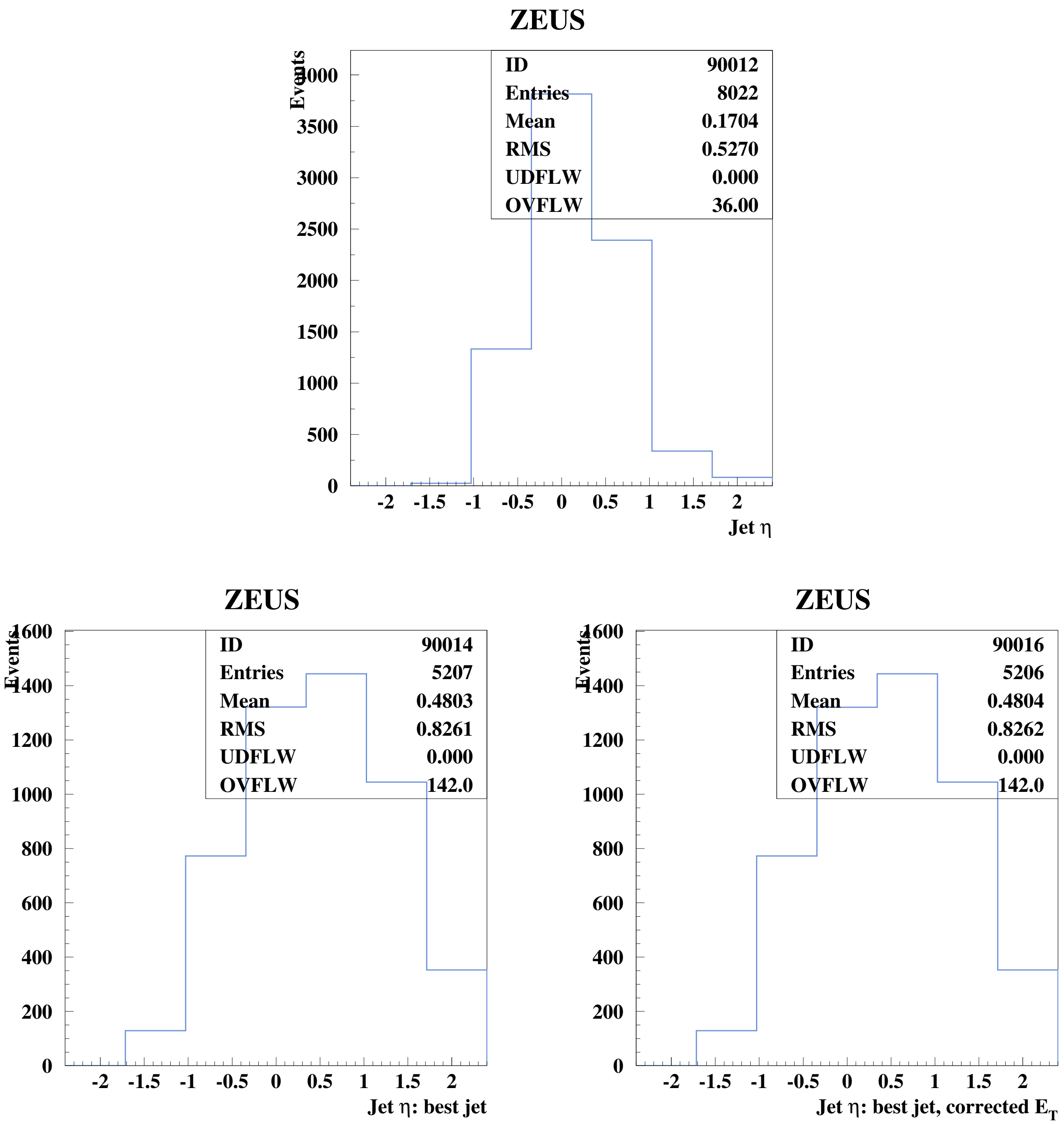

Figure 5.12: The top plot shows the $\eta^{\rm jet}$ PYTHIA distribution for the highest-E_T jet before any cuts are placed on it. The lower two plots show the distribution in η of the best jet, before and after the E_T correction is applied. As expected, the difference between the η before and after the energy is corrected is absolutely negligible.

finder.

By using a clustering mechanism which responds to the transverse momentum of the particles in the jet, the K_T^{clus} algorithm avoids this problem. As in the case of a cone-based algorithm, the jets are resolved based on their position in $\eta - \phi$. However, for the K_T^{clus} algorithm, the radius of the cone is variable and depends on the E_T of the particles in the jet. This means this algorithm is infra-red safe: if soft particles are radiated then they will be absorbed into the jet.

5.7.2 The jet cuts

Prompt photon events can be studied both in the inclusive form and also making a jet requirement. In the latter case, jets are required to pass the selection cuts $6 < E_T^{\text{jet}} < 17$ GeV and -1.5 $< \eta^{\text{jet}} <$ 1.8 after energy correction.

It is expected that there is a correlation in energy between the photon and the balancing jet. Since the lower E_T^{jet} cut is placed at 6 GeV rather than at the same level as the lower E_T^{γ} cut, it is likely that some prompt photon statistics are lost by this jet criterion. However, it is necessary for the NLO calculation that there is an asymmetry between the photon and jet energies. Previous prompt photon analyses at ZEUS placed the jet cut at 4.5 GeV, however the hadronisation corrections tend to be large at low E_T^{jet}, so the decision was made to use a slightly higher jet cut for this analysis.

The selection of the best jet is not necessarily straightforward. There may be low-E_T jets stored, and it is likely that the photon candidate will also be discovered by the jet finder. Therefore, to choose the best jet, any jet candidate which is within 0.5 radians of the photon candidate is removed from selection. The highest E_T jet is selected for study. Events with two jets which pass the low-E_T cut after correction are discarded for the γ plus jet selection.

Figure 5.11 shows three plots. The first shows the E_T^{jet} distribution which is found by selecting only the highest-E_T jet for study without first rejecting prompt photons found by the jet finder. In the lower two plots, the best jet has been selected. In the lower-right plot, the correction routine described in 5.8 is applied. Figure 5.12 contains the same plots in the pseudorapidity of the jet. The presence of the photon is particularly noticeable in the top plot in figure 5.12 by the dominance of events within the accepted photon pseudorapidity range. Once the selection of the best jet has been performed, this dominance is greatly reduced. In both figures, the subtraction of neutral mesons has not yet been applied, and therefore some changes in the shape of the distribution may occur due to this process.

5.8 Jet energy correction

In the case of quarks or gluons which are emitted from the final state, the particle cannot be observed directly. Instead, such particles undergo a process of *hadronisation*, in which the final-state quarks become hadrons, which, in turn, cluster into jets of particles. It is this jet that is observed in the detector.

This hadronisation process obscures the details of the original particle, which may have undergone subsequent decay, and hence it is difficult to deduce the precise details of the interaction which has taken place. Furthermore, Monte Carlo samples must be able to provide reasonable agreement with data as to the complicated process of hadronisation.

As in the photon case, the detector-level Monte Carlo jets display a similar shift from the parton level. In the case of hadronic jets, this is more severe than for photons, due to the additional hadronisation process which must also be accurately modelled. However, the same correction method as used for the photon is applicable here, despite the fact that the corrections are expected to be larger for the jet case.

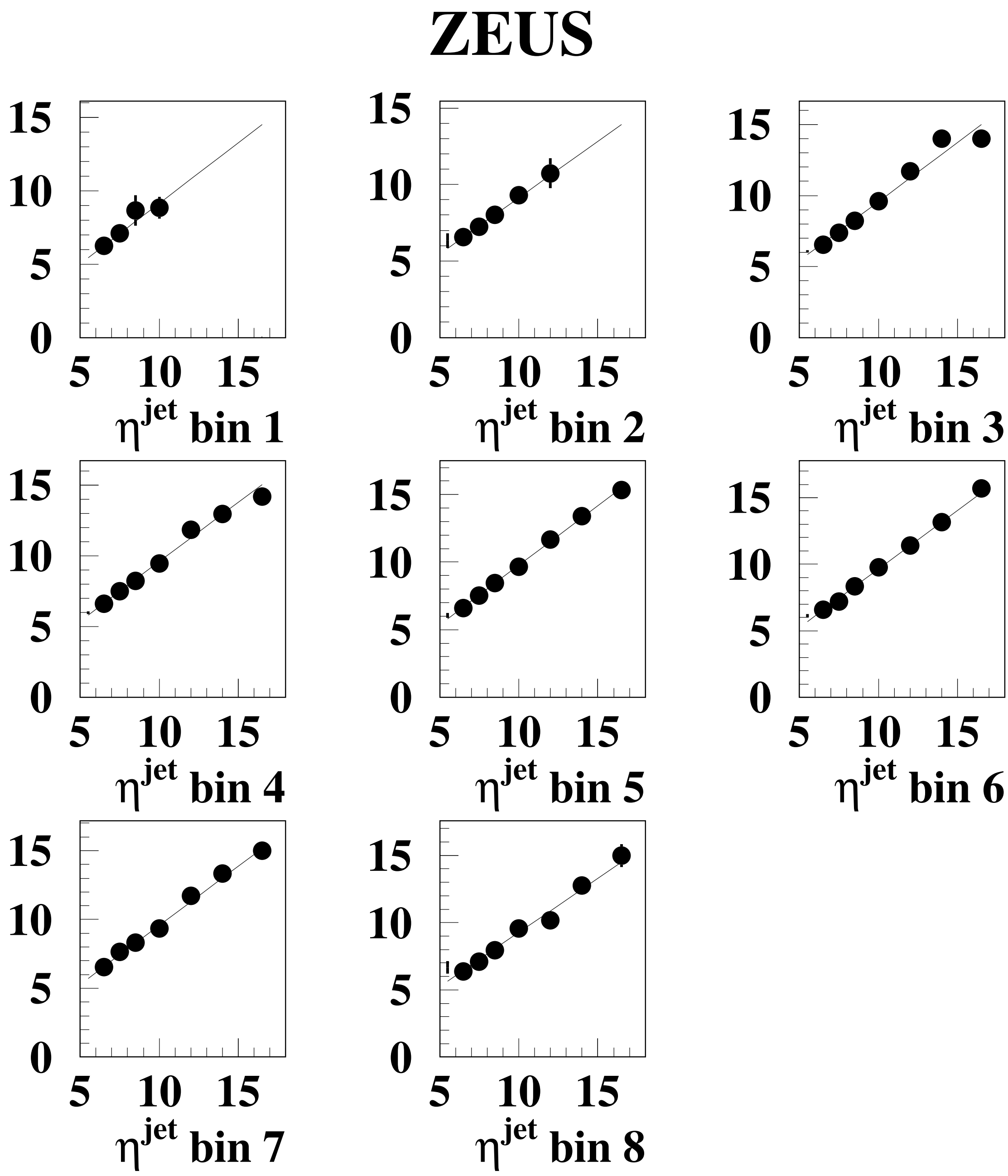

Figure 5.13: The jet E_T corrections in bins of $\eta^{\rm jet}$. The straight lines provide the values of A and B for the correction. Both axes in each plot are in units of GeV.

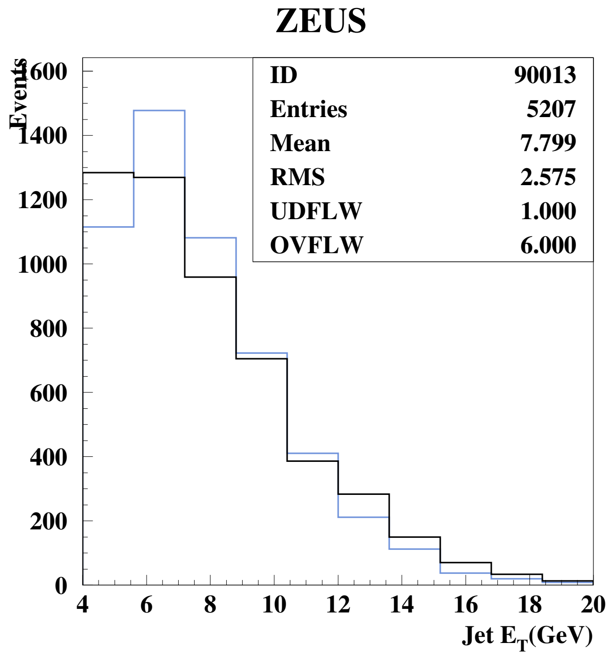

Figure 5.14: The difference between the corrected (black) and uncorrected jet E_T. The range of the plot is increased to allow for a more complete comparison of the effects of the correction.

$\eta^{\rm jet}$ **bin**	A	B
1	0.8250	0.8896
2	0.7352	1.7759
3	0.8329	1.2479
4	0.8386	1.2159
5	0.9315	0.1775
6	0.9028	0.3143
7	0.8843	0.5130
8	0.8607	0.6135

Table 5.3:

The fit parameters for the jet energy correction in bins of $\eta^{\rm jet}$.

In the case of the jet energy correction, the equation of the straight line is

$$E_T^{\mathrm{had}} = AE_T^{\mathrm{det}} + B$$

as the subtraction is a straightforward comparison between the hadron and detector level. The extracted values for A and B are given in table 5.3.

Figure 5.13 displays the fitted straight lines used to correct the jet E_T in bins of η^{jet}. The difference between the corrected and uncorrected jet E_T is shown in figure 5.14.

5.9 Summary of event selection

After the application of all cuts described except the jet cuts, a total of 34,847 events remain from the original 96-00 sample. Applying the jet cuts reduces this further to 5,169 events.

At this point, a photoproduction sample has been obtained containing a photon candidate in the BCAL. Jets are stored, and may be selected if the photon plus jet analysis is preferred. However, it is possible that some of these photon candidates originate from the decay of neutral mesons such as π^0, η or K_s^0 mesons. The removal of such background is described in detail in chapter 6.

5.10 Comparison between data and Monte Carlo for the inclusive analysis

In drawing comparisons between Monte Carlo samples and the data, it is necessary to first subtract the background from neutral mesons using the process described in chapter 6. The resulting comparison is presented here.

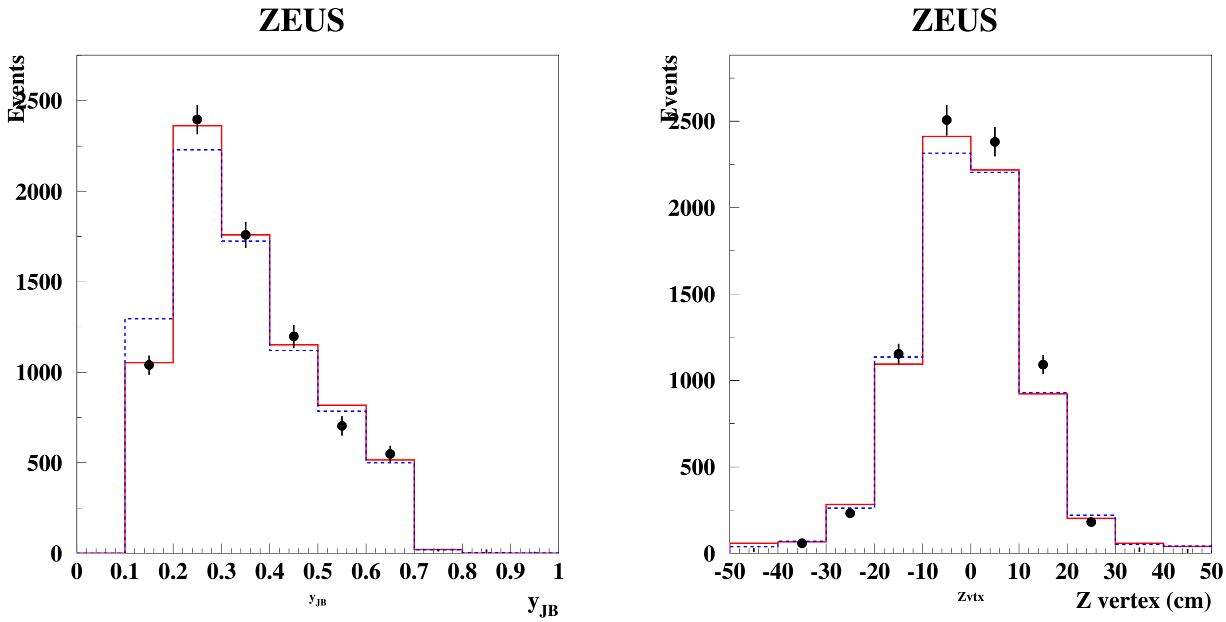

Figure 5.15: The left plot shows the y_{JB} distribution of the data compared to PYTHIA (full, red line) and HERWIG (blue, dashed) Monte Carlo simulations, and the right plot shows the same for the $Z_{\rm vtx}$ distribution. These distributions are from the inclusive photon process.

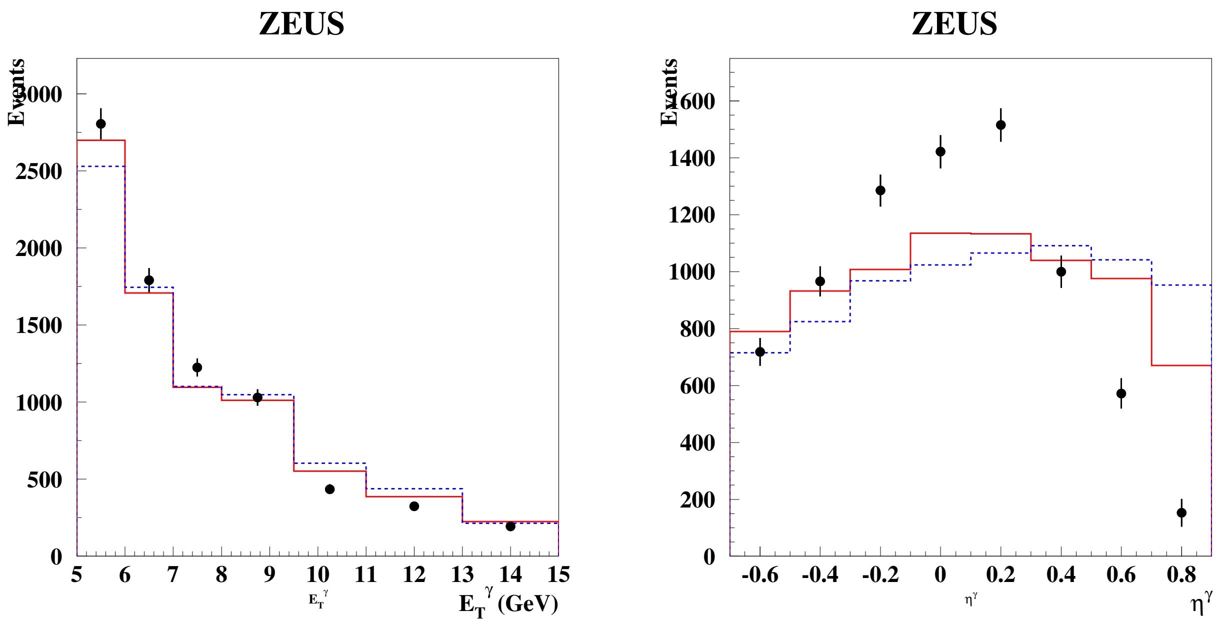

Figure 5.16: The left plot shows the E_T^γ distribution of the data compared to PYTHIA (full, red line) and HERWIG (blue, dashed) Monte Carlo simulations. Similarly, the right plot shows the same for the η^γ distribution. Both distributions are here displayed for the inclusive process.

Figure 5.15 shows the y_{JB} and Z_{vtx} distributions for the inclusive prompt photon process, as compared to the PYTHIA and HERWIG simulations. Both Monte Carlo programs provide a good description of the two variables, showing that both PYTHIA and HERWIG give a good approximation to the dynamics of a photoproduction event.

Figure 5.16 shows a comparison between the PYTHIA and HERWIG descriptions of the photon variables, the E_T and η of the photon, and the observed data after subtraction of the neutral meson background. Both PYTHIA and HERWIG give a good approximate description to the data for the E_T^{γ} distribution, particularly for energies above 6 GeV. In the η^{γ} distribution, there is a definite depletion in the central region and a surplus in the forward region for the Monte Carlo with respect to the observed data.

5.11 Comparison between data and Monte Carlo for the jet analysis

The comparisons between the data after the application of all cuts and the subtraction of the neutral meson background and the two Monte Carlo simulations are shown in figure 5.17. There is little difference in the quality of agreement between the PYTHIA and HERWIG samples for the control variables.

Figure 5.18 shows the description of the photon and jet E_T and η by the two Monte Carlo programs. It is clear that the PYTHIA programme provides a better description of the data compared to HERWIG. This is true for all four variables, but is most noticeable in the description of the photon pseudorapidity.

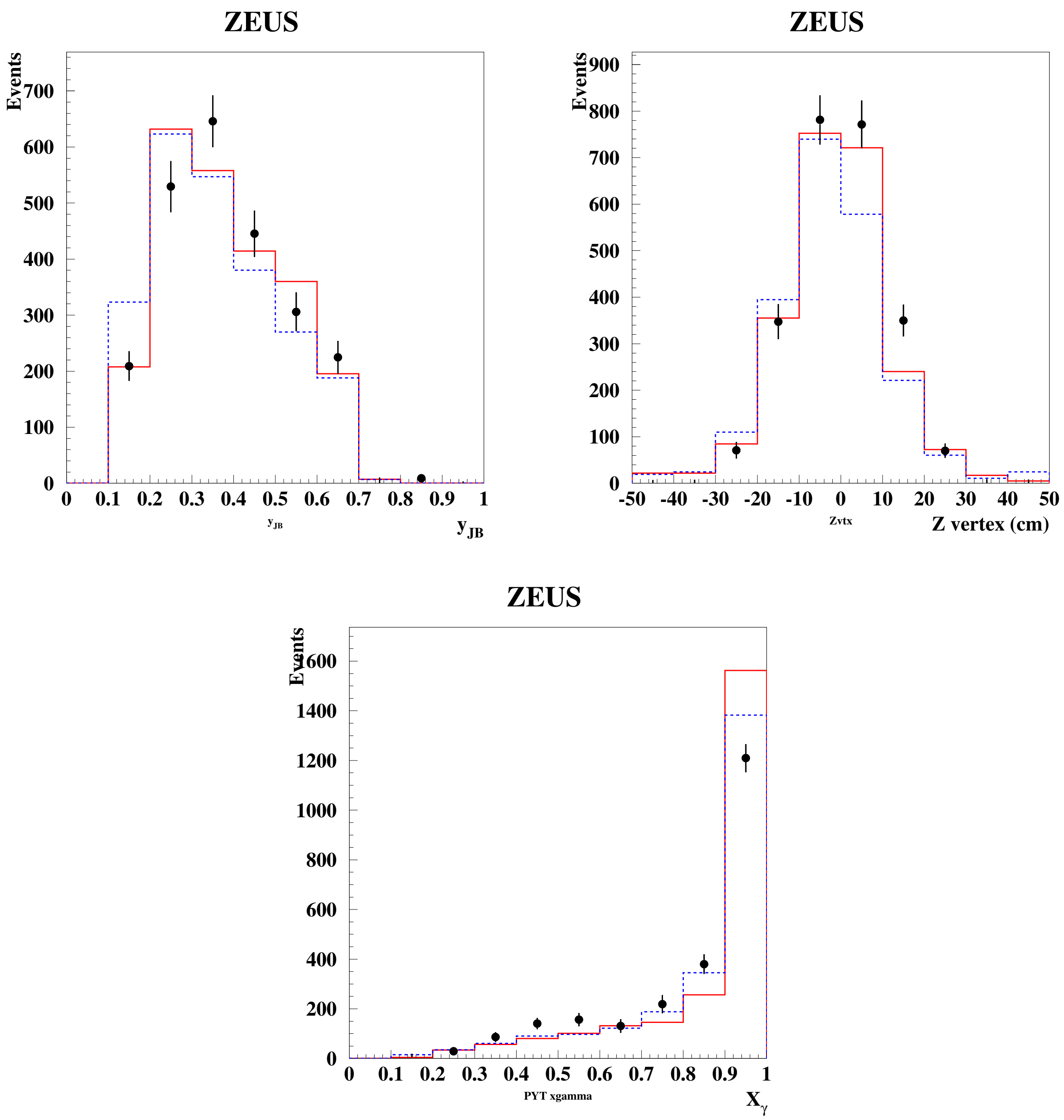

Figure 5.17: The top left plot shows the y_{JB} distribution of the data compared to PYTHIA (full, red line) and HERWIG (blue, dashed) Monte Carlo simulations. The top right plot shows the same for the $Z_{\rm vtx}$ distribution, while the bottom plot shows the x_γ distribution. These distributions are from the photon plus jet process.

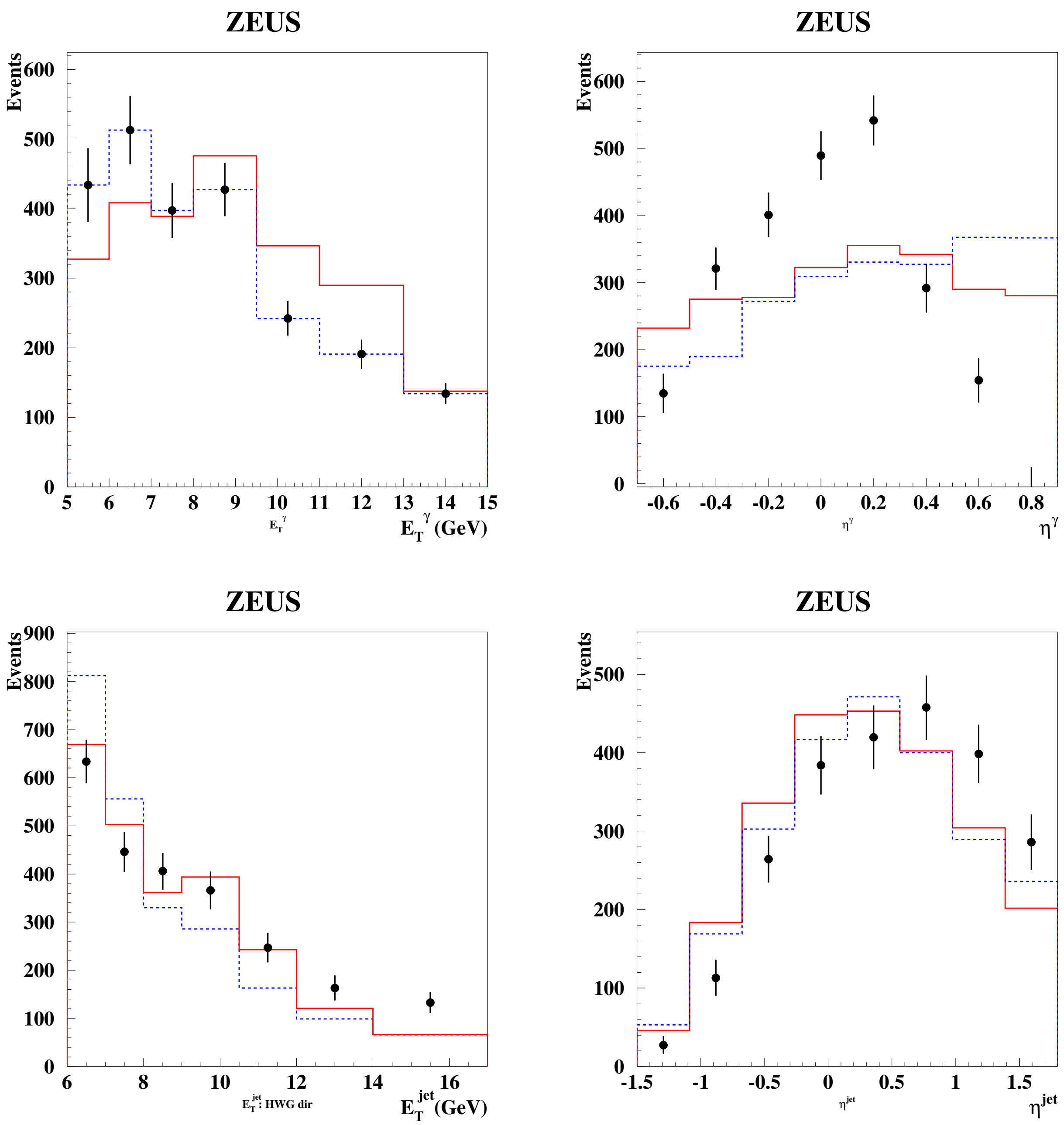

Figure 5.18: The top left plot shows the E_T^γ distribution of the data compared to PYTHIA (full, red line) and HERWIG (blue, dashed) Monte Carlo simulations. Similarly, the top right plot shows the same for the η^γ distribution. On the bottom are the jet variables, with the E_T of the jet show on the left and the pseudorapidity on the right. All variables are for the photon plus jet process.

5.12 The dijet method

The 'dijet' method, briefly described in section 1.4, is a proposed new method to study prompt photons. This method attempts to extend the analysis beyond the limits of the current method. One of the features of the method is that it is limited to the photon plus one or more jets case. The method is described in detail in the following sections.

The philosophy of the dijet method is as follows. Instead of finding the photon using an electron finder, dijet events are found, that is, events with a two-jet signature, with both jets passing a certain low-E_T cut. It is then required that one of the jets is made up of 95% electromagnetic energy. This electromagnetic jet is the photon candidate.

In this method, the removal of neutral mesons relies on the BPRE (described in section 3.6.2). This method essentially relies on the probability that a photon be converted to an e^+e^- pair. Signals from neutral mesons are made up of multiple photons and have a proportionally higher probability of conversion.

5.12.1 The cuts used in the dijet method

The cuts used in the dijet analysis are described below.

First, a preliminary event selection is made using orange (ZEUS code described in subsection 5.1.2):

- Events were selected from HERA 99-00 running, during which the BPRE was available.
- The trigger selection DST bit 79 was selected (described in section 5.2)
- The total missing p_T should be less than 10 GeV.
- The Z_{vtx} of the event should satisfy $|Z_{\text{vtx}}| < 55$cm.

- The uncorrected y_{JB} should be between 0.15 and 0.9.
- There should be no electron candidate identified by the Sinistra or EM electron finders.
- Two or more jets should be reconstructed by the $K_T^{\rm clus}$ algorithm, both satisfying $E_T^{\rm jet} >$ 4 GeV and $-2.6 < \eta^{\rm jet} < 2.6$.
- Of the two jets, one jet should be predominantly electromagnetic, and should satisfy $\frac{E_{\rm EMC}}{E_{\rm TOT}} > 0.85$; that is, the ratio of energy found in the electromagnetic calorimeter to the total energy of the jet should be more than 85 %. This jet should also have no matched track.

Corrections are applied to the $y_{\rm JB}$ distribution and the E_T of the 'photon jet' and the jet in much the same way as described in chapter 5.

After the corrections have been applied, more detailed selections are made:

- Corrected $y_{\rm JB}$ should lie in the region $0.2 < y_{\rm JB} < 0.8$.
- The ratio $\frac{E_{\rm EMC}}{E_{\rm TOT}}$ is tightened to be greater than 0.9.
- The 'photon jet' should satisfy $E_T^{\rm jet1} > 5\,{\rm GeV}$ and $-0.74 < \eta^{\rm jet1} < 1.1$, where the pseudorapidity requirement ensures that it lies within the acceptance of the BPRE.
- The second jet should satisfy $\frac{E_{\rm EMC}}{E_{\rm TOT}} < 0.9$, and should fall in the region $E_T^{\rm jet2} > 6\,{\rm GeV}$ (after correction) and $-1.6 < \eta^{\rm jet2} < 2.4$.

The background is reduced by the following selection:

- The MIP signal from the BPRE should be less than 4, where 4 represents 4 electromagnetic particles being detected in the BPRE.

For a fair comparison, it is necessary to use identical cuts where possible. Therefore for the purposes of the comparison, the cuts used in the shower shape analysis were modified to match those in the dijet method and the analysis was restricted to 99-00 data only. The results of the comparison are presented in section 8.4.

Chapter 6

Background subtraction and the DVCS process

6.1 Introduction

The cuts described in chapter 5 provide a sample of prompt photon candidates. However, there exists within this sample a selection of events which are generated by neutral mesons. These may decay to photons, hence producing a false signal in the detector. These are removed by a detailed subtraction process based on the shower shapes.

Studies which have been performed to optimise the background subtraction are further described here.

6.2 Neutral meson signals

The major background to the sample of prompt photon candidates comes from neutral mesons. These originate within jets and can have a large p_T, thus when they decay to photons according to the branching ratios below, the signal can be misidentified as a prompt photon. The contribution by these events is reduced by the no-track requirement, which is purposefully broad to mask signals from electrons or from nearby charged particles. It is further reduced by the isolation cut, which ensures that the photon candidate contains most of the energy originating in that region and is therefore unlikely to originate in a jet.

The main components to the background arise from the processes:

$$\pi^0 \rightarrow \gamma\gamma \text{ Branching ratio } 98.8\%$$

$$\eta \rightarrow \gamma\gamma \text{ Branching ratio } 39\%$$

$$\eta \rightarrow \pi^0\pi^0\pi^0 \text{ Branching ratio } 32\%$$

where in the third process each π^0 decays to two photons, causing a six-photon final state.

The contribution to the prompt photon sample can be reduced by making use of the multiple-photon nature of these processes. A true prompt photon process will contain only one photon and will therefore produce a very narrow signal in the calorimeter. However, the final state photons can only be individually resolved when they are separated by a distance which is greater than that of one calorimeter cell, and even in that case, the same signal would be generated by a single photon which loses a fraction of its energy over two or more calorimeter cells.

It is therefore helpful to consider the separation of the photons generated by the decay of a π^0. The opening angle, α, between two photons produced, for example, from the decay of a π^0 where the two photons have energies E_1 and $E_{\pi^0} - E_1$ can be calculated as follows:

$$\alpha = 2\sin^{-1}\left(\frac{m_{\pi^0}}{2\sqrt{E_1(E_{\pi^0} - E_1)}}\right)$$

This is minimised, that is, the resultant photons are closest together, when the energies of the two photons are equal. In this case, the minimum distance observed in the calorimeter,

D_{min}, can be deduced from the geometry as:

$$D_{min} = 2 * \frac{123.2}{\sin\theta_{\pi^0}} \tan\left(\sin^{-1}\frac{m_{\pi^0}\sin\theta_{\pi^0}}{E_{T,\pi^0}}\right)$$

These equations are also applicable to the photons produced by a decaying η meson, where θ_{π^0}, m_{π^0} and E_{T,π^0} should be replaced by the angle, mass and transverse energy, respectively, of the outgoing η meson. The number 123.2 is the distance from the interaction point to the detection point, that is, the radial distance from the beampipe to the BCAL.

For an outgoing π^0 with energy in the range 5-10 GeV, the minimum separation, D_{min} is calculated to be 6.7-3.3 cm, while the wider shapes from the decay of an η meson in the same range give a D_{min} of 27.2-13.5 cm. This information can be used to distinguish between particles. This cannot be done on an event-by-event basis, since it can occur that the full energy from the decay of a π^0 lies within a single calorimeter cell. The subtraction is therefore performed statistically.

6.3 Shower shapes background subtraction

In order to perform the background subtraction, two variables are defined which represent the shape of the electromagnetic cluster in the BCAL. The first, f_{max}, is a measure of the proportion of the total energy in an electromagnetic cluster found in the most energetic cell. A prompt photon is expected to have an f_{max} near 1, although it can be as low as 0.5 in the case where half of the photon energy is deposited in each of two adjoining calorimeter cells. That is,

$$f_{max} = \frac{\text{Energy in most energetic cell}}{\text{Total energy in cluster}}$$

The second variable, $\langle\delta Z\rangle$, is a measure of the average energy-weighted spread of the cluster in z. Prompt photons give a narrow signal in z, and thus will peak at low values of $\langle\delta Z\rangle$,

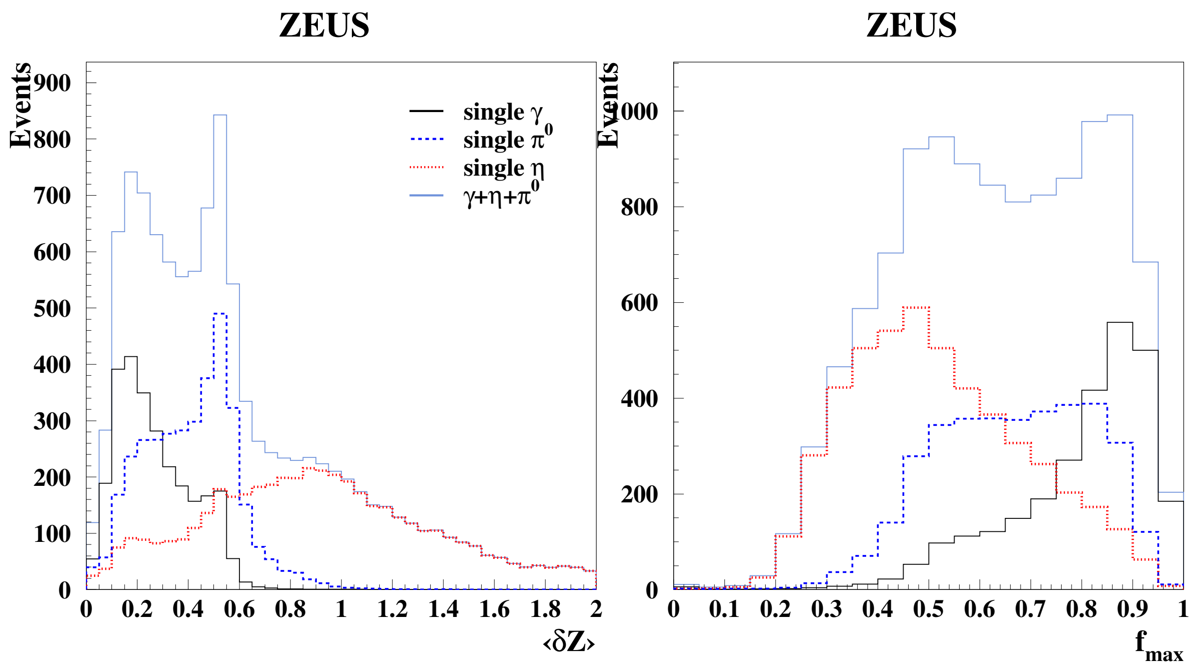

Figure 6.1: The $\langle \delta Z \rangle$ and $f_{\rm max}$ plots showing the single particle Monte Carlo distributions. The η, π^0 and γ distributions are weighted in E_T to match the data, and then fitted to the data. The pale blue line shows the sum of the Monte Carlo contributions.

while the signal from neutral mesons will be larger. The distribution in z due to η mesons is particularly large, and these give a long tail to the $\langle \delta Z \rangle$ distribution. The definition of $\langle \delta Z \rangle$ is

$$\langle \delta Z \rangle = \frac{\sum (E_{cell} |z_{cell} - \bar{z}|)}{\sum E_{cell}}$$

where the sum is over the cells in the cluster.

The distributions for f_{max} and $\langle \delta Z \rangle$ are displayed in figure 6.1. This uses single-particle Monte Carlo, which is generated with a flat E_T spectrum and then weighted in E_T^{γ} to match the data.

The fit to the data is displayed in figure 6.2.

The shower shape subtraction is performed as follows. In the $f_{\rm max}$ plot, a cut is placed such that $\langle \delta Z \rangle > 0.65$. Further background subtraction uses the f_{max} distribution. Events that have $f_{max} > 0.75$ are considered to be 'good' events, while those with $f_{max} < 0.75$ are called 'poor' events, where background is expected to dominate in poor events.

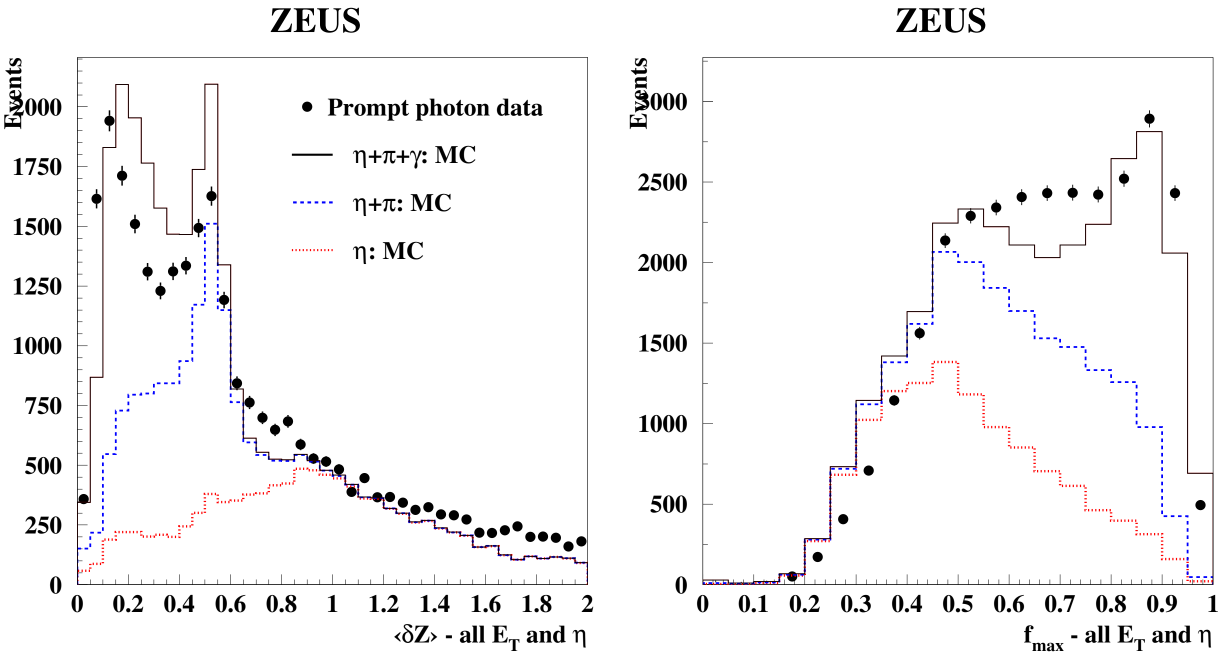

Figure 6.2: The $\langle\delta Z\rangle$ and $f_{\max}$ plots showing the fit to prompt photon in photoproduction data. The data are fitted to the $\eta + \pi^0 + \gamma$ distributions from single particle Monte Carlo. The two fits are performed simultaneously, and the cut $\langle\delta Z\rangle < 0.65$ is applied only in the $f_{\max}$ distribution.

Let n_+ be the number of good events, and n_- be the number of poor events. Then for some α, β:

$$n_+ = \alpha S + \beta B$$

$$n_- = (1-\alpha)S + (1-\beta)B$$

where S is the number of signal events and B is the number of background hits. n_+ and n_- can be obtained from the data $f_{\max}$ distribution. Solving the above equations gives:

$$S = \frac{(1-\beta)n_+ - \beta n_-}{\alpha(1-\beta) - \beta(1-\alpha)} \tag{6.1}$$

and

$$B = \frac{1}{\beta}(n_+ - \alpha S) \tag{6.2}$$

The subtraction is therefore dependent only on β, while α enters only in the denominator, setting a scale factor.

This subtraction is performed on a bin-by-bin basis in E_T and η, and the 'signal' produced is then used to provide the cross section.

The statistical error on the signal and background can be calculated in a similar manner. We find that

$$\delta S = \sqrt{\frac{1}{(\alpha-\beta)^2}(n_+(1-\beta)^2 + n_-\beta^2)} \tag{6.3}$$

and

$$\delta B = \sqrt{\frac{1}{(\alpha-\beta)^2}(n_+(1-\alpha)^2 + n_-\alpha^2)} \tag{6.4}$$

6.4 f_{max} correction factors

The simulation of neutral mesons is not perfect. While generation of single particles with a flat E_T spectrum and re-weighting to match the prompt photon data provides an improved fit to the data, particularly at high-E_T, there remains a rapidity-dependent discrepancy between the peaks observed in the prompt-photon data and those seen in the Monte Carlo.

Detailed studies were carried out by Sung Won Lee for the previous prompt photon in photoproduction analysis. Samples of DIS positrons, prompt photon data and Monte Carlo simulations, neutral mesons from ρ-enriched Monte Carlo samples and $\eta + \pi^0$ anti-isolation background from neutral current events were obtained and examined. Comparing the data to these samples allowed rapidity-dependent correction factors in the range 0.95-1.05 to be determined. A χ^2-minimisation was then used to determine the optimum correction factors for the simulated single-particle backgrounds. Further details of the studies can be found in [30].

This study was not repeated for the present analysis, but the resulting correction factors were applied as follows.

- Single γ: $f^{\mathrm{cor}}_{\mathrm{max}} = (-0.104\eta_\gamma^2 + 0.002\eta_\gamma + 1.046) * f_{\mathrm{max}}$

- Single π^0 and η: $f_{\rm max}^{\rm cor} = f_{\rm max} + \frac{1.8(-0.047\eta_\gamma^2+1.01-1)}{f_{\rm max}-0.4}$

In the case of the DVCS photons, no correction factor was deemed necessary.

6.5 The DVCS process and event selection

DVCS stands for Deeply Virtual Compton Scattering. The process is a *diffractive* one, that is, the proton is not broken up in the event, and has a final state made up of only an electron (or positron) and a photon. The lack of hadronic activity ensures no contribution from neutral mesons, and allows the DVCS process to provide a pure sample of photons uncorrupted by the decay of neutral mesons.

As can be seen from figure 6.2, the fit to the data provided by the simulated photons is poor, particularly at very low values of $\langle \delta Z \rangle$. While the subtraction process should ensure that the effect of this poor fit is minimised, this should be checked. DVCS photons provide a pure sample of photons which can be used as a cross check, both for the subtraction method and for the effect of the poor fit on the extracted signal.

This cross-check was originally performed for the prompt photon in DIS analysis. In the photoproduction analysis, the DVCS process was used as the preferred sample of pure photons, and the single particle photons were used as a cross-check. The sample of DVCS photons was provided by the authors of the recent ZEUS publication [31] and the relevant details about the sample follow.

The DVCS process is $ep \to e\gamma p$. At $Q^2 > 5\,{\rm GeV}^2$ the event signature consists of a photon and an electron at balanced transverse momenta. The proton is not scattered through a large angle and remains undetected in the beampipe.

Two electromagnetic clusters were required. One was constrained to occur in the RCAL and have energy $E_1 > 15\,\mathrm{GeV}$. This was the DIS scattered electron. The second could occur in either the RCAL or the BCAL, and should have energy $E_2 > 2.5\,\mathrm{GeV}$ and polar angle $\theta_2 < 2.75$ rad. Any track found in the CTD was required to point to one of the electromagnetic clusters. Any further activity in the calorimeter, not associated with these clusters and not consistent with noise, was required to have energy less than 0.2(0.3) GeV for the 96-97 (98-00) running period. A further cut of $40 < W < 140\,\mathrm{GeV}$ was applied, where W is as defined in equation 2.2.

At this stage, no assumption is made that the second electromagnetic cluster points to a photon, and in fact there were events in the sample containing two electrons or an electron and a positron. These events were removed at a later stage.

The above cuts are those used to produce the required event list. Those events, as provided by the diffractive group, were then passed through the event selection for the prompt photon analysis with the photoproduction and the DVCS-reduction cuts removed.

In order to clean up this sample further, to be as sure as possible that the photons are comparable, the following cuts were applied:

- There should be no charged track pointing to the cluster - this removes the electron contribution.
- The energy in a cone around the cluster not from the photon should be 0.
- The energy in the BEMC should be more than 2 GeV.
- The transverse momentum, p_T, should be > 5 GeV.

6.6 Shower shapes in DVCS

The DVCS events provide a sample of pure photons. Figure 6.3 shows the difference between the shower shape distributions for single photon Monte Carlo and DVCS data. The plots are broadly the same shape, although it can be seen that both plots have a much narrower peak in the DVCS data than in the Monte Carlo.

Figure 6.4 shows the same distributions, this time weighted to match the prompt photon in photoproduction data.

6.6.1 Weighting the DVCS

Figure 6.5 shows a comparison of the E_T and η distributions of the photons from the prompt photon in DIS analysis and the DVCS photons. The variation in η is minor, but there is a noticeable difference in the E_T distributions.

The DVCS photons were therefore weighted in energy so that their energy matched those of the data. This allowed much more accurate f_{max} and $\langle \delta Z \rangle$ plots to be produced, which had the same energy dependence as the data.

Figure 6.6 shows a similar plot for the photoproduction analysis. For this analysis, the E_T^{γ} distribution showed less of a discrepancy with the prompt photon distribution than the η distribution. It was therefore decided to weight the DVCS data in pseudorapidity rather than transverse energy.

Figure 6.7 shows the shower shape distributions fitted to the DIS prompt photon data, where the fit is performed to the sum of energy-weighted DVCS photons with single π^0 and η mesons. The resulting fit is much improved compared to that performed with single photon Monte Carlo.

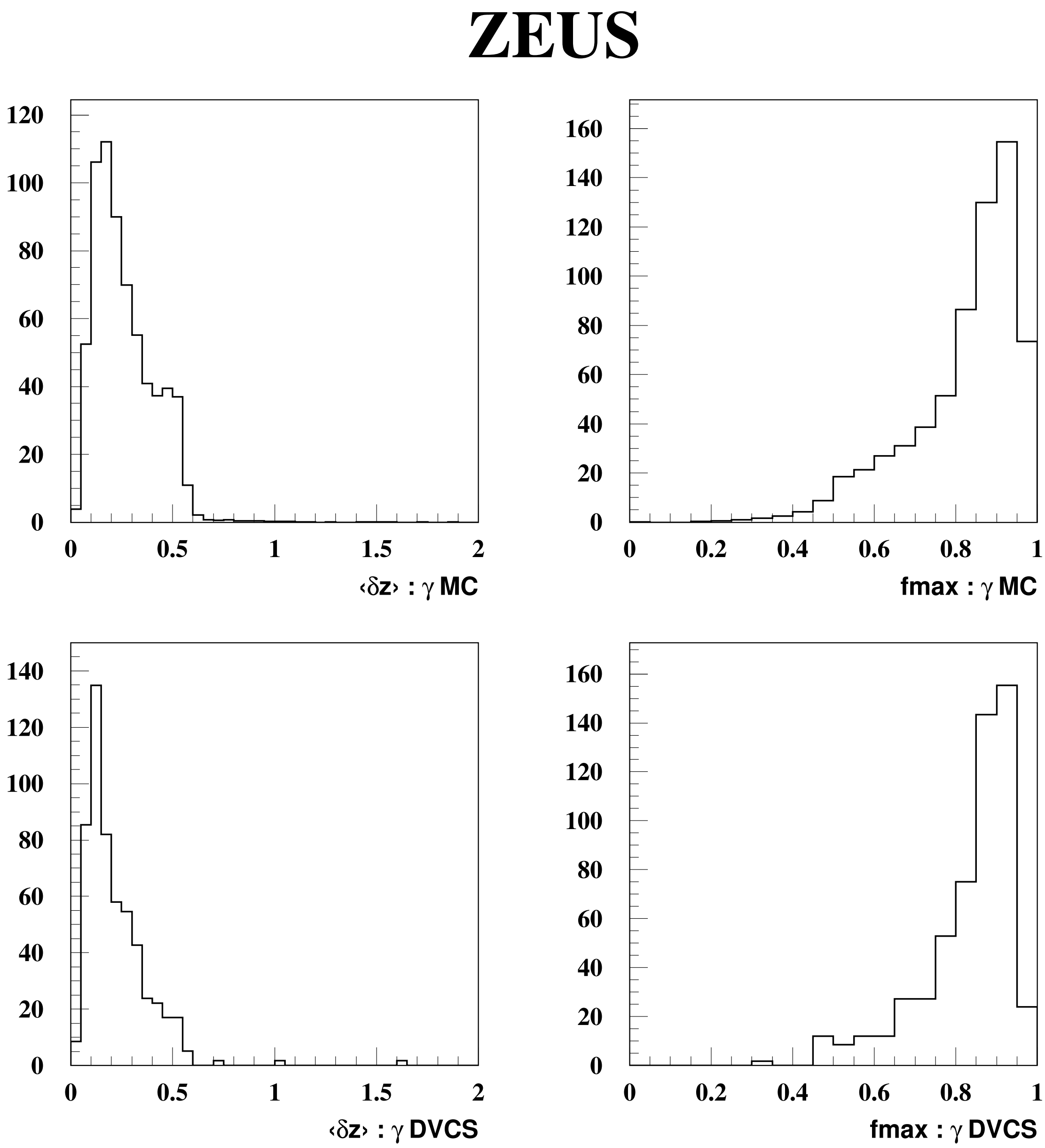

Figure 6.3: The shower shape distributions. On the left is $\langle \delta Z \rangle$ and on the right is f_{max}, the top two plots being the single photon Monte Carlo, while the lower two are DVCS data. The plots are broadly the same shape, although it can be seen that both plots have a much narrower peak in the DVCS data than in the Monte Carlo. The plots have been normalised to the prompt photon in DIS data.

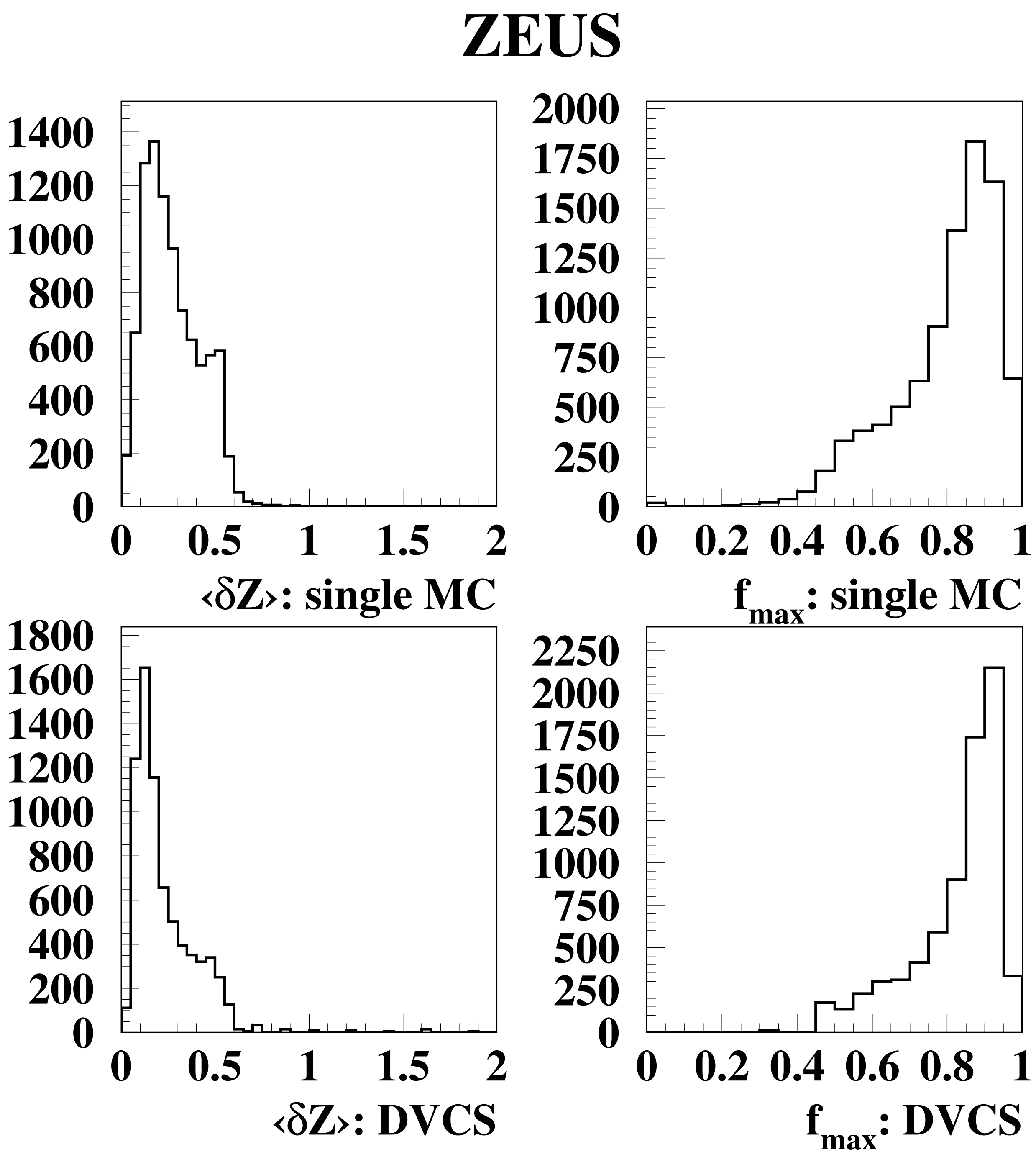

Figure 6.4: The same plots as in figure 6.3, this time weighted to the photoproduction data.

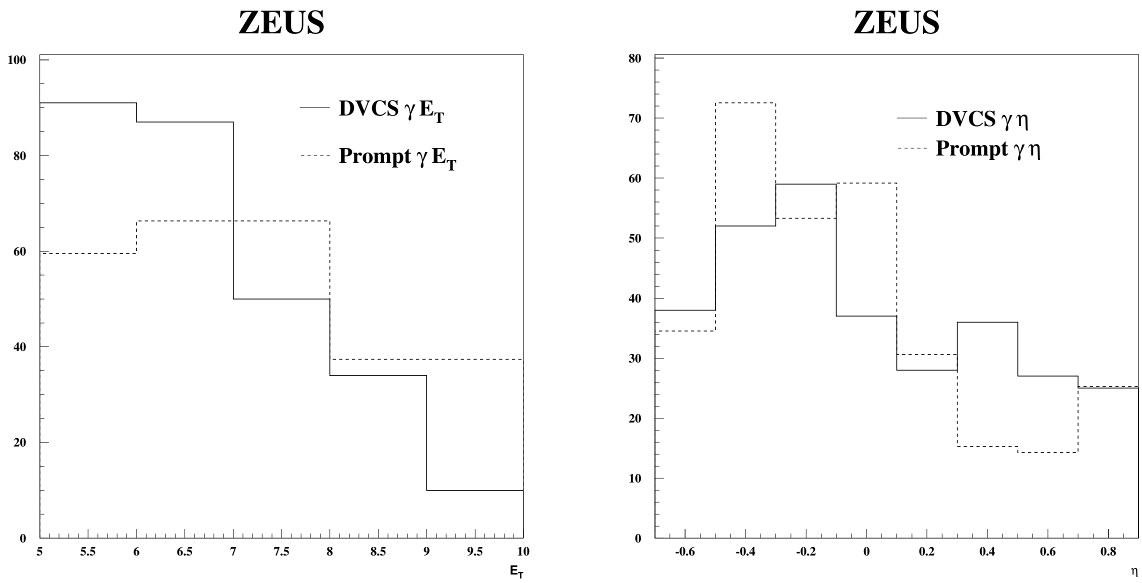

Figure 6.5: A comparison of the transverse energy and the pseudorapidity of the DVCS photons and the prompt photons from the DIS analysis. The plots have been normalised to the same number of events.

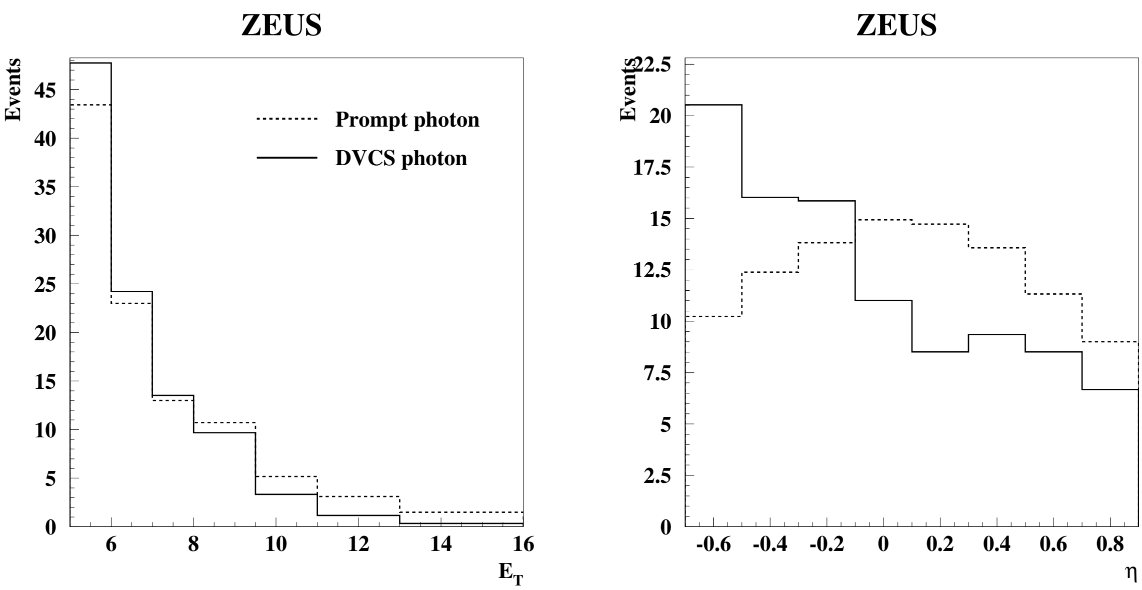

Figure 6.6: A comparison of the transverse energy and the pseudorapidity of the DVCS photons and the prompt photons from the photoproduction analysis. The plots have been normalised to the same number of events. In this case the DVCS photons are weighted in η^{γ}, whereas for the DIS analysis they were weighted in E_T^{γ}.

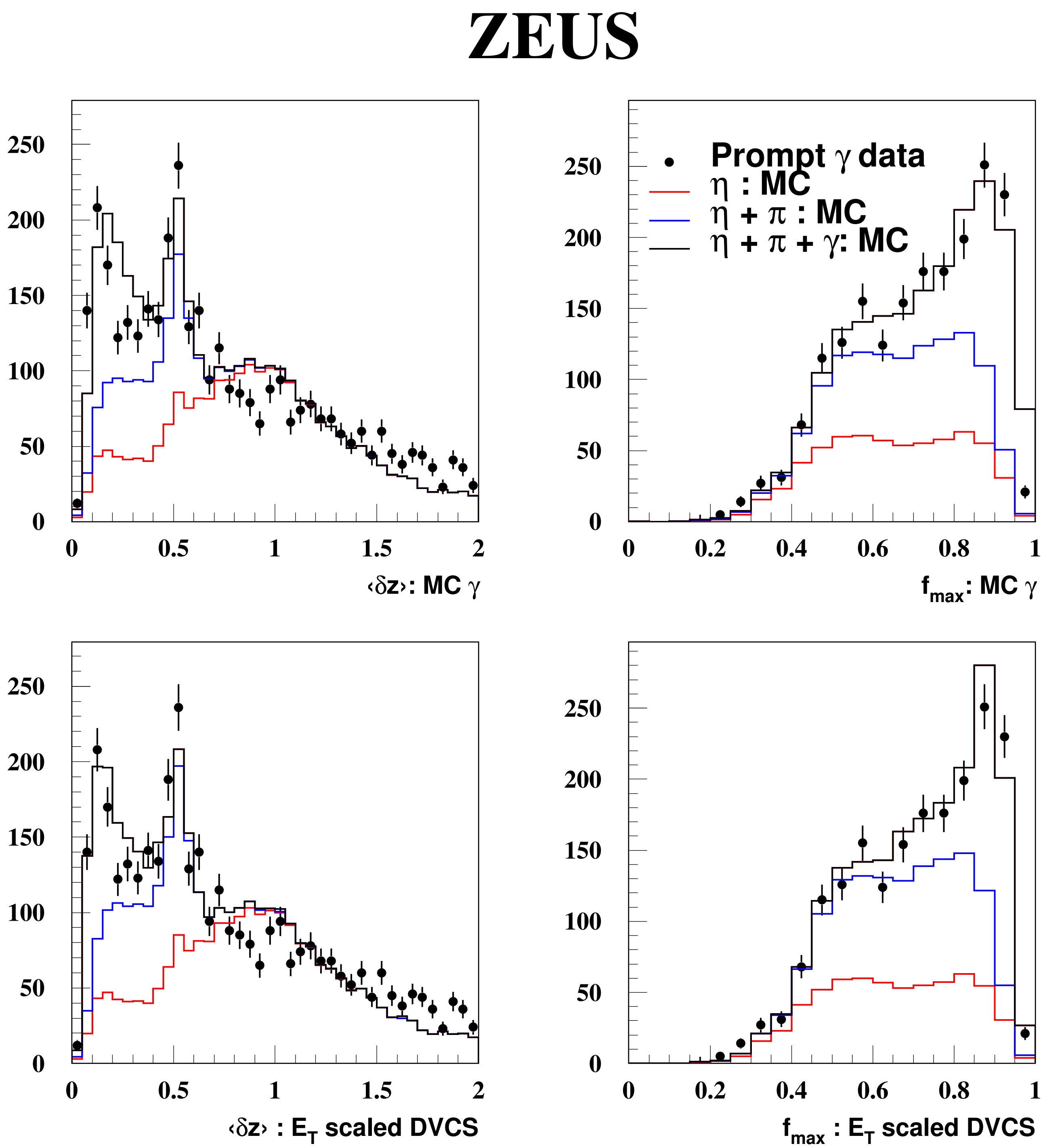

Figure 6.7: The fit to the prompt photon in DIS data. The black points are the ZEUS 96-00 prompt photon in DIS data. In the top two plots, the black line shows the Monte Carlo contributions for $\eta + \pi^0 + \gamma$. Notice that the first peak in $\langle \delta Z \rangle$ occurs approximately one bin earlier in the data, and the last point in f_{max} lies well below the prediction. In the lower plots, which use E_T-scaled DVCS data, these features have been corrected.

6.6.2 Correcting the π^0 and η distributions

The distribution of the single photon as produced from the Monte Carlo is different to that observed in the DVCS data. We must therefore assume that there is some minor but significant flaw in the simulation of single photons.

Taking this into account, it becomes obvious that there must be a similar flaw in the simulation of single π^0 and η mesons. However, there is no easily available method to provide a sample of such isolated neutral mesons in the required energy range. It is therefore necessary to apply a correction factor to the π^0 and η distributions. This is most significant in the $f_{\max}$ distribution, particularly for the extraction of the signal. When the $f_{\max}$ plots are filled, a cut has been placed in the $\langle \delta Z \rangle$ distribution, reducing the number of η mesons in the $f_{\max}$ plot. Those η mesons which remain may safely be modelled as π^0 mesons in the correction to be described below.

The method is as follows:

Let n^+ be the number of events in a sample with $f_{\max} > 0.75$.

Let n^- be the number of events in a sample with $f_{\max} < 0.75$.

Let $r = \frac{n^-}{n^+}$ for all γ, π^0 and η cases.

We observe that r_γ for photon MC is wrong and should be corrected by an amount δ to make it agree with the DVCS photon value:

$$r_\gamma^{\mathrm{DVCS}} = r_\gamma^{\mathrm{MC}} + \delta$$

This correction, however, must not change the number of events, but only the ratio of n^+ to n^-. Taking this into account and working through the algebra, we find that δ becomes

$$\delta^{\mathrm{corr}} = \delta \frac{1 + r_\gamma^{\mathrm{MC}}}{1 + r_\gamma^{\mathrm{DVCS}}}$$

The algebra is reproduced in appendix B.

This was applied to the lower $f_{\max}$ bin, where contributions from longitudinal-type events and the non-photon-like signal make the correction necessary. Both the π^0 and the η distributions underwent the correction.

This correction is applied before the extracted $f_{\max}$ ratio is used to calculate the total signal for each relevant bin. The previous corrections as described in section 6.4 are unaffected by this additional correction.

This method is not used for the systematic check on the prompt photons in DIS analysis.

6.7 DVCS photons in the prompt photon in DIS analysis

For the prompt photon in DIS analysis, the fit to the DVCS data was used as a systematic check. The cross sections were extracted from the fit using single-photon Monte Carlo. A global fit to all prompt photon in DIS data was then performed using DVCS photons instead of single-photon Monte Carlo. It was found that the DVCS fit had the result of lowering the extracted signal by a simple scale factor of -5%.

The cross sections display minimal dependence on the quality of the fit, due to the method of signal extraction which depends solely on the ratio of signal to background events in two $f_{\max}$ regions. Therefore the effect of the DVCS fit on the extracted global cross section was also a scale factor, which was taken into consideration as a -7% systematic error. The results of this study were presented in a ZEUS note written by the author [32] and were used in the prompt photons in DIS paper [9].

6.8 DVCS photons in the PHP analysis

The DVCS study was further developed for the prompt photon in photoproduction analysis. The same sample of DVCS photons was used for both the DIS and the photoproduction analyses. In the case of the photoproduction analysis, the DVCS photons were weighted in η^γ to match the prompt photon in photoproduction η^γ distribution.

For the photoproduction analysis, the DVCS sample was split into two bins in E_T, below 6 GeV and above 6 GeV. The low-E_T bin was then used to fit the first two bins in the prompt photon E_T distribution, while the high-E_T bin was used for the top three bins. The η^γ and jet variables, where appropriate, were fitted using the global energy-weighted shower shape distributions. In this way, it is possible to reduce the effect of the limited DVCS statistics and provide a more accurate fit to the shower shape, since the shower shape variables are observed to vary significantly with the energy of the cluster.

In this case, the DVCS photons are chosen as the default method of simulating the photon signal. The single photon Monte Carlo sample remains as a cross-check.

Additionally, the correction to the simulated π^0 sample described in section 6.6.2 is applied.

6.9 Using the Barrel Presampler

The proposed dijet prompt photon analysis does not provide detailed information on the precise shape of the photon cluster in the calorimeter. It is therefore not possible for the analysis to use such a shower shape analysis for reducing the neutral meson background. Instead, the analysis uses the BPRE (described in section 3.6.2) to perform a 'conversion probability' calculation.

The BPRE records a MIPS signal when a photon is converted to an e^+e^- pair in the BPRE. A single photon signal will have a relatively low probability of converting. On the other hand, a multiple-photon signal from the decay of neutral mesons will have a higher probability of conversion. By placing a direct cut on this MIPS, the background due to neutral mesons can be reduced. Single particle Monte Carlo studies carried out by my ZEUS colleagues using PYTHIA have indicated that a cut at a MIPS value of 4 will remove 27% of photons, but 51% of π^0's and 65% of η's. A lower cut, for example, at 0, removes more signal without a significant improvement in the rejection of background.

A major advantage of this method is the comparative simplicity: a direct cut allows for a more flexible analysis. On the other hand, the statistical analysis provided by the shower shape method provides much greater confidence in the signal, while the conversion probability method merely reduces the background contamination, without claiming to remove the contribution entirely.

With the added confidence and detail available from the shower shape subtraction, it is possible to demonstrate the efficiency of the MIPS cut. It was also suggested that the MIPS cut may be able to be incorporated into the shower shape analysis. A preliminary study was therefore done using the global shower shape plots and the signal extraction, for both the inclusive and the photon plus jet processes.

Figure 6.8 displays a preliminary comparison between the global shower shape variables with and without a cut at a BMIPS value of 4. It is clear that there is an overall reduction in the total number of events, and that this does not appear, by eye, to be restricted to background-dominated areas. However, normalising both plots to the same area shows an enrichment in the peak which is dominated by signal events as compared to the background-dominated peak.

This first look appears to confirm that there is a reduction in both signal and background with this cut, but that the proportional reduction of signal is much smaller. To confirm this, a more detailed study including the full signal extraction was done using the global shower shape

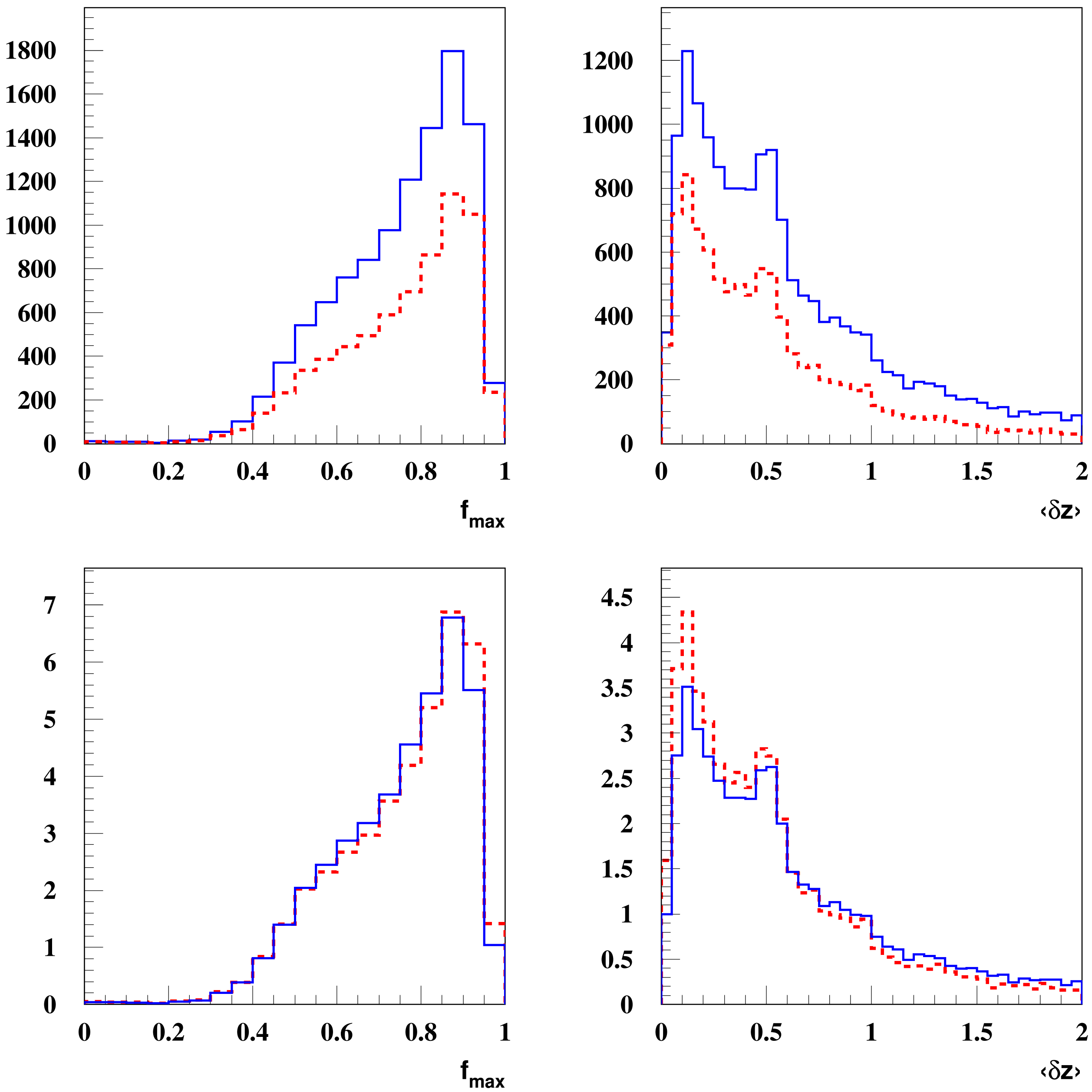

Figure 6.8: The shower shape plots in the prompt photon data with (blue) and without (red, dashed) the BPRE cut applied. The top plots show the absolute comparison, while the lower plots have been normalised to the same number of events. From the upper plots, it is clear that there is a considerable decrease in the overall number of events. From the lower plots it becomes apparent that there is an enrichment in the $\langle \delta Z \rangle$ photon peak near 0 as compared to the π^0 peak near 0.5.

for four cases: inclusive and photon plus jet processes with and without the BMIPS cut.

The fit to the data for the inclusive case for 99-00 data only is shown in figure 6.9. In this case, the number of extracted signal events without the bmips cut was 5,358. Including the BMIPS cut reduced this to 3,801, a reduction of 29%. The extracted background without the cut was 5,707, reduced to 3,181 when the cut was applied, giving a reduction in background of 44%. From this it appears that the Monte Carlo studies provided a reasonable figure for the reduction in signal, but they over-estimated the effect on the background.

Similarly, figure 6.10 displays the fit to the 99-00 data for the photon plus jet process. In this case, the extracted signal was 1,841 without the application of the cut and 1,247 when the cut is applied, a reduction of 32%. The extracted background was found to be 1,753 without the cut and 815 with the cut, giving a reduction of 53%. The dijet method, for which the Monte Carlo study was performed, can only measure the photon plus jet cross-section. For this process, the Monte Carlo provides a better estimate of the effect of the cut on the background, but it appears to under-estimate the effect on the signal.

From these figures it appears that, within the scope of the current analysis, the BPRE cut is largely unnecessary. While it does have a larger effect on reducing the background than it does on the signal, it does not add significantly to the level of confidence in our understanding of the background processes. It therefore contributes little to the efficiency of the statistical background extraction. We can further conclude that the subtraction of the background is incomplete using this method, and there will be some contamination of the cross-section from neutral meson decay in any analysis which relies on this cut. It is also true that the BMIPS cut may only be applied to data taken after 1999 in a ZEUS analysis, since the BPRE was not installed before then. Incorporating it into the current analysis would either complicate the statistical extraction by applying the cut to only a small subsample of the data or would

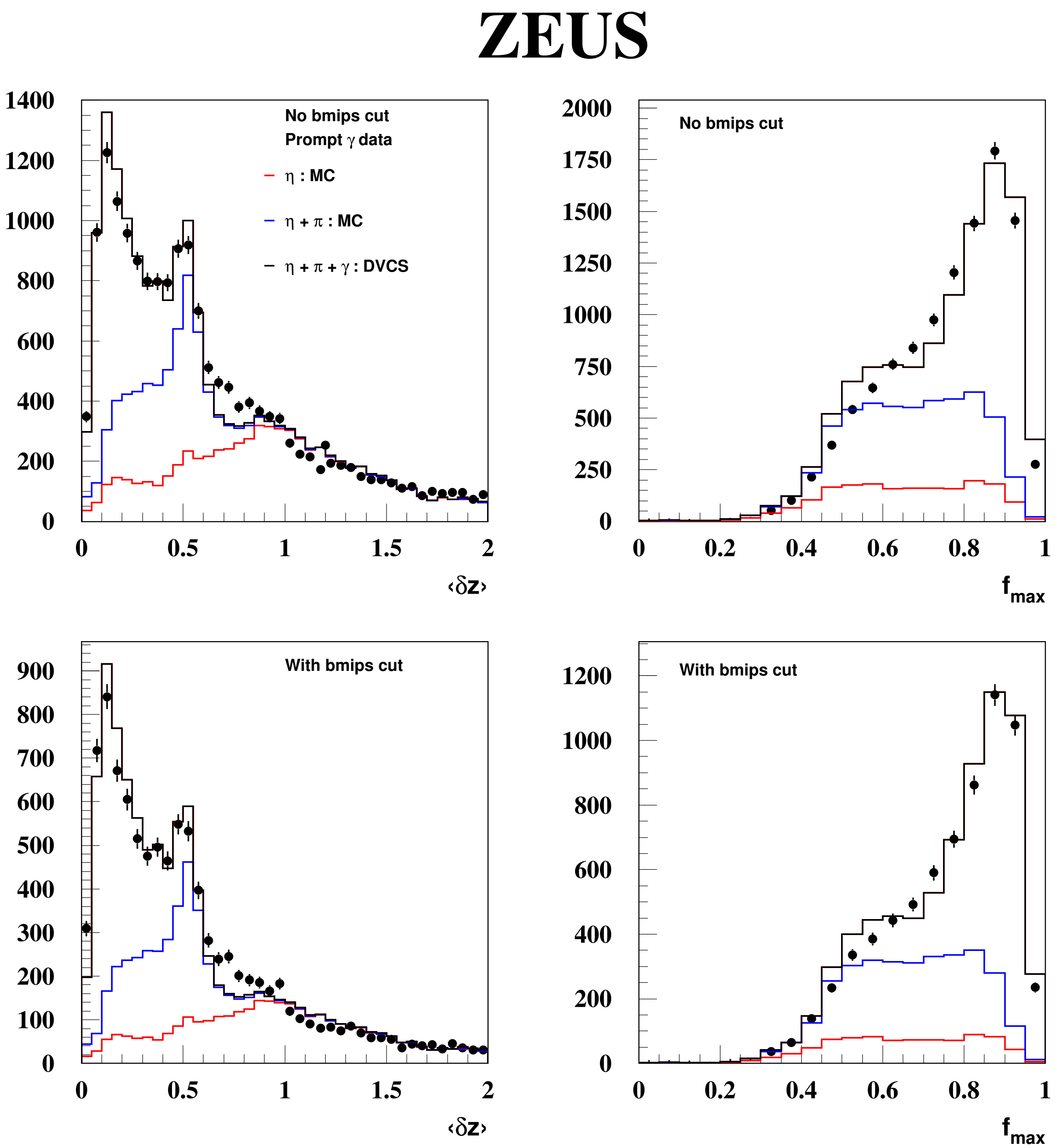

Figure 6.9: The shower shape fit to the data using DVCS photons, with π^0's and η's from single particle Monte Carlo for the inclusive process. The top plots have no BMIPS cut, while the lower plots include a cut at a BMIPS value of 4.

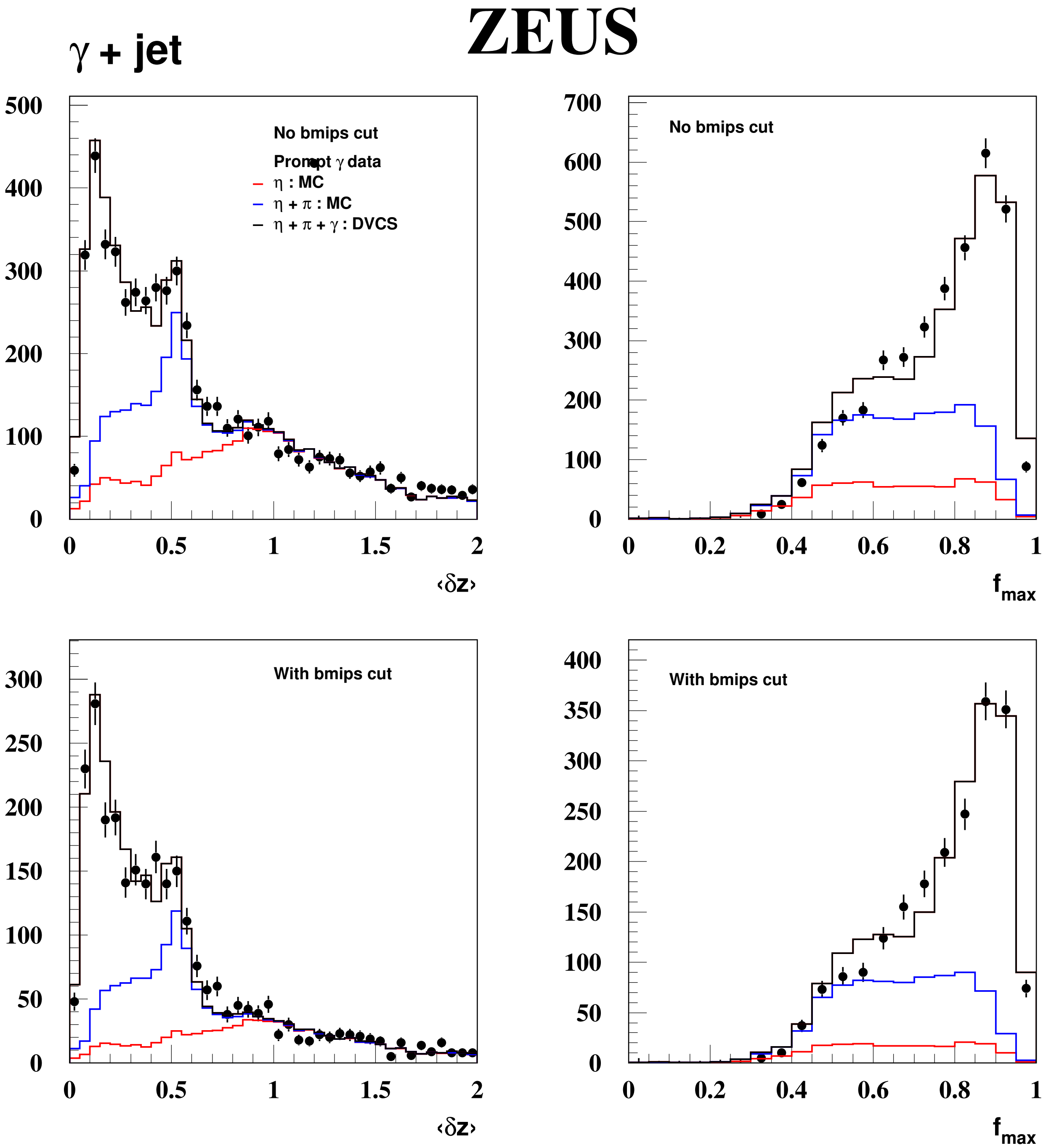

Figure 6.10: The shower shape fit to the 99-00 data using DVCS photons, with π^0's and η's from single particle Monte Carlo for the photon plus jet process. The top plots have no BMIPS cut, while the lower plots include a cut at a BMIPS value of 4.

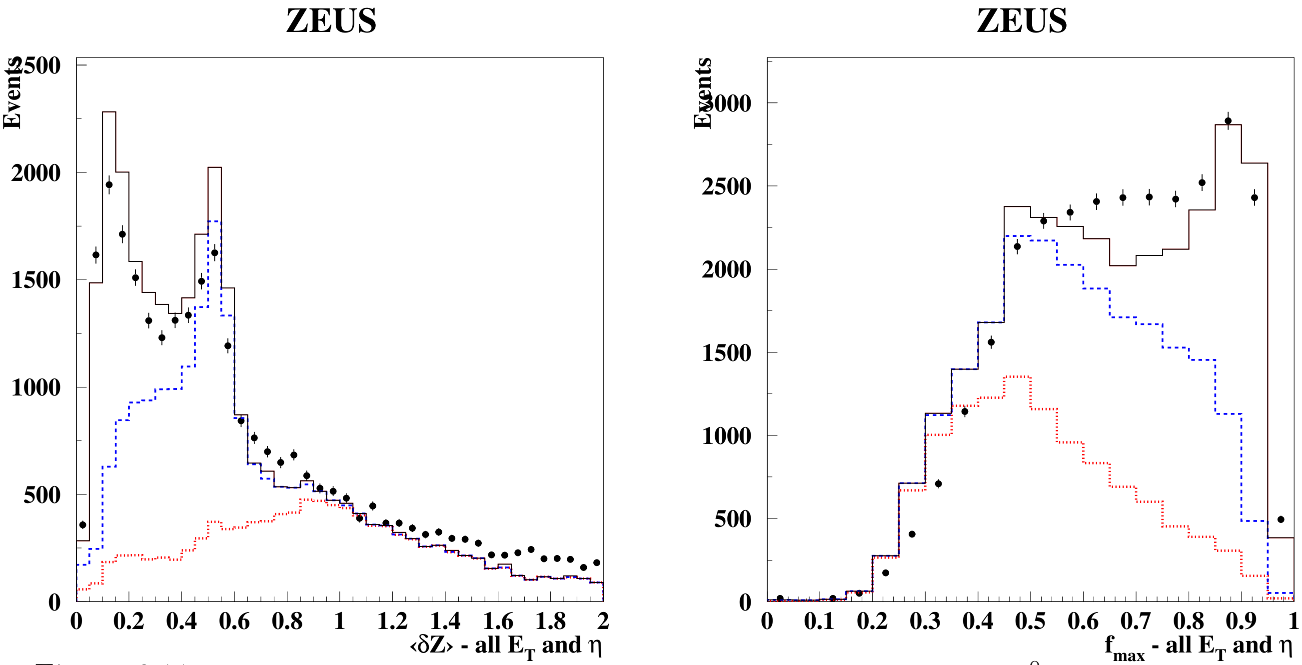

Figure 6.11: The shower shape fit to the data using DVCS photons, with π^0's and η's from single particle Monte Carlo for the inclusive photoproduction analysis.

require that the as-yet unpublished and unstudied data from 1998 is not incorporated into the analysis.

This is not to say that the BPRE cannot be used for the prompt photon analysis, however. By its nature, the signal extraction method relies on a certain number of both signal and background events being found. As we go to higher values of E_T^γ, the contamination from these largely low-E_T neutral mesons becomes significantly less. At the same time, the number of prompt photon candidates found becomes sufficiently small that a statistics-based signal extraction becomes inefficient. In such a situation, the BMIPS cut may allow a prompt photon analysis to be carried to much higher-E_T^γ than the present method, significantly extending the scope of the analysis.

6.10 The completed method and subtraction

In order to extract the prompt photon signal for the final cross section for the prompt photon in photoproduction analysis, the neutral meson background is subtracted as follows.

- A sample of single particle Monte Carlo is generated using JetSet, simulating photons, π^0's and η's. Each sample has a flat energy spectrum.
- Similarly, a sample of DVCS photons is obtained from the data, using the cuts described in section 6.5.
- The single particle Monte Carlo samples and the DVCS photons are weighted in E_T to match the prompt photon data.
- The shower shape variables, $f_{\max}$ and $\langle \delta Z \rangle$, are generated in bins of E_T^{γ} and η^{γ}, and E_T^{jet} and η^{jet} for the photon plus jet analysis, for the single particle Monte Carlo samples, the DVCS data and the prompt photon data. The $f_{\max}$ distribution is corrected in the single particle Monte Carlo samples as described in section 6.4.
- For each bin in E_T^{γ} and η^{γ}, and in the case of the photon plus jet analysis, E_T^{jet} and η^{jet}, a fit of the DVCS photons and the single particle Monte Carlo π^0's and η's to the prompt photon data is performed.
- From each fit, a value for the number of 'good' and 'poor' events is extracted.
- The 'good' and 'poor' values extracted for the single pions and η-mesons are corrected using the method described in subsection 6.6.2 and appendix B.
- From the 'good' and 'poor' numbers, a value for the extracted signal and background is extracted, using equations 6.1 and 6.2.

- The errors on the signal and background are similarly extracted from the fits using equations 6.3 and 6.4.

The global fit, that is, the fit in all bins of E_T and η, is displayed in figure 6.11.

Chapter 7

Inclusive prompt photons

The inclusive prompt photon process at HERA is $e^{\pm}p \rightarrow \gamma + X$, where the photon is of sufficient E_T and isolated, and X represents any other combination of particles in the final state. In measuring the cross section for the inclusive process no jet cuts are applied, so as not to introduce a dependence on the understanding of the hadronisation process.

For the inclusive process, the cross section is measured with respect to the transverse energy, E_T^{γ}, and the pseudorapidity, η^{γ}, of the photon.

7.1 Acceptance corrections

The acceptance corrections are calculated as described in section 4.7. In order to unfold the cross section, the acceptance corrections must be calculated on a bin-by-bin basis for each of the variables by which the cross section will be measured. The acceptance corrections are shown in figure 7.1. There is very little variation in the required correction factors with either E_T^{γ} or η^{γ}, which means that the value of the correction does not vary systematically with either of the key variables.

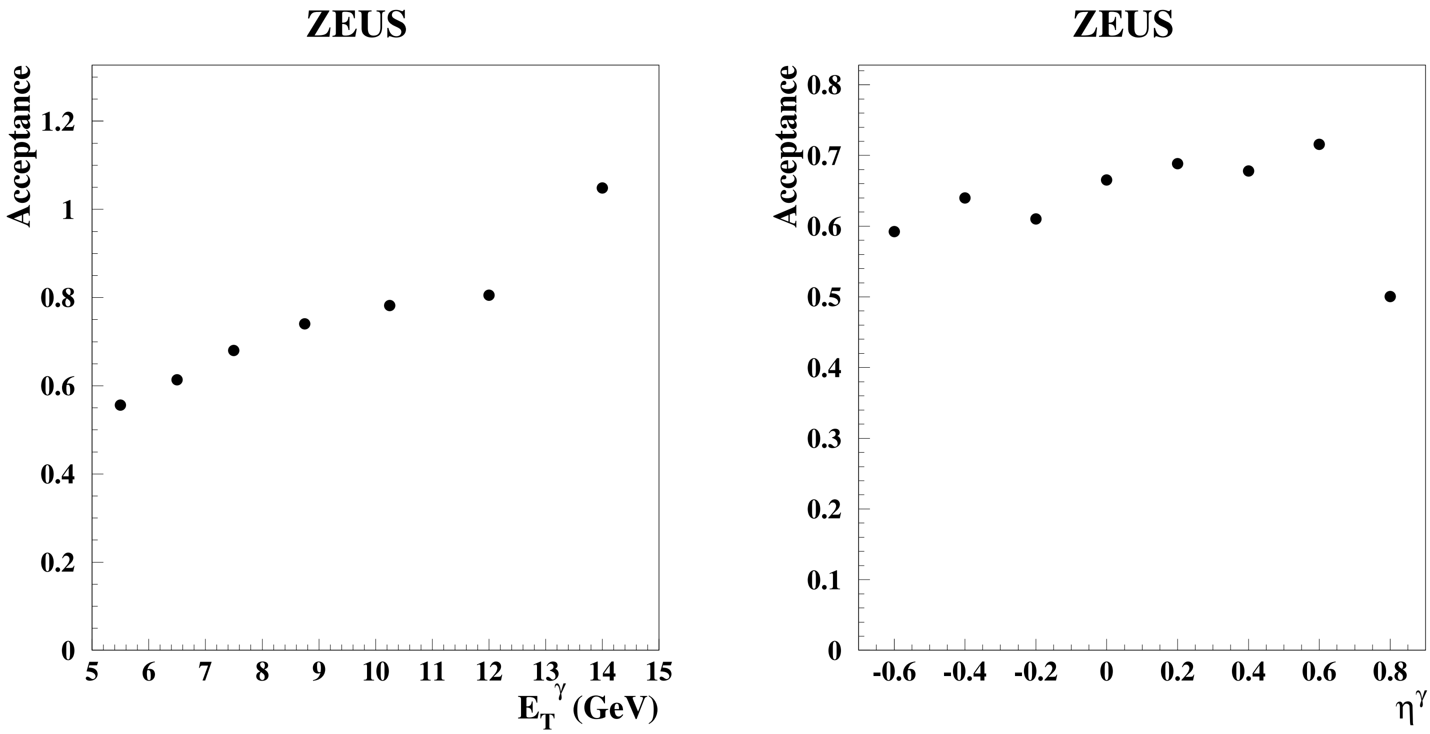

Figure 7.1: The acceptance corrections as calculated for E_T^γ on the left and η^γ on the right. The statistical errors are small.

The acceptance corrections, as described, are a key part of the process of unfolding the cross section. Such corrections allow a compensation for differences between the detected event and the true event to be made, providing a measurement which does not depend on the response of the detector.

7.2 Systematic uncertainties

There are a number of possible ways in which uncertainty can enter the measurement. The statistical errors are calculated to provide a measurement of the statistical uncertainty. It is also important, however, to provide an estimate of the systematic effects which could enter the measurement.

In this analysis, the following possible sources of systematic errors are studied:

- Performing corrections with HERWIG instead of PYTHIA Monte Carlo samples.
- The calorimeter energy scale is increased and decreased by 3%.
- The cut on the Z_{vertex} was tightened to $|Z_{\mathrm{vertex}}| < 20$cm.
- The cuts on y_{JB}, E_T^γ and η^γ are varied within the resolution of the measurement.
- The cut on $\langle \delta Z \rangle$ was increased to 0.75.
- The isolation requirement was modified such that the maximum energy in a unit cone around the photon which did not originate from the photon was 5% and 15% of the photon energy.
- The track requirement was loosened to no tracks within 0.2 radians and tightened to no tracks within 0.4 radians.
- The π^0 corrections were halved.
- The single-γ Monte Carlo was used in place of the DVCS photons in the background subtraction.
- The numbers extracted from the background fit were taken from the Monte Carlo instead of the data.

These 18 checks were carried out and the percentage changes to the cross section are plotted on figure 7.2. The systematic errors on a bin-by-bin basis are plotted in figures 7.3 and 7.4.

The effect of each systematic check on the calculated cross section is shown in table 7.1.

There is a large discrepancy between the measured cross section where PYTHIA is used for acceptance corrections and that calculated using HERWIG. Because there is such a large

Systematic	**Number**	**Cross Section Change(%)**
PYTHIA $\rightarrow$ HERWIG	1	-38.9
CAL scale +3%	2	-1.2
CAL scale -3%	3	-2.7
$\lvert Z_{\text{vertex}}\rvert < 20$cm	4	7.2
$y_{\text{JB}} > 0.2 \rightarrow y_{\text{JB}} > 0.2 - \text{res.}$	5	-1.6
$y_{\text{JB}} < 0.8 \rightarrow y_{\text{JB}} < 0.8 + \text{res.}$	6	1.3
$E_T^\gamma > 5 \rightarrow E_T^\gamma > 5 - \text{res.}$	7	5.0
$E_T^\gamma < 16 \rightarrow E_T^\gamma < 16 + \text{res.}$	8	-0.05
$\eta^\gamma > -0.7 \rightarrow \eta^\gamma > -0.7 - \text{res.}$	9	0.7
$\eta^\gamma < 1.1 \rightarrow \eta^\gamma < 1.1 + \text{res.}$	10	-0.6
$\langle \delta Z \rangle < 0.65 \rightarrow \langle \delta Z \rangle < 0.75$	11	-0.2
$E(\text{not from } \gamma) < 0.1 E_\gamma \rightarrow E(\text{not from } \gamma) < 0.05 E_\gamma$	12	1.1
$E(\text{not from } \gamma) < 0.1 E_\gamma \rightarrow E(\text{not from } \gamma) < 0.15 E_\gamma$	13	-0.6
Distance to nearest track < 0.3 radians $\rightarrow$ 0.2 radians.	14	1.0
Distance to nearest track < 0.3 radians $\rightarrow$ 0.4 radians.	15	-4.0
π^0 correction is halved	16	1.9
DVCS $\rightarrow$ Single γ Monte Carlo	17	-5.8
Use Monte Carlo to extract signal instead of data	18	$\pm$ 20.2

Table 7.1:

The effect each systematic check has on the cross section. The numbers refer to the axes of the figures. The abbreviation 'res' represents the resolution of the measurement in question.

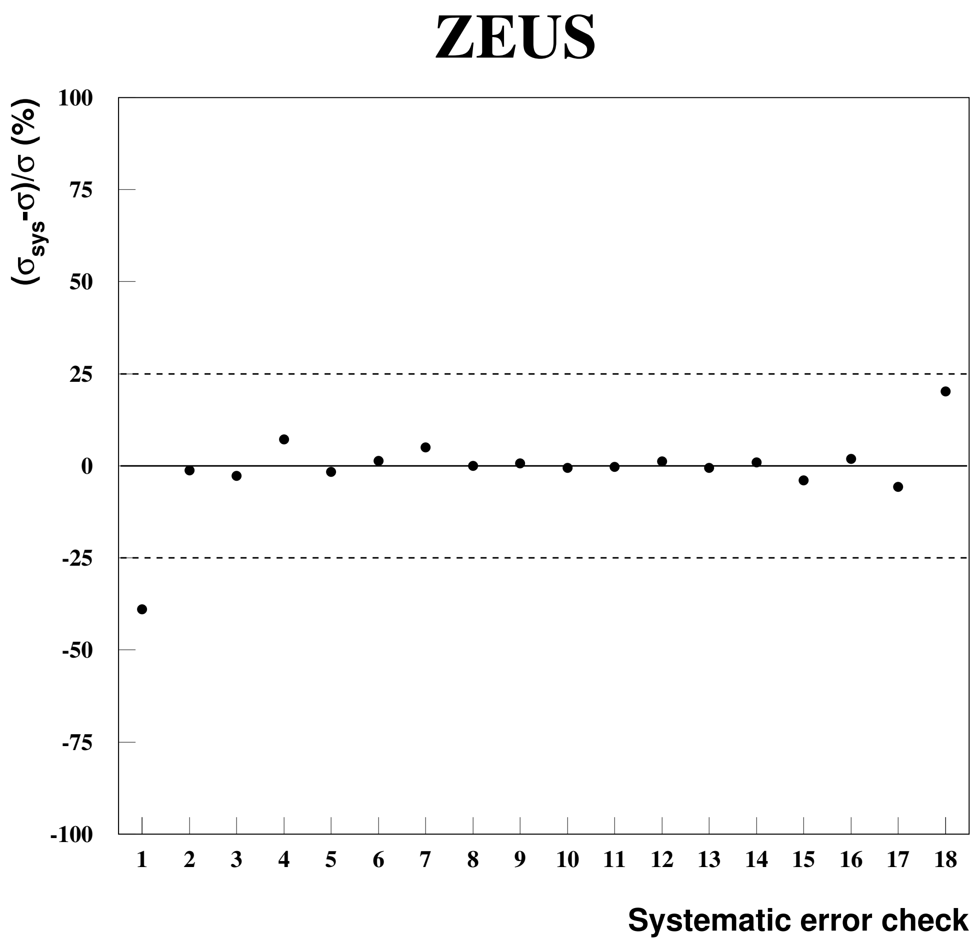

Figure 7.2: A summary of the global effects of the systematic errors on the calculated cross section, displayed as a percentage change from the measured results. The zero-line represents the calculated cross section with no check applied, and the numbers on the x-axis correspond to the numbers shown in table 7.1. Systematic error 18 is shown as positive, although it is applied symmetrically.

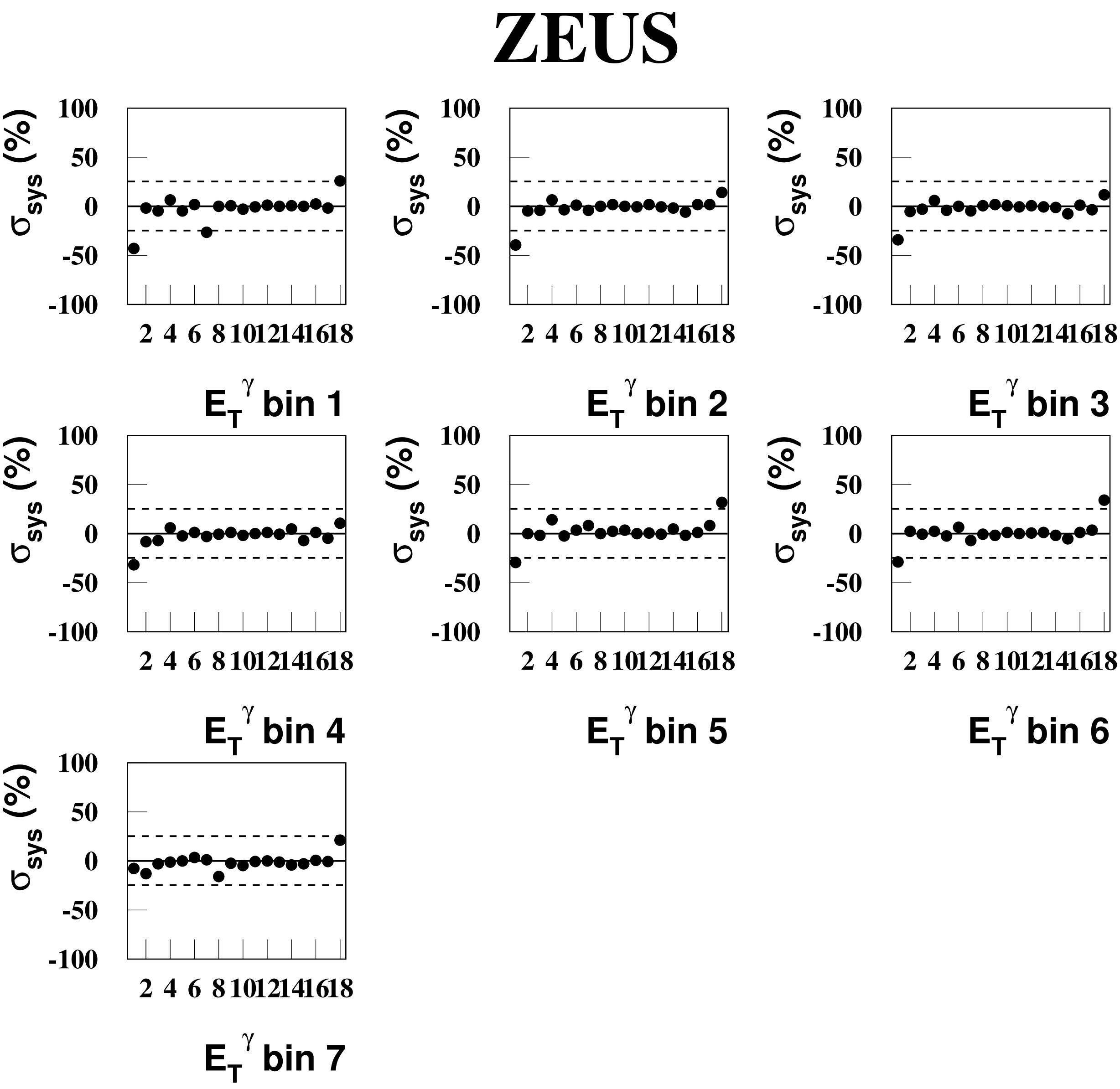

Figure 7.3: As in figure 7.2, the systematic uncertainties are displayed as percentages of the calculated cross section and the numbers correspond to the numbers shown in table 7.1. The seven graphs show the systematic uncertainties in each bin in E_T^γ. Systematic error 18 is shown as positive, although it is applied symmetrically.

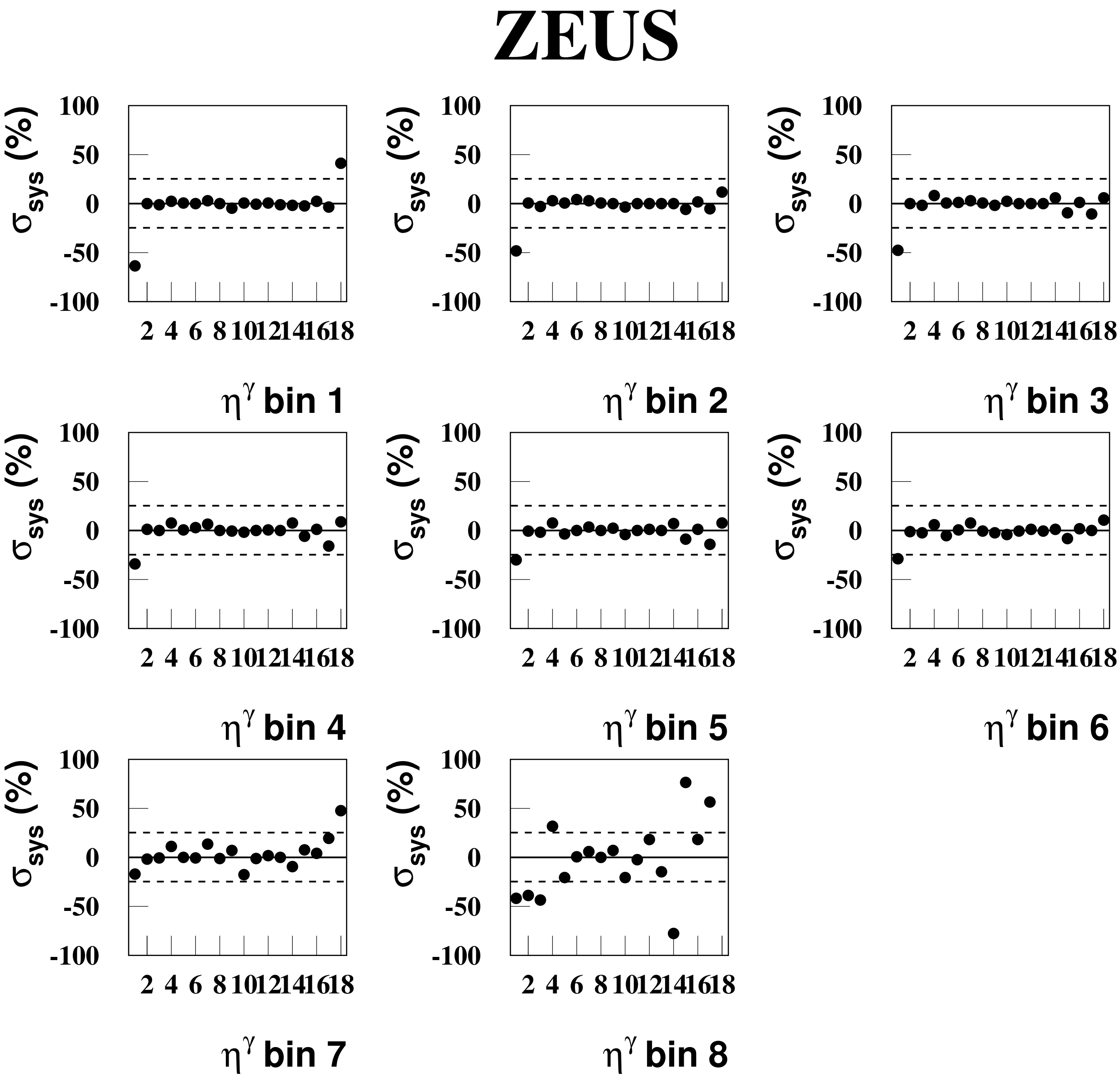

Figure 7.4: The systematic uncertainties in bins of η^γ. As before, systematic error 18 is shown as positive, although it is applied symmetrically.

difference and the agreement between the data and the HERWIG prediction is not good, the HERWIG systematic is displayed here but not included on the plots of the cross sections.

The remaining systematic errors are combined in quadrature to provide an overall value for the systematic errors.

7.3 Cross sections

The definition of the cross section with respect to quantity R in bin i is as follows:

$$\frac{d\sigma}{dR_i} = \frac{N_i}{A_i w_i \int Ldt} \tag{7.1}$$

where N_i is the number of events in bin i, A_i is the acceptance correction in bin i, w_i is the width of bin i and $\int Ldt$ is the total integrated luminosity.

The statistical error on the cross section in bin i, r_i, is calculated from the error on the extracted signal and the error on the acceptances. Taking these into account, it follows that:

$$r_i = \sqrt{\left(\frac{\delta N_i}{A_i w_i \int Ldt}\right)^2 + \left(\frac{N_i \delta A_i}{A_i^2 w_i \int Ldt}\right)^2} \tag{7.2}$$

In the case of the inclusive prompt photon process, the cross sections may be measured with respect to the E_T and the η of the photon. In this case, the number of events, E_i, is extracted on a bin-by-bin basis from the background subtraction process. The statistical error is calculated as shown, and the systematic errors are added to the statistical errors in quadrature on a bin-by-bin basis.

7.4 Comparisons to the previous ZEUS analysis

Comparisons with the previous inclusive prompt photon analysis have been made for the 96-97 dataset as well as the full 96-00. Such a comparison provides a case for the reliability and

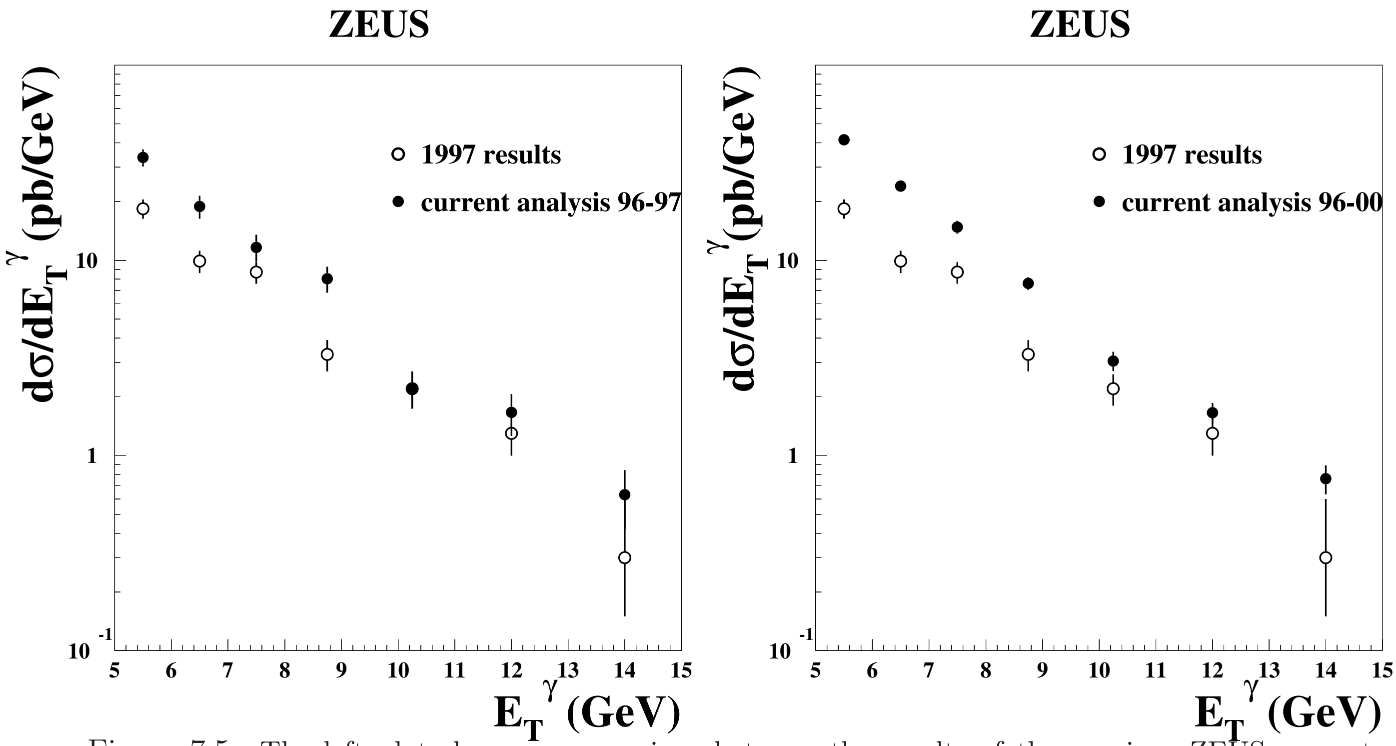

Figure 7.5: The left plot shows a comparison between the results of the previous ZEUS prompt photon in photoproduction analysis, carried out in 2000, and the new analysis using only 96-97 data. In the right plot, the current analysis is expanded to include the full 96-00 dataset, while the points from the previous analysis remain the same.

stability of the measurement and the method. The comparison uses the cross section in terms of E_T^γ, since the η^γ cross section was published using a much smaller range of E_T^γ than was used for the E_T^γ cross section, making a direct comparison difficult.

Figure 7.5 shows a comparison between the current analysis using the 96-97 dataset only and the previously published ZEUS cross section in E_T^γ. The general shape of the distributions show good agreement, although the analyses do differ in detail and magnitude, particularly at low-E_T^γ.

The comparison is also extended to the full 96-00 dataset. Although the comparison is not substantially changed, the current analysis lies slightly higher above the previous results than did the 96-97 results. This is partially due to a slight decrease in the acceptance seen between the newer data with protons at 920 GeV and the older data, which used protons at 820 GeV. The improvement in the statistical errors, shown on the plot, is striking.

Some changes have been made to the analysis since the previous paper, most notably the use of the DVCS photons instead of simulated single photons in the background model. These may account for the fact that the difference between the two analyses using the 96-97 dataset is most marked in the low-E_T^γ region, where the observed background due to neutral mesons is highest.

7.5 Comparisons to Monte Carlo samples

Cross sections are presented for the variables E_T^γ and η^γ using the full 96-00 HERA I dataset. The sample is an inclusive photoproduction sample containing an isolated photon in the energy range $5 \leq E_T^\gamma \leq 15$ GeV and the pseudorapidity range -0.7 $\leq \eta^\gamma \leq$ 0.9. The isolation criteria is as defined in section 5.5.

Comparisons to the PYTHIA and HERWIG Monte Carlo programmes are shown in figures 7.6 and 7.7.

The agreement between the data and the Monte Carlo sample in the E_T^γ distribution is good for both the PYTHIA and the HERWIG samples. In η^γ, the PYTHIA distribution mirrors the data well, particularly in the rear direction. However, in the forward direction there is a slight excess seen in the PYTHIA distribution. The HERWIG η^γ distribution does not agree with the data.

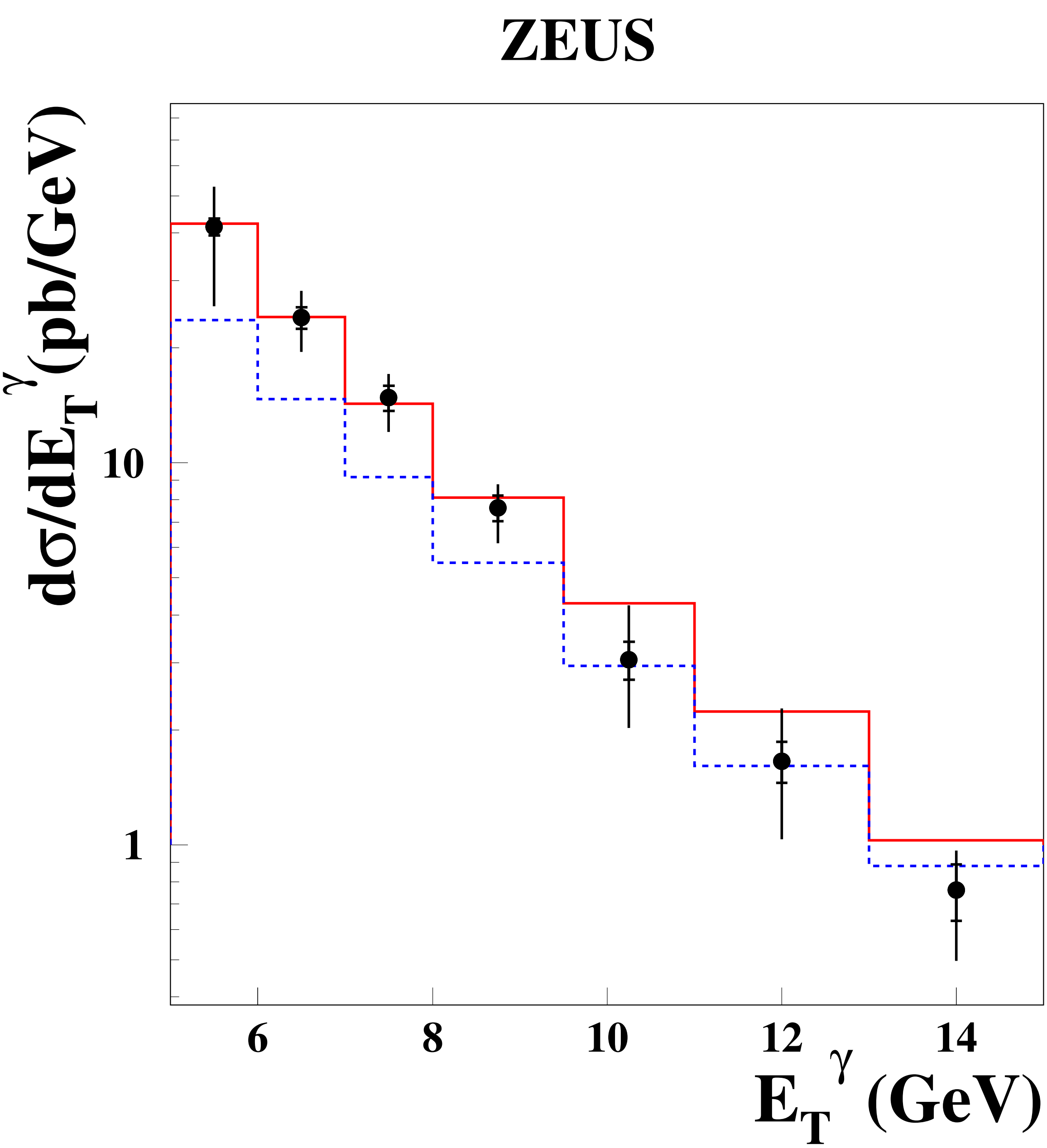

Figure 7.6: The cross section including all systematic and statistical errors with respect to E_T^γ. E_T^γ is shown in GeV. PYTHIA is displayed in red, while HERWIG is the blue dashed histogram.

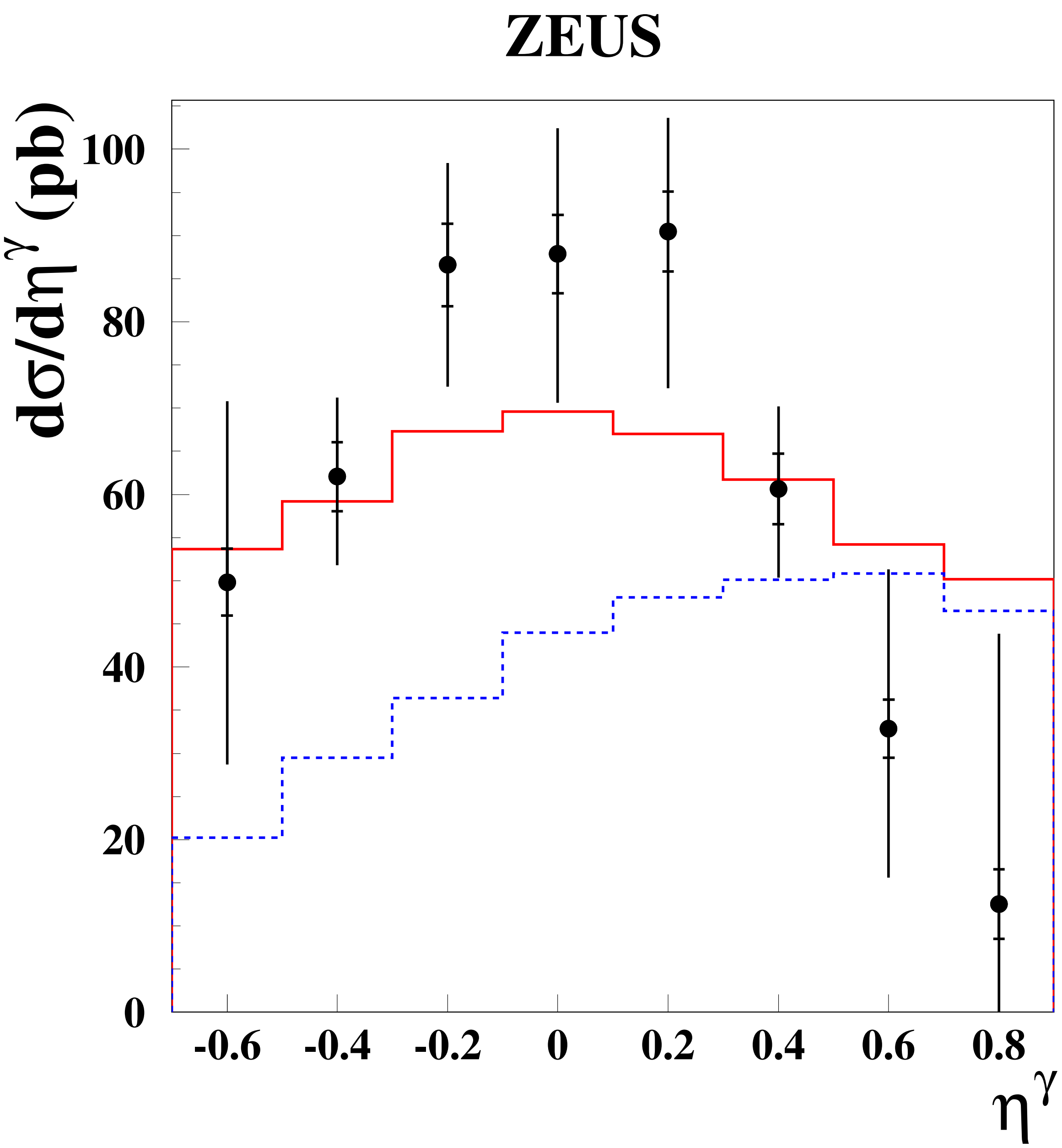

Figure 7.7: The cross section including all systematic and statistical errors with respect to η^{γ}. Shown in red is the results from PYTHIA, HERWIG is represented by the blue dashed histogram.

Chapter 8

The photon plus jet process

Requiring that the prompt photon process also contains a jet constrains the process. However, a jet cannot be measured to the same accuracy as a photon, and the effect of hadronisation must be taken into account and corrected for.

Otherwise, the method for measuring prompt photons with a jet is much as was used for the inclusive process. Further, the cross sections may also be measured with respect to the jet variables, $E_T^{\rm jet}$ and $\eta^{\rm jet}$. Hence we can use our understanding of the photon to provide information about the jet itself.

8.1 Acceptance corrections

The acceptance corrections for the photon plus jet process are calculated as described in section 4.7. The acceptances are shown in figure 8.1, calculated from the efficiencies and purities displayed in figures 4.6 and 4.5.

In the photon plus jet analysis, the cross sections are measured with respect to E_T^γ, η^γ, $E_T^{\rm jet}$ and $\eta^{\rm jet}$. The acceptance corrections must therefore also be calculated in those variables.

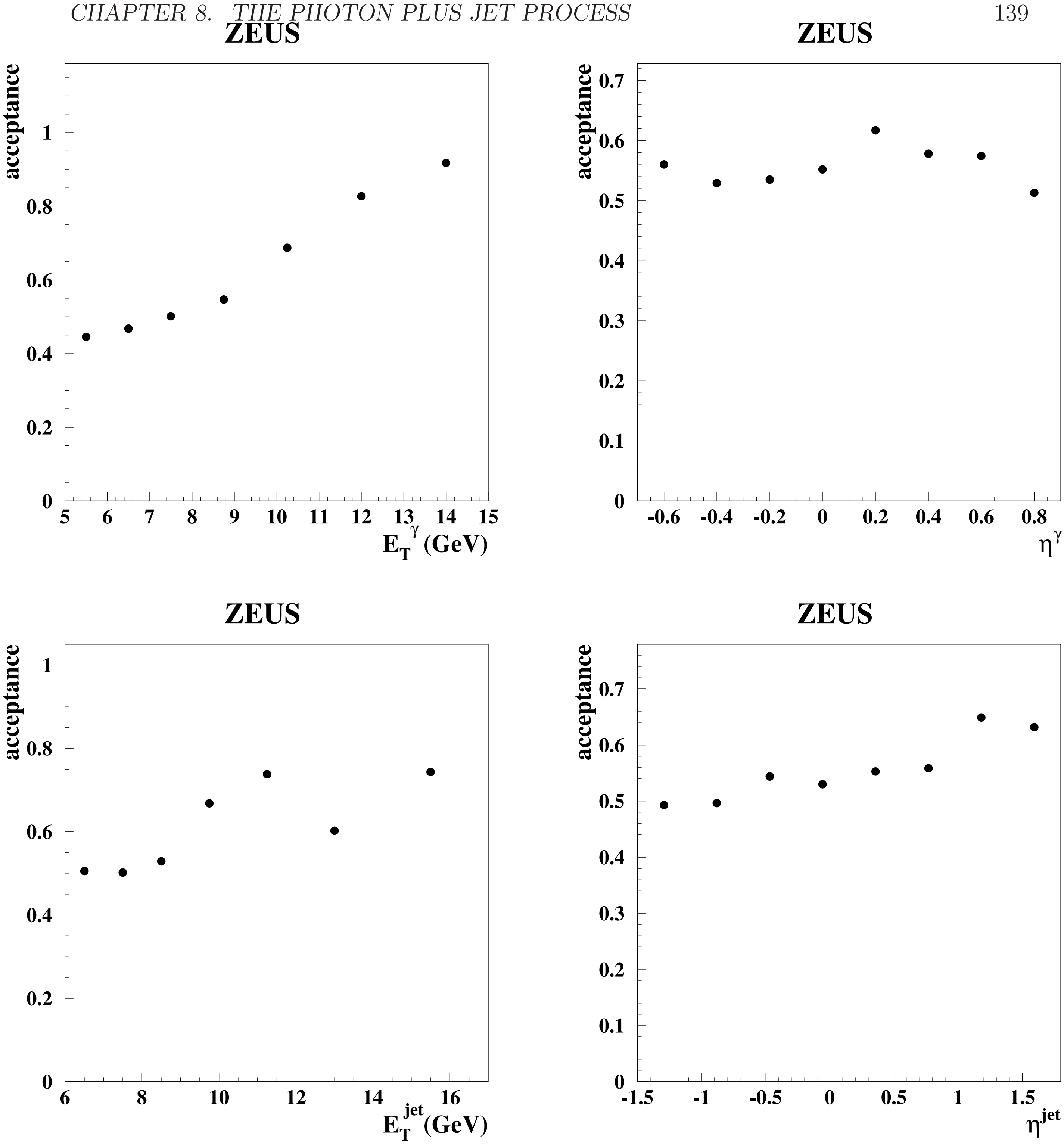

Figure 8.1: The acceptance corrections as calculated for E_T^{γ} on the left and η^{γ} on the right are shown in the top two plots. The lower plots show the calculated acceptance corrections for E_T^{jet} and η^{jet}.

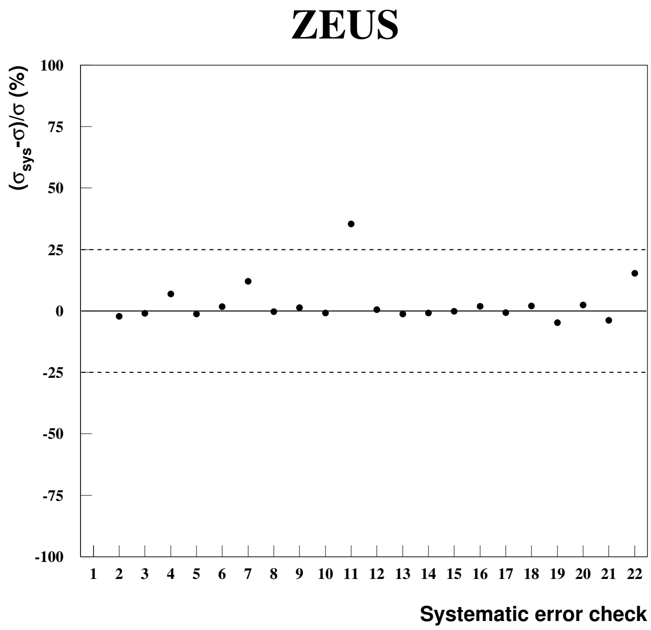

Figure 8.2: A summary of the global effects of the systematic errors on the calculated cross section, displayed as a percentage change from the measured results. The zero-line represents the calculated cross section with no check applied, and the numbers on the x-axis correspond to the numbers shown in table **??**.

There is little variation in the size of the correction in either of the four variables studied. The correction therefore does not significantly depend on the transverse energy or pseudorapidity of either the photon or the jet, which is as expected.

8.2 Systematic uncertainties

The systematic checks are much the same as for the inclusive prompt photon process, with the inclusion of varying the jet cuts by the resolution: that is, the cuts on $E_T^{\rm jet}$ are increased and decreased by the resolution of the measurement, as are the cuts on $\eta^{\rm jet}$. The effects of the systematic uncertainties on the photon plus jet cross section are shown in table 8.1.

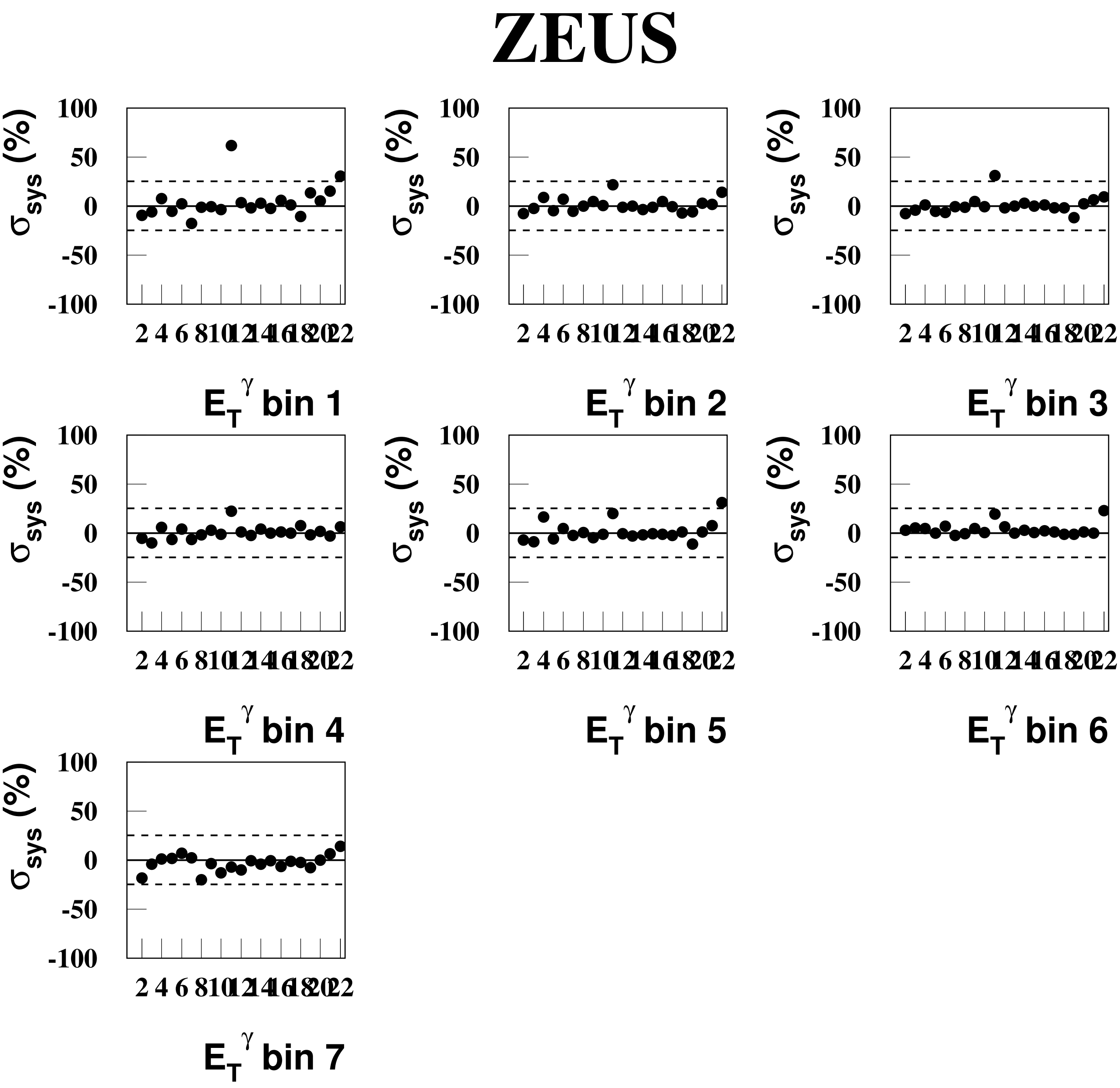

Figure 8.3: The global effects of the systematic errors on the calculated cross section displayed as a percentage change from the measured results, in bins of E_T^γ. As for the global plot, the zero-line represents the calculated cross section with no checks applied.

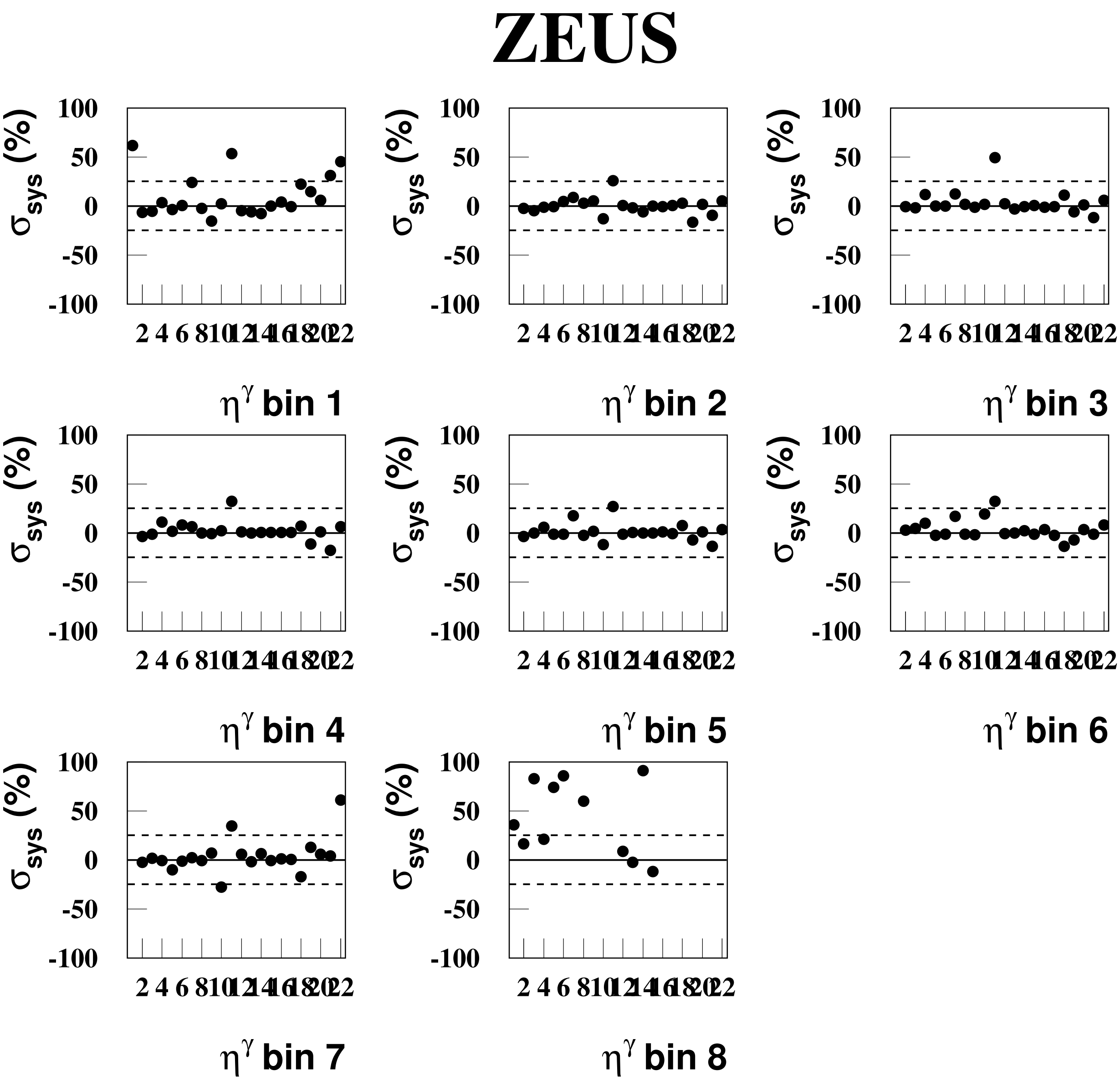

Figure 8.4: The global effects of the systematic errors on the calculated cross section displayed as a percentage change from the measured results, in bins of η^γ. As for the global plot, the zero-line represents the calculated cross section with no checks applied.

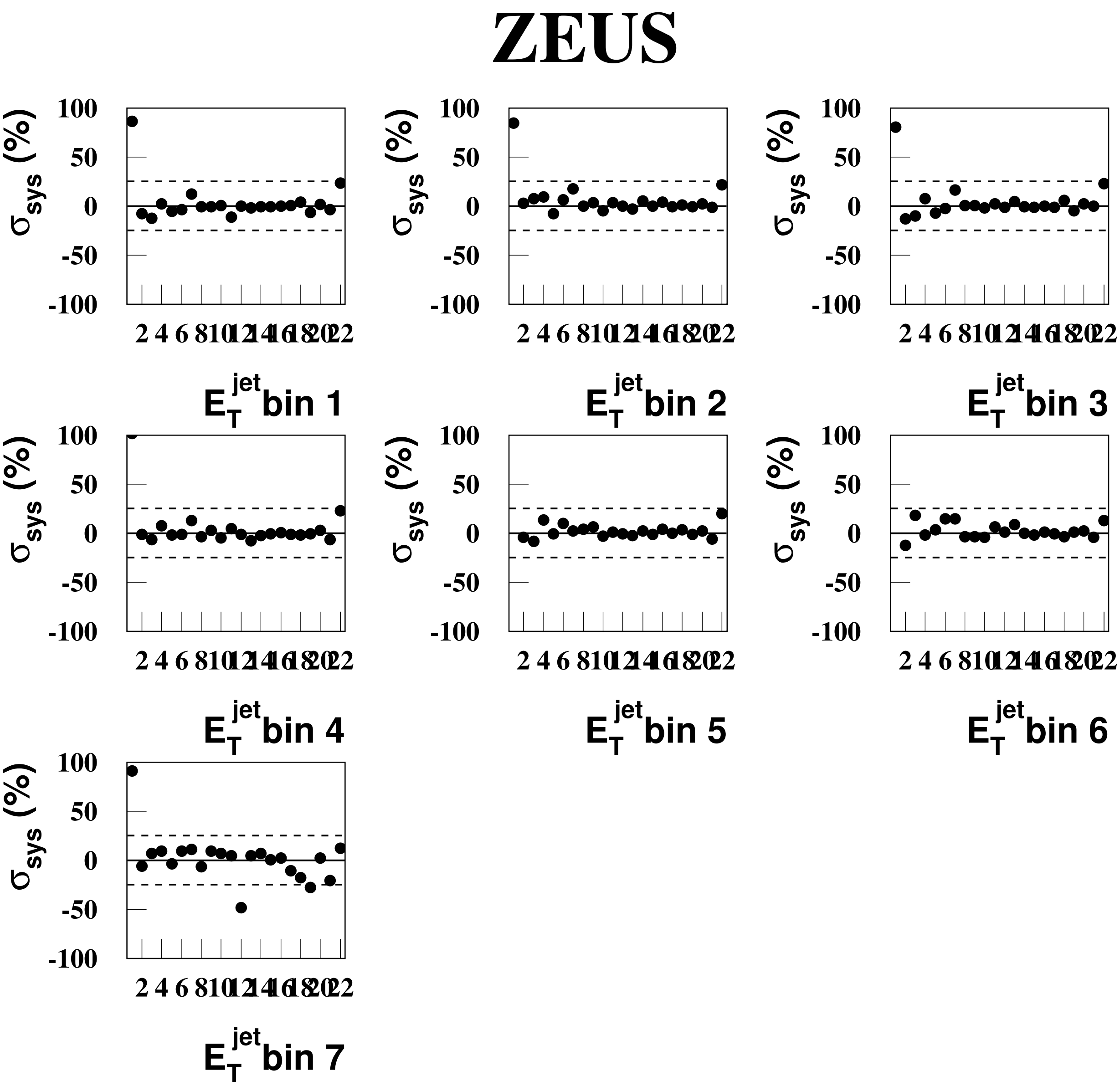

Figure 8.5: The global effects of the systematic errors on the calculated cross section displayed as a percentage change from the measured results, in bins of $E_T^{\rm jet}$. As for the global plot, the zero-line represents the calculated cross section with no checks applied.

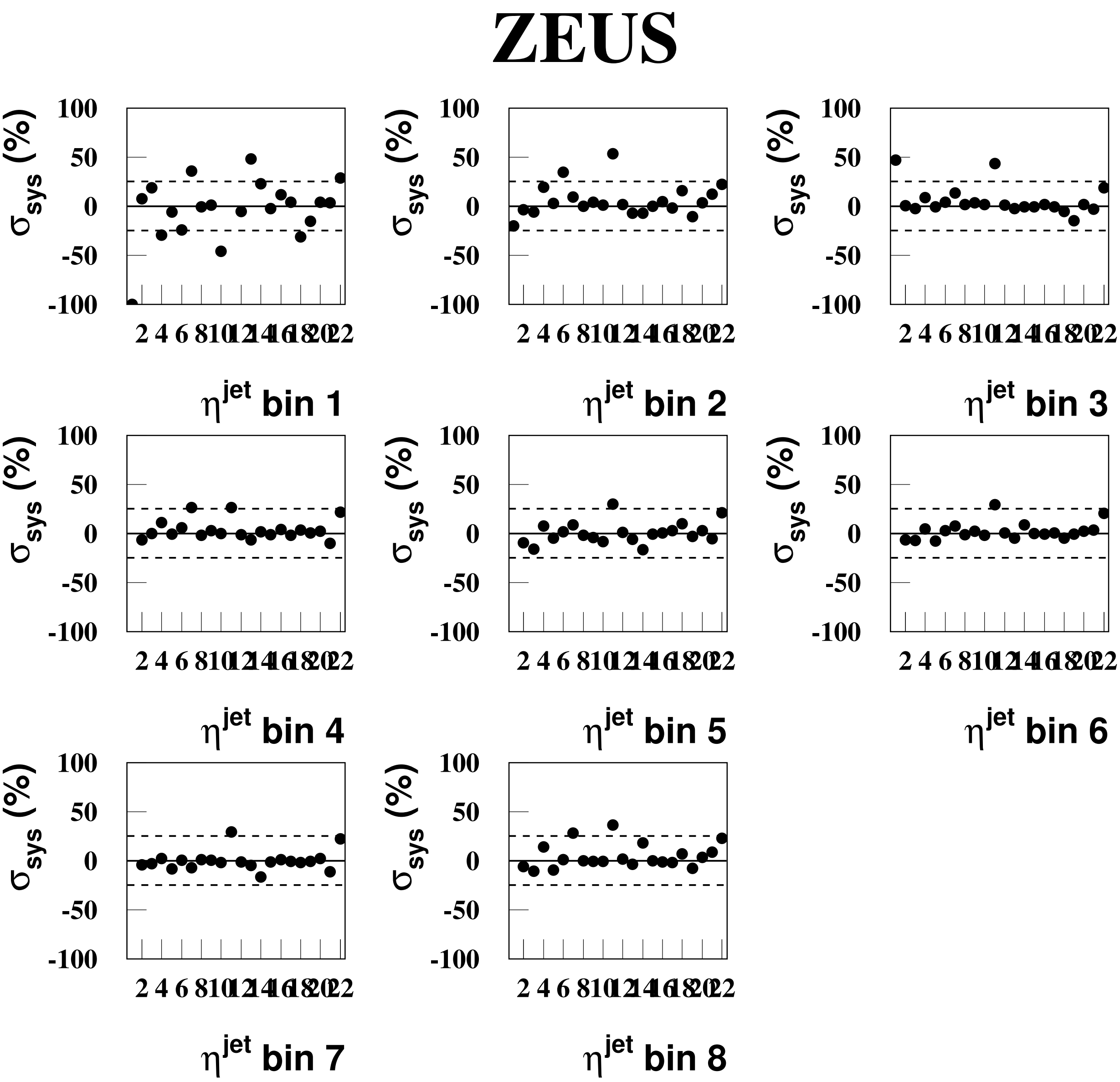

Figure 8.6: The global effects of the systematic errors on the calculated cross section displayed as a percentage change from the measured results, in bins of η^{jet}. As for the global plot, the zero-line represents the calculated cross section with no checks applied.

Systematic	**Number**	**Cross Section Change (%)**
PYTHIA $\rightarrow$ HERWIG	1	175.2
CAL scale +3%	2	-2.2
CAL scale -3%	3	-1.0
$\lvert Z_{\text{vertex}}\rvert < 20$cm	4	6.9
$y_{\text{JB}} > 0.2 \rightarrow y_{\text{JB}} > 0.2 -$ res.	5	-1.3
$y_{\text{JB}} < 0.8 \rightarrow y_{\text{JB}} < 0.8 +$ res.	6	1.8
$E_T^\gamma > 5 \rightarrow E_T^\gamma > 5 -$ res.	7	12.0
$E_T^\gamma < 16 \rightarrow E_T^\gamma < 16 +$ res.	8	-0.3
$\eta^\gamma > -0.7 \rightarrow \eta^\gamma > -0.7 -$ res.	9	1.4
$\eta^\gamma < 1.1 \rightarrow \eta^\gamma < 1.1 +$ res.	10	-0.8
$E_T^{\text{jet}} > 6 \rightarrow E_T^{\text{jet}} > 6 -$ res.	11	35.5
$E_T^{\text{jet}} < 17 \rightarrow E_T^{\text{jet}} < 17 +$ res.	12	0.6
$\eta^{\text{jet}} > -1.6 \rightarrow \eta^{\text{jet}} > -1.4 -$ res.	13	-1.2
$\eta^{\text{jet}} < 2.4 \rightarrow \eta^{\text{jet}} < 2.6 +$ res.	14	-0.8
$\langle \delta Z \rangle < 0.65 \rightarrow \langle \delta Z \rangle < 0.75$	15	-0.1
$E(\text{not from } \gamma) < 0.1E_\gamma \rightarrow E(\text{not from } \gamma) < 0.05E_\gamma$	16	1.8
$E(\text{not from } \gamma) < 0.1E_\gamma \rightarrow E(\text{not from } \gamma) < 0.15E_\gamma$	17	-0.7
Distance to nearest track < 0.3 radians $\rightarrow$ 0.2 radians.	18	2.0
Distance to nearest track < 0.3 radians $\rightarrow$ 0.4 radians.	19	-4.7
π^0 corrections are halved	20	2.5
DVCS $\rightarrow$ Single γ Monte Carlo	21	-3.9
Use Monte Carlo to extract signal instead of data	22	± 15.4

Table 8.1:

The effect each systematic check has on the cross section. The numbers refer to the axes of the figure and the abbreviation 'res' refers to the resolution of the measurement in question.

A summary of the systematic errors is shown in figure 8.2. In figures 8.3, 8.5, 8.4 and 8.6, the effects of the systematic errors are shown in bins of E_T^γ, $E_T^{\rm jet}$, η^γ and $\eta^{\rm jet}$ respectively. In the plots, the final systematic error is shown as positive: however this error is applied as a plus or minus error.

As in the inclusive case, the systematic check which uses HERWIG in place of PYTHIA is recorded, but not shown on the cross section plots. The HERWIG prediction does not follow the data well. The overall error on the cross section is found by adding the results of all the systematic errors in quadrature, then adding the systematic errors to the statistical errors in quadrature in the relevant bin of the relevant variable.

8.3 Cross Sections

The cross sections are calculated and unfolded using the same method as for the inclusive process – that is, equation 7.1 – and the same formula also holds for the cross sections with respect to $E_T^{\rm jet}$ and $\eta^{\rm jet}$. As in the inclusive case, the statistical error is calculated using equation 7.2 and added in quadrature to the calculated systematic errors.

The cross sections for the photon plus jet process cover an inclusive photoproduction sample from which an isolated photon in the energy range $5\leq E_T^\gamma \leq 15\,$GeV and pseudorapidity range $-0.7\leq \eta^\gamma \leq 0.9$, and one and only one jet in the energy range $6< E_T^{\rm jet} <17\,$GeV and the pseudorapidity range $-1.5 < \eta^{\rm jet} < 1.8$ is required. The photoproduction cuts and isolation criteria are as detailed in chapter 5.

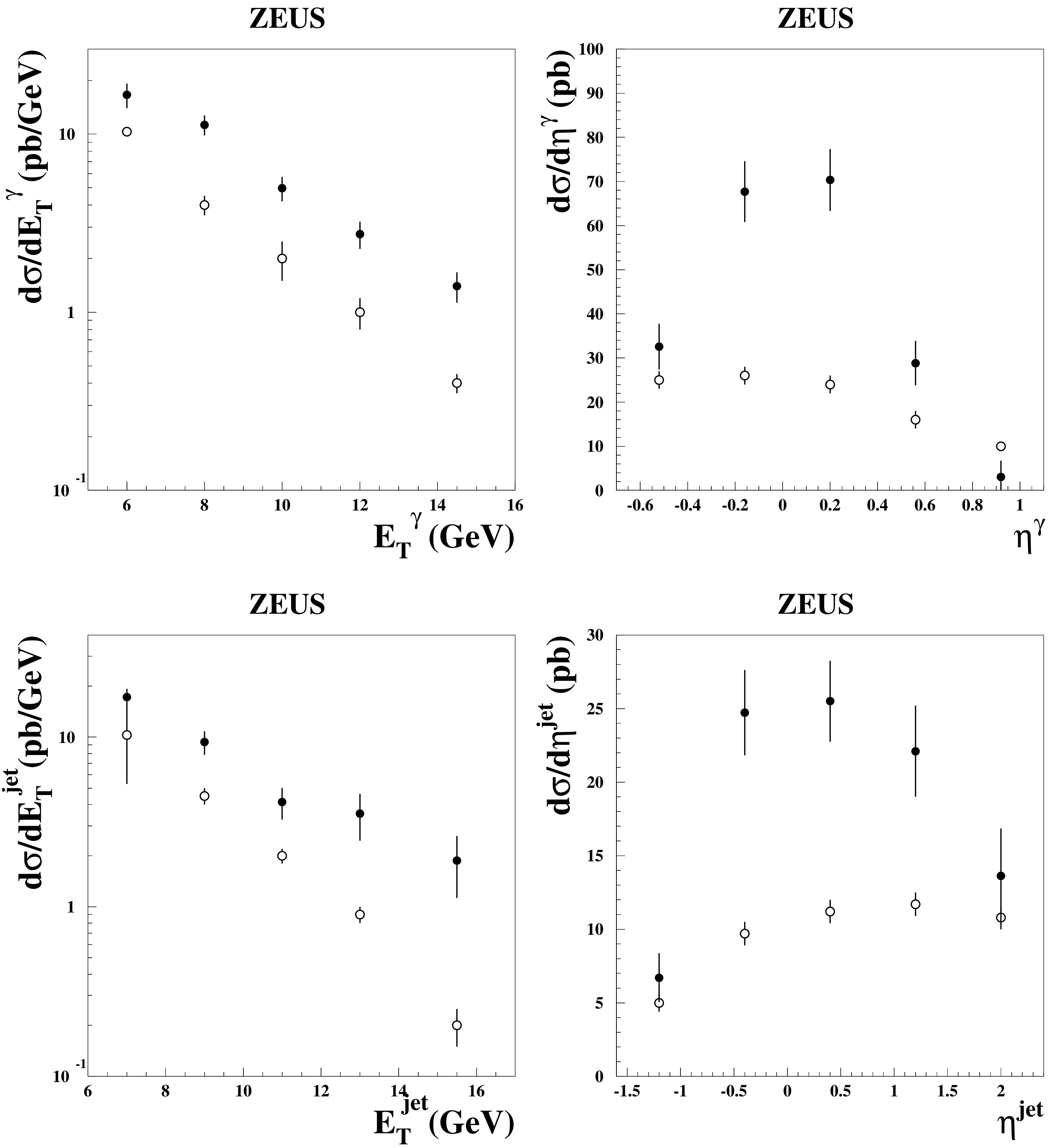

Figure 8.7: The top two plots show the cross sections for the photon plus jet process with respect to the photon variables, and the bottom two plots are the jet variables. In both cases, the dijet analysis method is shown in the open circles and the closed circles represent the results of the shower shape analysis method. The data represented are from 99-00 HERA running only.

8.4 Comparisons to the dijet method

The event selection used in the dijet method is described in section 5.12. For the purposes of comparison, the analysis using the shower shape method is modified slightly to match the cuts of the dijet analysis. The comparison is performed using only 99-00 HERA data. The changes made to the cuts in the shower shape analysis are as follows.

- The y_{JB} was measured in the range $0.2 < y_{JB} < 0.8$.
- The photon pseudorapidity range was increased to $-0.7 < \eta^{\gamma} < 1.1$
- The jet pseudorapidity range was substantially increased to $-1.6 < \eta^{\text{jet}} < 2.4$

The comparison between the dijet method and the shower shape method described in this thesis is shown in figure 8.7. The results show some surprising discrepancies between the two analysis methods. The shower shape analysis tends to lie above the dijet method rather than below, as would be the case if the dijet method's inability to effectively remove the background from π^0 mesons was to blame for the discrepancies. This may be an indication of depleted signal in certain areas where the BMIPS cut is less effective. There is good agreement in the lowest E_T^{γ} bin, where the contribution from neutral mesons is highest.

It is likely that using the BPRE to remove the background based on the conversion probability of the photon tends to vary in its effectiveness with E_T^{γ}. If that is in fact the case then it may be that more of the good signal events are removed by that cut at higher E_T^{γ}, which may account for some of the differences. However, if this is true then one of the most promising aspects of the analysis, the possibility of measuring to higher-E_T^{γ} where the statistics limit the effectiveness of the shower shape subtraction, would require considerable further work to remove this problem.

The agreement in η^{γ} and $\eta^{\rm jet}$ is reasonable in the first and last bins for both variables. However the shower shape analysis shows an excess compared to the dijet analysis in the central region.

8.5 Comparisons to Monte Carlo samples

The cross sections are presented in figures 8.8, 8.9, 8.10, and 8.11, the figures showing the cross section with respect to E_T^{γ}, η^{γ}, $E_T^{\rm jet}$ and $\eta^{\rm jet}$ respectively. All four are compared to PYTHIA and HERWIG, where the solid red histogram represents PYTHIA and the blue dashed histogram shows the HERWIG distribution.

Although the artificial weighting described in section 4.4.3 is applied to the HERWIG distribution, the agreement between HERWIG and the data is still poor. PYTHIA, on the other hand, maintains a reasonable agreement with the data regardless of the jet requirement. In fact, the agreement between the data and PYTHIA is noticeably better compared to the comparisons made by previous ZEUS prompt photon analyses, almost certainly due to using a newer version of PYTHIA. It would appear that while HERWIG provides a reasonable picture of the event structure, as seen by the good agreement in the control plots, it does not provide a good description of the photon plus jet process. η^{γ}, in particular, is poorly modelled by HERWIG.

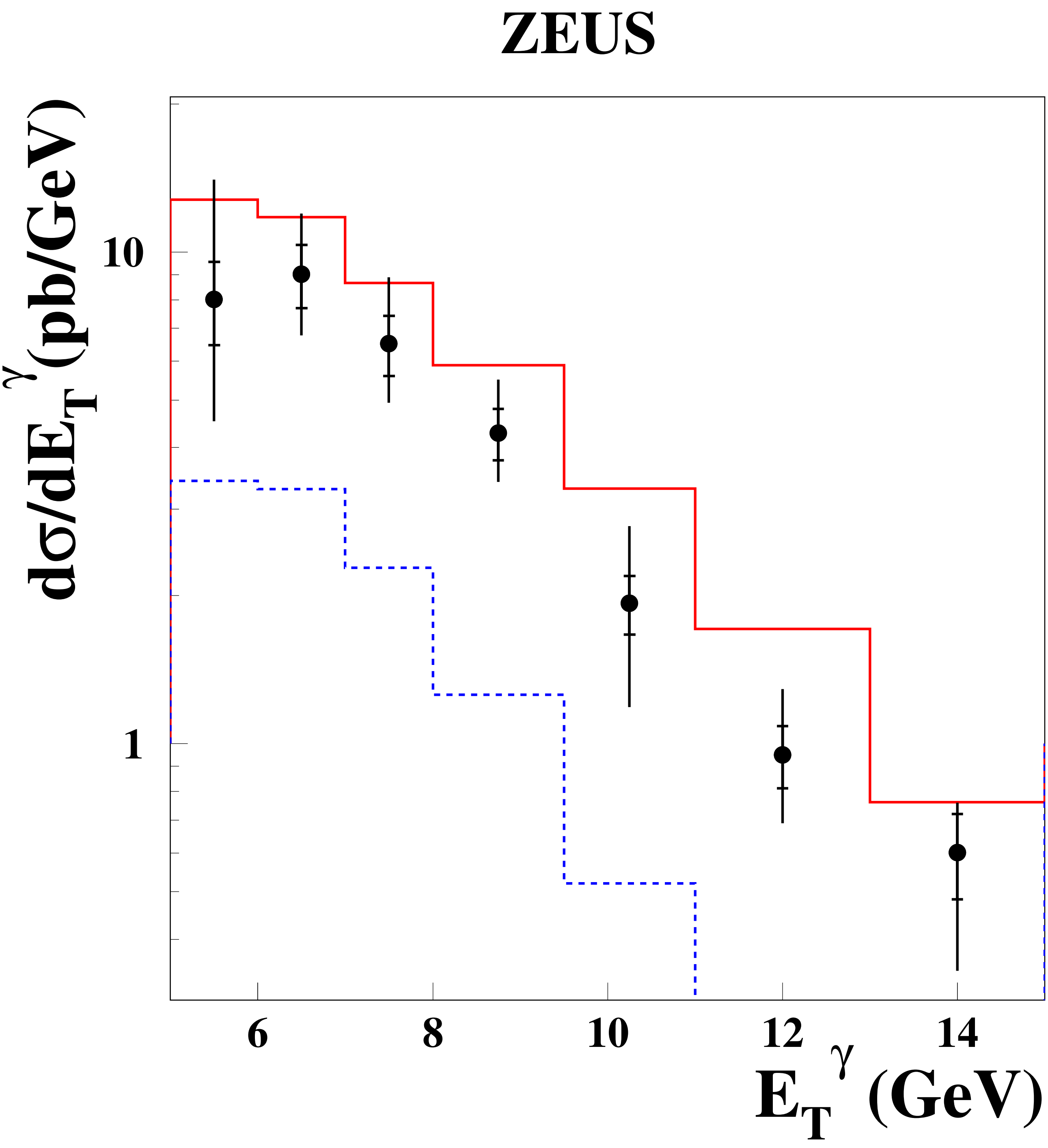

Figure 8.8: The cross section with respect to E_T^{γ}, compared to the PYTHIA (full, red line) and HERWIG (blue, dashed) simulations. The inner error bars show the statistical errors, while the outer bars show the systematic uncertainties.

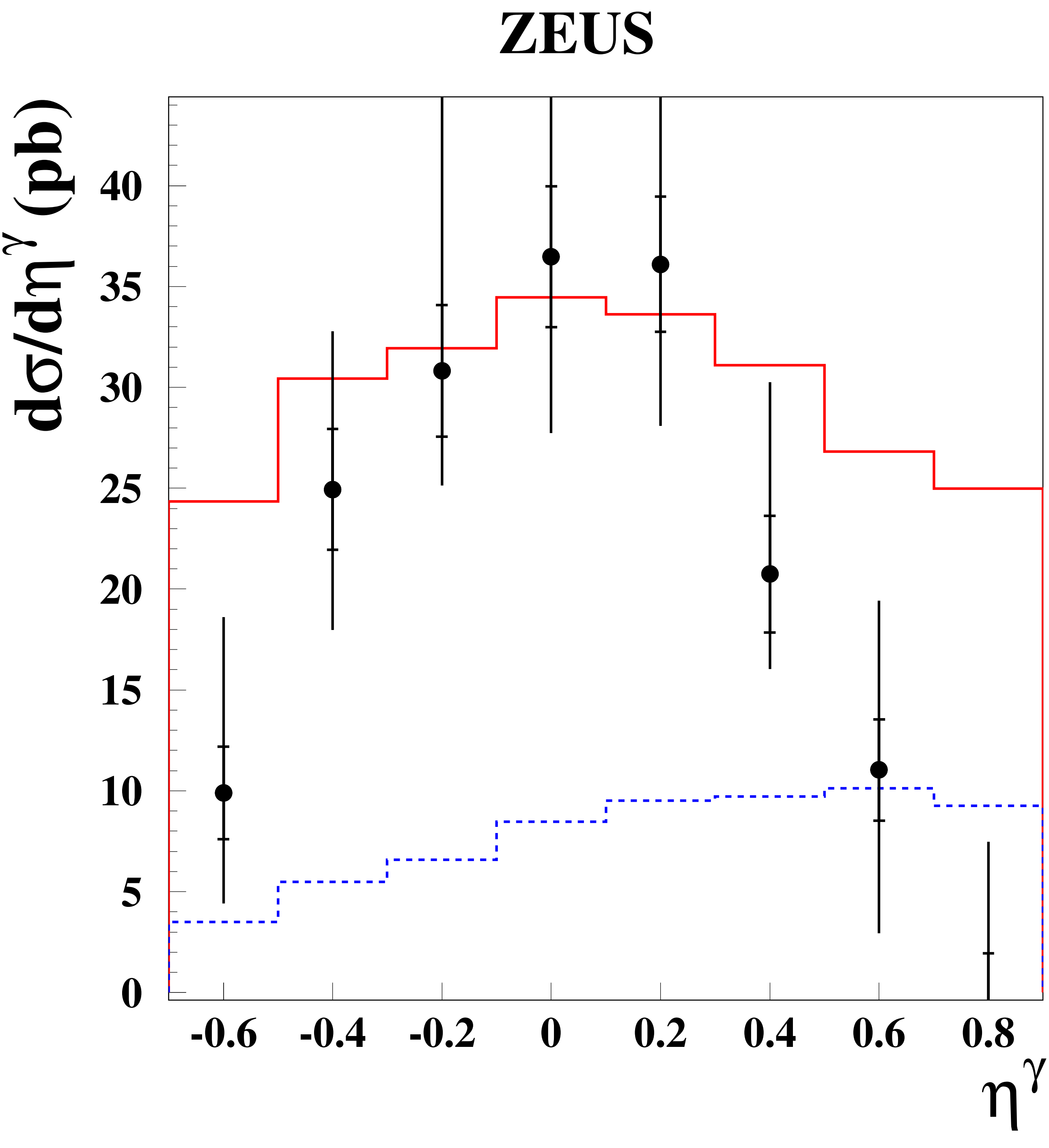

Figure 8.9: The cross section with respect to η^{γ}, compared to the PYTHIA (full, red line) and HERWIG (blue, dashed) simulations. The inner error bars show the statistical errors, while the outer bars show the systematic uncertainties.

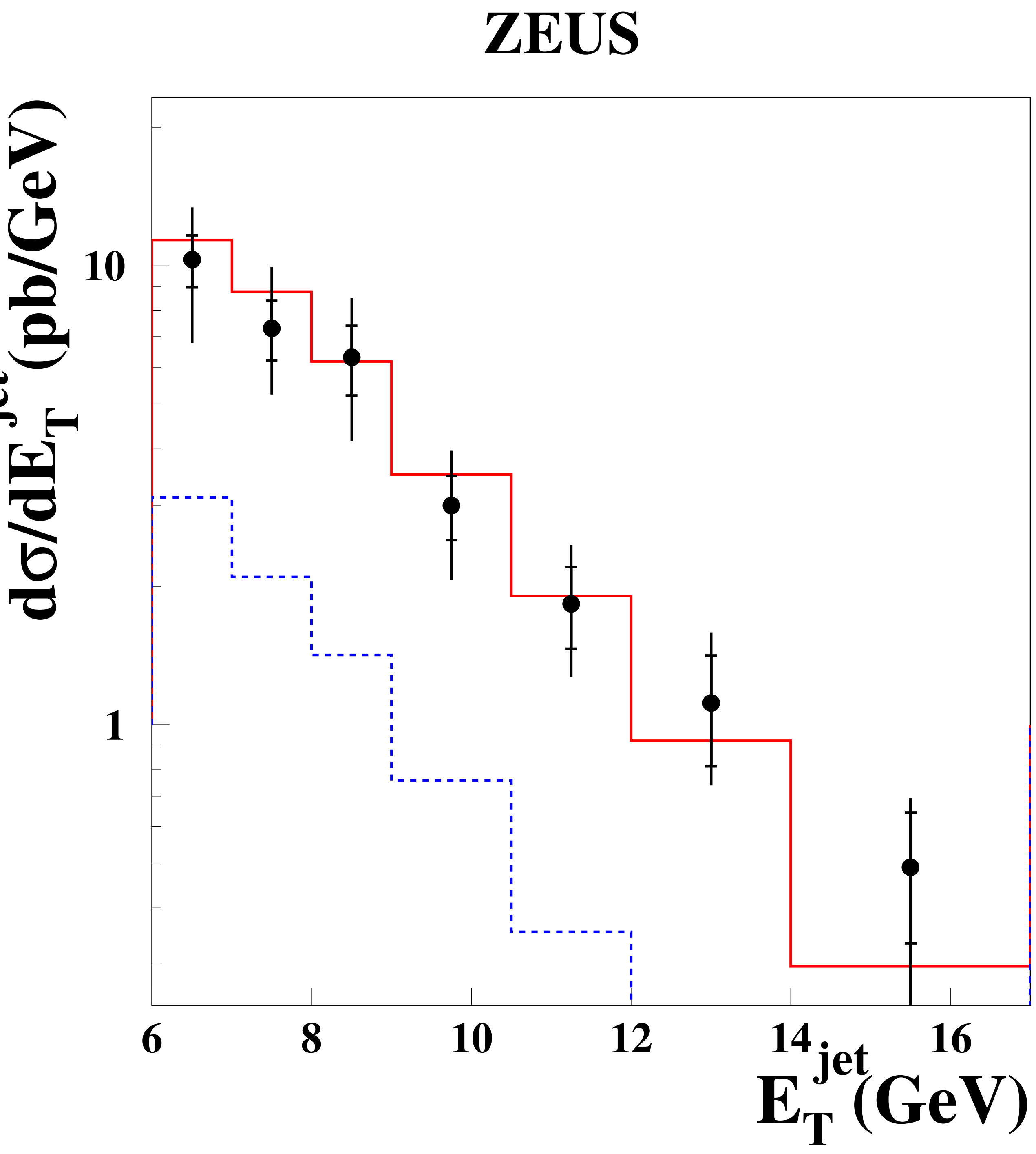

Figure 8.10: The cross section with respect to E_T^{jet}, compared to the PYTHIA (full, red line) and HERWIG (blue, dashed) simulations. The inner error bars show the statistical errors, while the outer bars show the systematic uncertainties.

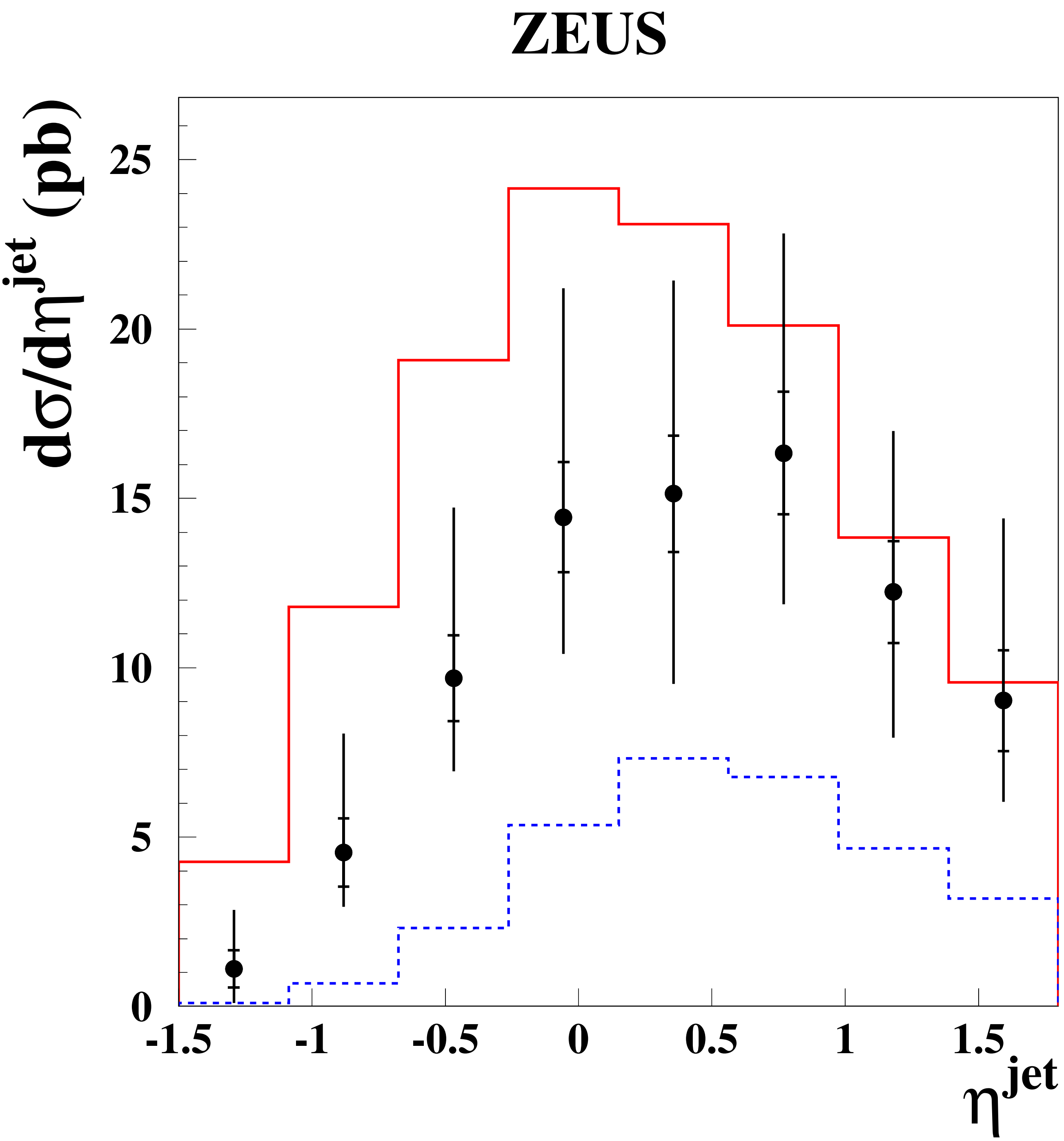

Figure 8.11: The cross section with respect to $\eta^{\rm jet}$, compared to the PYTHIA (full, red line) and HERWIG (blue, dashed) simulations. The inner error bars show the statistical errors, while the outer bars show the systematic uncertainties.

Chapter 9

Conclusions

Prompt photons in photoproduction have been measured at the ZEUS experiment at HERA. Cross sections have been produced for both the inclusive and the photon plus jet processes, using the full HERA I dataset, providing increased luminosity and hence improved precision in the measurement.

The new use of DVCS photons in place of the single particle Monte Carlo provides a much improved confidence in the evaluation of the photon signal and the background, both directly, since it is now possible to use the signature of real photons in the background subtraction process, and indirectly, in that the comparison between the single particle Monte Carlo and the DVCS for the photons allows for a correction of the distributions for the π^0 and η Monte Carlo samples.

9.1 Inclusive prompt photons

9.1.1 Comparison to the 96-97 analysis

For the inclusive prompt photon process, cross sections are unfolded with respect to E_T^γ and η^γ, yielding $d\sigma/dE_T^\gamma$ and $d\sigma/d\eta^\gamma$. Comparisons are made to the previous results for E_T^γ, both using the 96-97 subsample and using the full 96-00 dataset.

In the limited 96-97 dataset, the agreement between the current analysis and the previous analysis is reasonable, both in order of magnitude and in the general shape of the distribution. The agreement is best at higher-E_T^γ, where the background from neutral mesons is less significant, showing an effect from the improved shower shape evaluation.

When the sample is increased to the full 96-00 luminosity, the shape of the distribution remains in agreement with the previous analysis, although there is a noticeable increase in the observed cross section. This is likely to be due to the increased proton-beam energy used at HERA after 1998.

9.1.2 Comparison to the Monte Carlo samples

The unfolded cross sections are also compared to Monte Carlo samples from the PYTHIA and HERWIG event generators.

PYTHIA provides a good fit to the data in both E_T^γ and η^γ, a fit, in fact, that is somewhat improved since the previous published analysis, particularly in η^γ, where the older version of PYTHIA failed to reproduce the data in the backward region of the calorimeter.

HERWIG does not provide a good fit to the data. Control plots show a good description of the underlying event kinematics, however the photon is not well-modelled at the event stage. The cross section with respect to E_T^γ shows reasonable agreement with the data, and, in fact, provides a slightly better agreement than PYTHIA for high-E_T^γ. However, in both shape and magnitude, there is little agreement between HERWIG and data in the η^γ distribution.

9.2 The photon plus jet process

Four cross sections are measured for the photon plus jet process; $d\sigma/dE_T^\gamma$ and $d\sigma/d\eta^\gamma$ are unfolded as for the inclusive process, while $d\sigma/dE_T^{\rm jet}$ and $d\sigma/d\eta^{\rm jet}$ are presented for the first time at ZEUS.

As in the inclusive case, the photon plus jet process makes use of the DVCS photons in the background subtraction. Further, the suggestion of the new dijet method for measuring the prompt photon plus jet process has opened up new possibilities for extending the analysis.

9.2.1 Comparison to the dijet method

The dijet method of measuring prompt photons is a promising development. The shower shape method, by its nature, is restricted to where there are sufficient statistics to allow for an effective statistical subtraction of the background. The dijet method offers the possibility of measuring prompt photon signals in regions which have fewer event numbers, and the simpler method could allow for analysis on an event-by-event basis, which is not currently possible with the shower shape method.

A first comparison has been made between the two methods. An analysis of the method used to subtract the background concurred with a PYTHIA-based analysis by my ZEUS colleagues [1], showing that both signal and background are removed by the BMIPs cut, although the ratio of signal to background is enhanced after it is applied. It is acknowledged that the dijet method has no way of removing photons which originate from the decay of π^0 mesons from the sample.

The cross section comparison uses data from 99-00. In magnitude, the shower shape method lies consistently above the value for the dijet analysis, which is unexpected, since a contribution from π^0 mesons remains in the dijet sample. In shape, there is good agreement between the two methods in both E_T^γ and $E_T^{\rm jet}$, although in both η^γ and $\eta^{\rm jet}$ there is a considerable excess seen in the central region when the shower shape method is used. Agreement is seen in the lowest E_T bin for both the photon and the jet, and the far forward and far backward bins in η^γ and $\eta^{\rm jet}$ also display good agreement.

It appears clear that there are some substantial differences remaining between the two methods. However, this first comparison is very promising, and it may be possible to extend the prompt photon analysis in previously unexpected ways if the strengths of the new method are fully exploited.

9.2.2 Comparison to Monte Carlo samples

The results for the photon plus jet analysis are compared to PYTHIA and HERWIG samples, as in the inclusive case.

PYTHIA provides reasonable agreement with the resultant cross sections, although the data lie below PYTHIA predictions in the high-E_T^γ and the forward η^γ regions. The general shape of the jet variables is fairly well described.

HERWIG does not provide a good description of the data. At the control plot level, the $y_{\rm JB}$ and $Z_{\rm vtx}$ distributions are well-described by HERWIG. However, the agreement between the data and the HERWIG predictions is poor at both the event level and the cross section level for both the photon and the jet variables, with no significant agreement in either magnitude or shape. While the agreement is slightly improved by the use of a weighting factor in E_T^γ, the resulting prediction continues to fail to produce acceptable agreement. This is consistent with prior comparisons between data and HERWIG for prompt photon analyses.

9.3 Future Work

The success of the recent upgrade from HERA I to HERA II has opened up the possibility for a number of new analyses using the upgraded luminosity and the potential for polarisation. The ZEUS upgrade should also provide scope for further development in this field, with the new Micro-Vertex Detector providing the potential for measuring prompt photons with heavy flavour events if the event rate is high enough. Further, an integrated luminosity of several times the present figure should be available by the time HERA closes in 2007, so that the statistical precision on the present measurements can be significantly improved.

The dijet method is encouraging in its results, and although the agreement with the shower shape method is not perfect, with some refinement to the background subtraction process this new method may allow for new prompt photon processes to be studied, such as very high-E_T photons or photon plus dijet processes. The higher luminosity available from the full HERA I and HERA II dataset should further aid any studies in this direction.

Prompt photon studies continue to be important, both for their contribution to our understanding of QCD and as a background process to such events as the Higgs two-photon decay channel, of particular interest when the LHC comes online.

It is anticipated that this is a field that will continue to yield rich results.

Appendix A

Solving the HERA background problems

A.1 Introduction

Over the period of 2001 - 2002, the HERA ring and the experiments there underwent a major luminosity upgrade. Data taking was resumed in April 2002. However, the level of background events was much higher than was expected. This had the potential to be a very serious barrier to resuming physics data-taking. Therefore, the long-awaited data from HERA II - that is, post-upgrade HERA - was not immediately forthcoming. There are many areas of physics in both ZEUS and H1 which depend on the new data, either for luminosity reasons or because the new components or the polarised lepton beam were vital to the analysis.

Further, the detectors themselves were not designed to withstand large quantities of radiation over extended time scales, and the luminosity upgrade was not designed to have a large impact on radiation dosage. In actuality, the large radiation dosage could severely shorten the lifetimes of certain crucial detector components - most notably, the Central Tracking Detector

(CTD) and the new Micro Vertex Detector (MVD). These components often had to be switched off or worked at low efficiencies in order to protect them from long term damage.

During these problems, it was necessary that work was done to allow normal physics data-taking to be resumed [33]. The author, alongside the rest of the CTD team, played a substantial part in this work, and some of the CTD analysis is documented here.

A.2 The background problem

Preliminary analysis indicated that there were three main components to the background problems:

- Synchrotron radiation
- Off-momentum positrons
- Proton background.

The proton background was thought to display fixed-target like properties: it appeared that the beam was impacting on something in the beampipe. Detailed studies into the new conditions would have to be made in order that the necessary steps could be taken to resolve the problems.

The detectors available for studying to background condition were the MVD, the C5 counters, the trigger system, and the CTD. The tools were not yet available to study the effects, and had to be developed from scratch.

It was essential that the experiments used to study the background did not also contribute to the damage being suffered by key components, especially the CTD. By studying the currents in the chamber as they relate to the beam currents, any possible damage could be quantified.

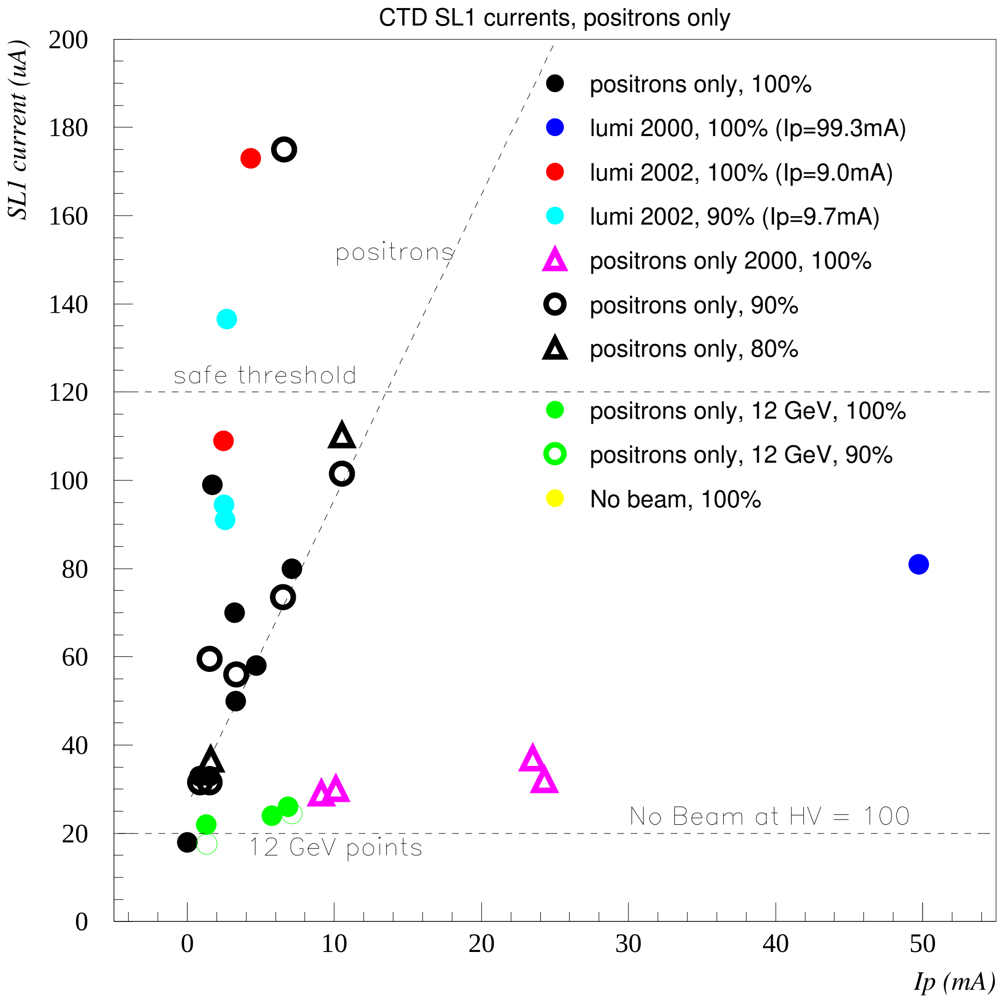

Figure A.1: This plot is from August 2002. The x axis displays the positron only beam current in mA. The y axis shows the current in the CTD chamber. The general trend of the black points shows that the chamber currents are rising far too steeply with respect to the beam currents, so that the safe threshold for running the CTD is reached at only 15mA of positron current. The design current after the upgrade was to be 50mA. The percentages quoted refer to the high voltage setting of the CTD.

Figure A.1, displays for the period from August 2002, how the CTD responded to the background conditions. The two horizontal lines show the chamber currents in superlayer one with no beam current, and the threshold current for safe long term operation. The black points are the data points taken with positrons only since the upgrade. The pink triangles show the same data, but from pre-upgrade runs. The green points are post-upgrade, but running with positrons at injection energy - that is, at 12 GeV. The percentages shown in the key refer to the percentage of the previous high voltage value at which the CTD was running when the points were taken.

The best-fitting straight line through the pre-upgrade points is much shallower than the post-upgrade line, which is displayed on the chart. This indicates that running with small beam currents was now producing large chamber currents in the CTD. It could therefore be inferred that running with positrons at higher currents would bring the chamber currents above the safe threshold for long-term running and would almost certainly cause long-term damage to the detector. At the point at which the graph was produced, many points lay on the line, but the only points that lay below it were taken with either the CTD high voltage at less than 100 % or with the beam energy at less than the usual 27.5 GeV. This fact limited the amount of work that could be done with the CTD at high positron beam currents.

A.3 Analysis of the background

Due to the new and unusual features that were associated with the high background, it was necessary to examine as much data as possible. Some of the most prominent features are demonstrated in Figure A.2, which dates from June 2002, early in the study of the background problems. The structure of the plots provided an excellent overall summary of the important feature recorded by the CTD in each run.

The information in the top three plots is predominantly of technical interest, and can therefore be ignored in this context.

In the centre row, the first two plots show the variation with z of the number of events. From the strong peak in the $-z$ direction, it seems clear that much of the activity is concentrated here. Note also that this run used a random trigger, by which it can be seen that overall, most of the hits in the CTD are likely to occur in this region. The third plot in this row is the drift time, as measured by the z-by-timing system of the CTD. The main features of the drift time can be more clearly seen by the FADC system due to a much finer digitisation. However, this plot is useful for de-bugging purposes.

In the third row, the first plot shows the ϕ distribution. This shows a double-peaked structure. Further investigation of this structure showed that it is was concentrated in the rear direction and in the first superlayer, that is, near the beampipe.

The final two plots in the third row show the drift time as measured by the FADC system of the CTD. The two vertical lines are situated firstly at the time of the bunch crossing - or the t_0 - and at one bunch crossing later. Initial examination shows that although there is a small peak at the t_0, there is a large peak at about 60ns later. Physics plots, on the other hand, show a large peak at the t_0. This indicated that there was a large delayed component to the background. The drift time structure will be examined further in section A.4.2.

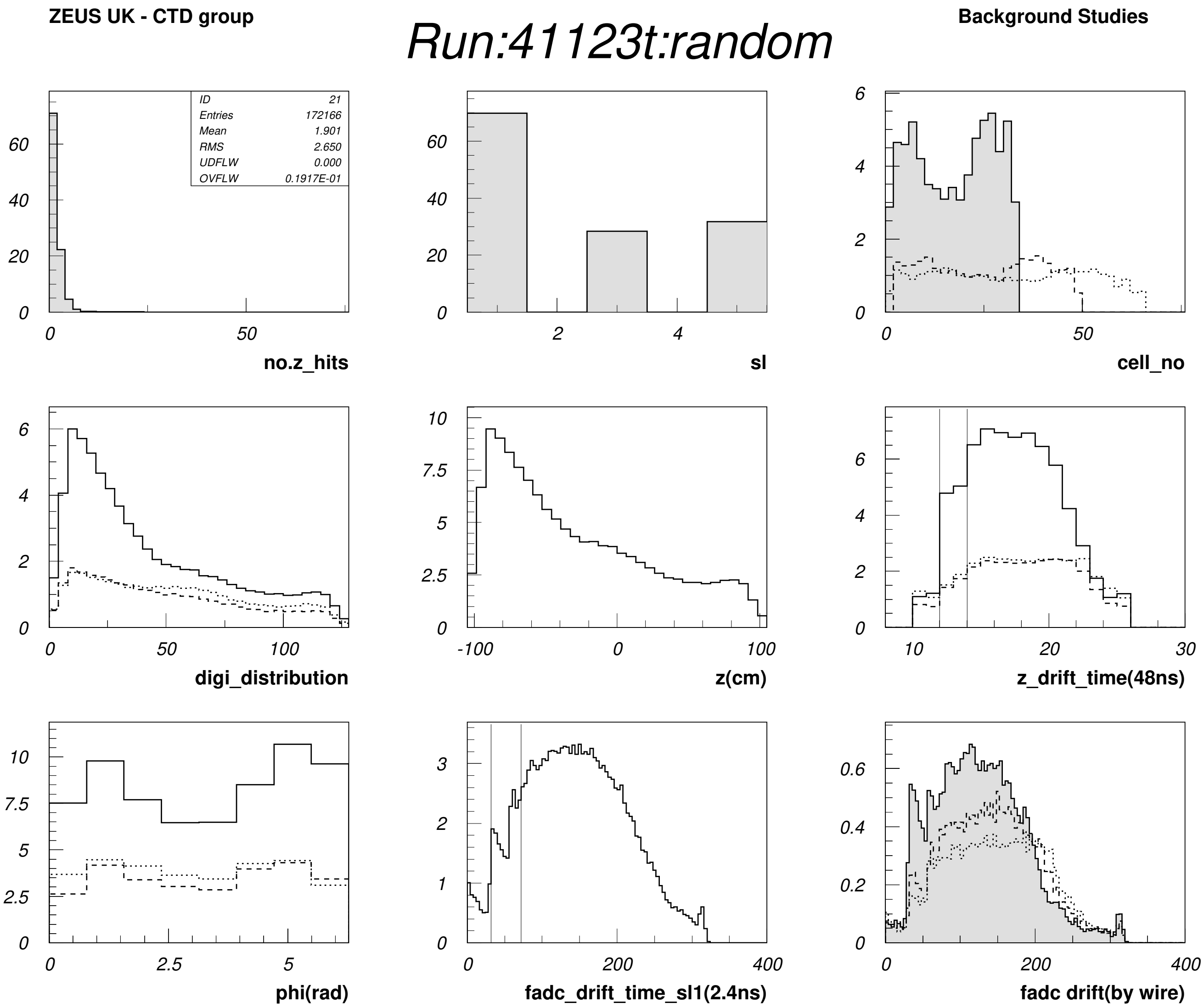

Figure A.2: The modified summary plot from June 2002. From left to right and top to bottom, the plots are as follows. Row 1: The number of hits in the z system, the hits in superlayers 1, 3 and 5, the number of hits in each cell of the CTD. Row 2: The digi distribution in superlayers 1, 3, and 5, the z distribution and the z-by-timing drift time. Row 3: The ϕ hit distribution, the FADC drift time in superlayer 1, and the FADC drift time in wires 1, 4, and 7.

A.4 Forming hypotheses

A.4.1 Random and track trigger structures

The trigger system provided a very useful method to separate different backgrounds and to estimate their respective contributions to the observed effect. Two trigger configurations used frequently to study the background are here referred to as ‘random’ and ‘track’ triggers.

The random trigger uses only a random number selection to reduce the volume of events, and therefore should not introduce any bias into the detector. That is, the random trigger should display what is happening in the detector in the majority of events, and no particular pattern is expected. On the other hand, the track trigger looks for events that have a clear track in the detector, introducing a bias towards events that contain a charged particle. The track trigger was used to look specifically at the behaviour of the particle background, while the random triggered events were dominated by synchrotron radiation. The differences are demonstrated in figure A.3.

The first plot shows the ϕ distribution. While for random runs there are slight peaks around $\phi = 0$, the predominant feature is undoubtedly the double-peaks in the up and down directions. In track runs, the peak around $\phi = 0$ (that is, in the $+x$ direction) is the most prominent feature. This may indicate a contribution from off-momentum positrons in that direction.

For the z distributions, both types of runs show large peaks in the rear z. However, the random run drops off sharply, whereas the track run shows a less sharp fall-off. In both cases, the peak is explained by considering that synchrotron radiation is being reflected into the rear of the detector.

In the drift time, the random run and track runs are entirely different shapes - the random run does not have the large in-time peak which dominates the track drift time. This is expected

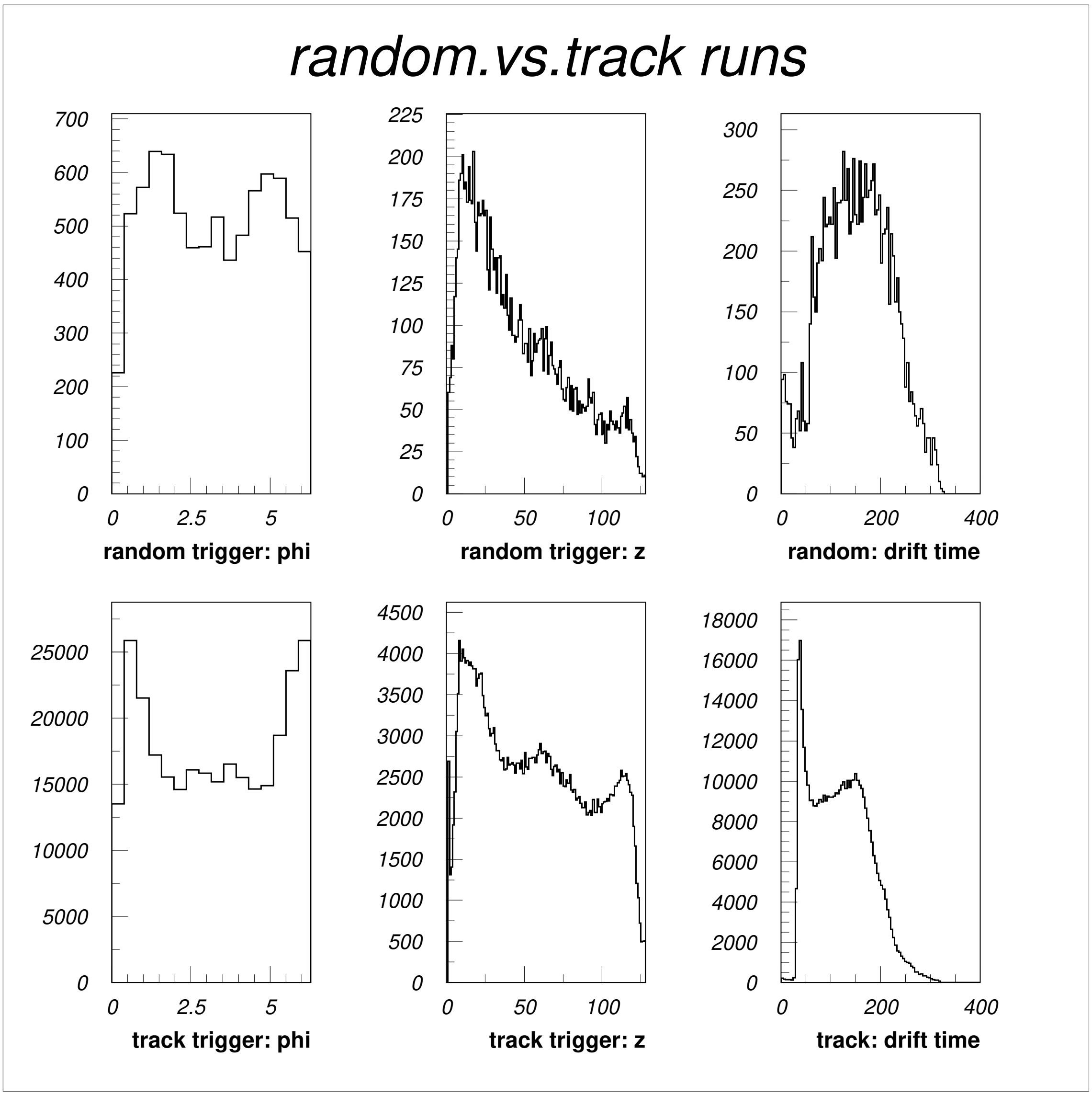

Figure A.3: The difference between random and track triggered runs. The top three plots show the ϕ, z and drift time for random runs. Below are the same quantities in a track run. The figure is explained more fully in the text.

due to the way the drift chamber measures tracks compared to individual hits. The individual hits should be evenly spaced throughout the event, whereas the nature of tracks introduces a large component at the t_0.

A.4.2 The FADC drift time

The FADC system in the CTD provides detailed timing information for each event, in steps of 9.6 ns. This provides a valuable measure of the origin of the hits in that event. Figure A.4 shows the different drift time plots for two similar random-triggered runs from June 2002. The top plot, run 41123, displays a direct component at the t_0, and a further delayed component between 60 and 70 ns later. The bottom plot shows no direct component, while the delayed peak is still obvious. Differences in the two plots are likely to be due to different beam tunings.

The timing of the delayed peak indicates that the radiation must be originating at or around the absorber at -11m. Later runs displayed components at different times, and it can therefore be inferred that there are components from other absorbers and collimators further down the beampipe.

This information is crucial. By observing the timing of the synchrotron radiation component, an estimation of the source of the reflected radiation could be made, providing a clear method of combating this problem.

A.4.3 The energy steps experiment

One of the biggest problems in identifying the background was investigating precisely which features occurred due to radiation effects, and which were related to the positron and proton particle backgrounds. Although different trigger configurations gave a good indication, the results inferred from this should be confirmed if possible.

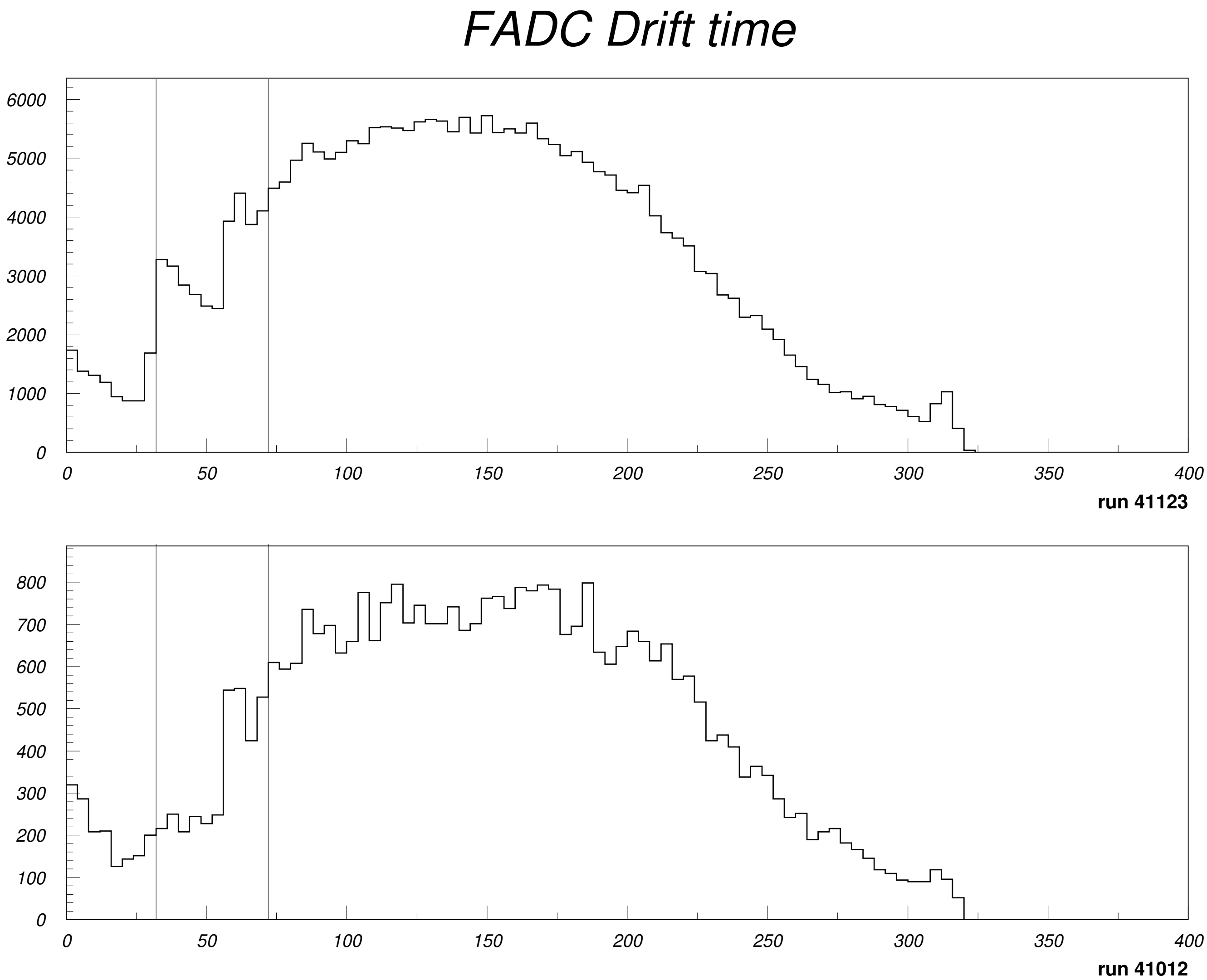

Figure A.4: The FADC drift time. Above, run 41123, has a direct and delayed component. Below, run 41012 shows only the delayed component. The x axes are in ns, the y axes show the number of hits at each time. The two vertical lines indicate the t_0 and one bunch crossing later.

One way to achieve this was by examining the different features at different beam energies. It is known that the intensity of synchrotron radiation varies as the fourth power of the beam energy, that is E^4. Particle background, however, displays only a linear dependence on energy. It should therefore be possible to compare the plots at increasing energies, as synchrotron radiation background becomes more dominant.

An experiment was therefore set up to allow runs to be taken at approximately the same current, but at different energies. This was originally performed with only positrons in the machine, and that is what is examined here. This can be seen in figure A.5.

The energy was stepped from positron injection energy of 12.0 GeV, to 15.3 GeV, 18.1 GeV, 21.9 GeV, 24.0 GeV, up to the full energy of 27.5 GeV.

When the summary plot was produced for these runs, it became obvious that there were two main steps in energy where certain features became prominent. At 12 GeV, the z and ϕ distributions are essentially flat, and the drift time spectrum shows almost entirely in time components. the picture is almost identical at 15 GeV, although the drift time shows a slightly higher plateau. The first step occurs at 18 GeV, where the peak that has been seen in the rear direction in z shows clearly. The downward peak in ϕ also becomes prominent, although the other peak in the up direction is not there. In the drift time spectrum, there is still a substantial in-time component, however, there is also some delayed. 21 GeV shows a very similar picture. The next step occurs at 24 GeV. At this energy, there are peaks in the up and the down direction in ϕ, and the drift time spectrum is dominated by delayed components. The picture at 24 GeV looks very similar to that at 27 GeV.

The conclusions from this experiment broadly agree with those seen from the trigger comparisons, i.e. that the synchrotron radiation is the dominant source of background, predominately seen in the strong delayed component in the drift time distribution, and that the particle back-

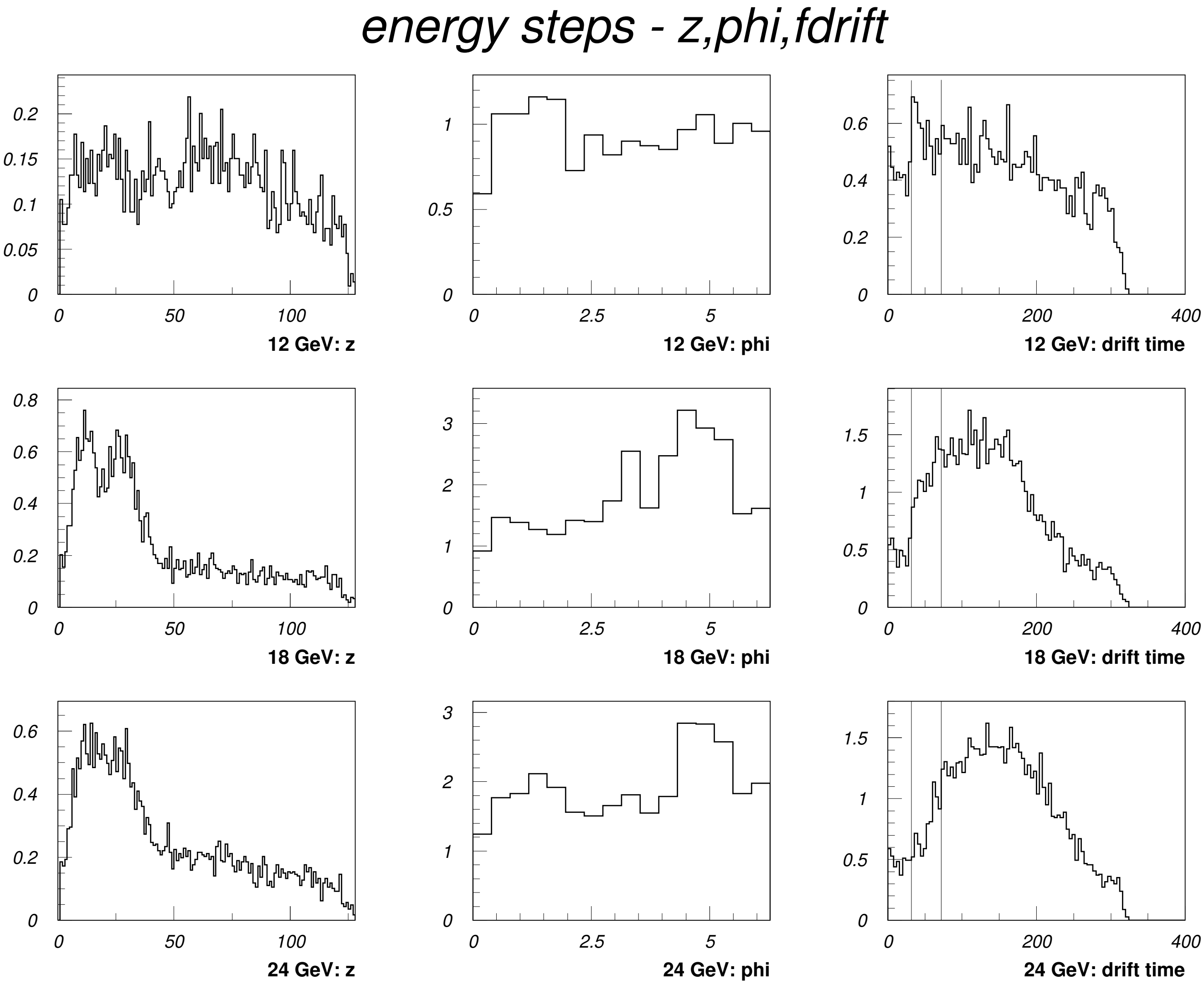

Figure A.5: The changes seen at steps in beam energy. Displayed are plots for, from top to bottom, 12, 18 and 24 GeV, and, from left to right, z, ϕ and FADC drift time. It is clear that, in z, the peak develops at around 18 GeV, with a double-peaked structure that vanishes at 27 GeV. In ϕ, the downward peak (on the left) develops at 18 GeV, but the upwards peak is not visible until 24 GeV. In the drift time, most of the contribution is in-time (that is, occurs at t_0) until 24 GeV, when the delayed contribution becomes more noticeable. As the beam energy increases, the contribution from background due to synchrotron radiation also increases, therefore it is likely that features which become important at higher beam energies are due to the synchrotron radiation component of the background.

ground tends to form the in-time component but is apparently not restricted to one section of the detector. The effect on the chamber current is shown in figure A.6, which is discussed more fully in section A.4.4.

A.4.4 The lead experiment

As previously mentioned, the large number of hits due to synchrotron radiation was causing a large increase in the sense current of the CTD. Previous plots had given the locations with the highest concentration of these hits to be in the $-z$ direction and upwards and downwards in ϕ. It should therefore be possible to shield many of these areas from the excess radiation.

Two sheets of lead were thus inserted into the detector, resting on the beampipe. It was postulated that the lead should absorb some of the hits, allowing higher positron beam currents without risking the CTD. The position of the lead, extending from -40cm to -100cm in z, well away from the nominal z vertex position, should mean that the lead would not interfere with normal physics events.

Figure A.6 shows the difference in the CTD chamber currents including points with the lead and the points from the energy ramping experiment. It is directly comparable with figure A.1, although it should be noted that the lines are purely to guide the eye. The points relating to the lead experiment, at the top of the charts in red, show a substantial decrease from the projected value, in quadrant 2.

Figure A.7 shows that there is a clear difference in the number of hits in ϕ before and after the lead was inserted. Further investigation revealed that the effect was, indeed, much more prominent in the rear direction in z, and upwards in ϕ, exactly where it was expected.

To support this data, there were some calculations done by other members of the background team. The first calculation assumed that the CTD currents were affected by two sources of

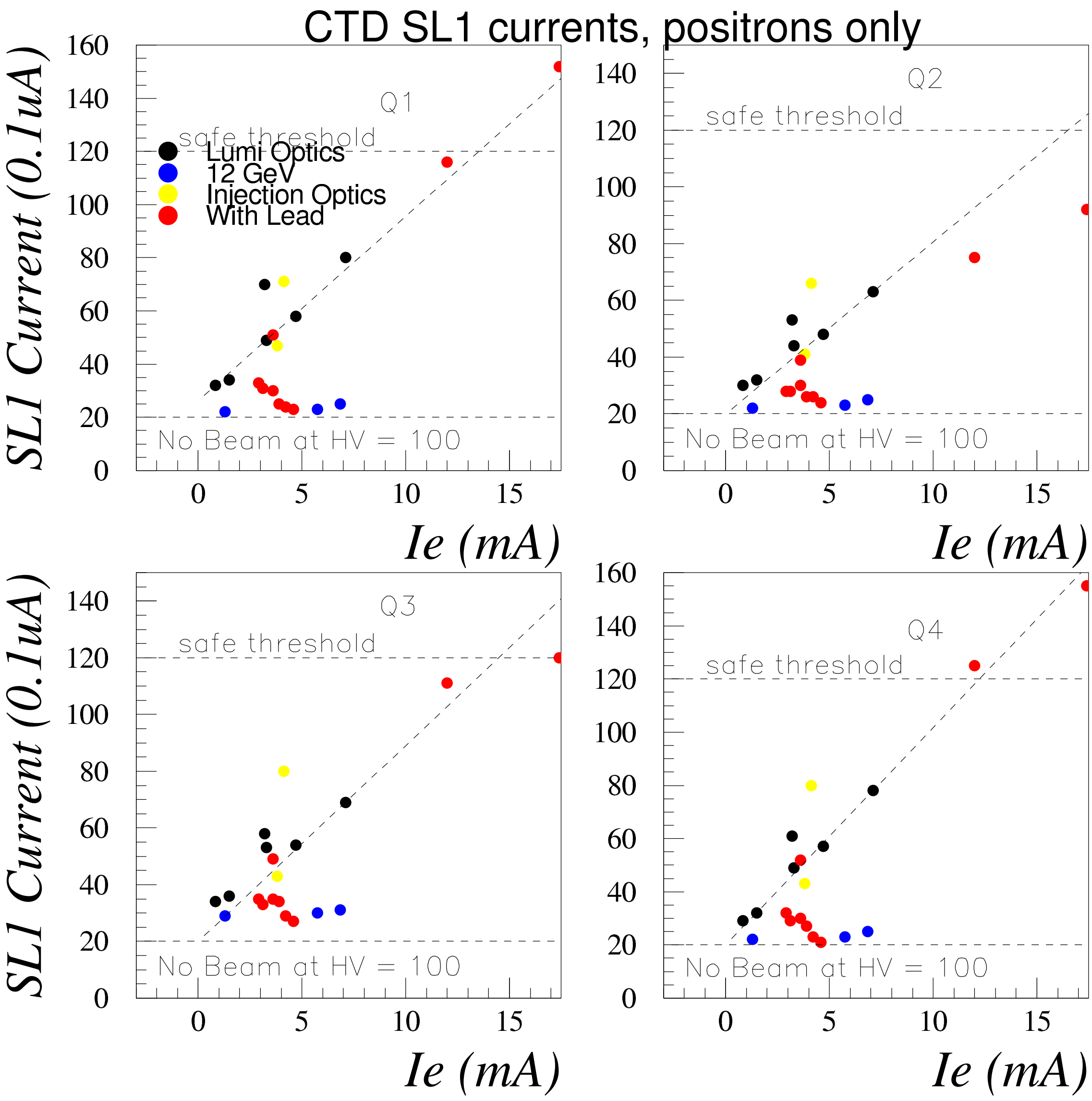

Figure A.6: The same plot as in figure A.1. The four plots represent the values for the four high voltage quadrants in ϕ. The red points at the top of the charts show the new values for the CTD chamber current once the lead is in place, and the most significant deviation from the projected line is, as expected, in quadrant 2. The cluster of red points at the bottom are from the energy steps experiment, with the energy increasing from right to left – notice that the beam current decreases during the course of the experiment.

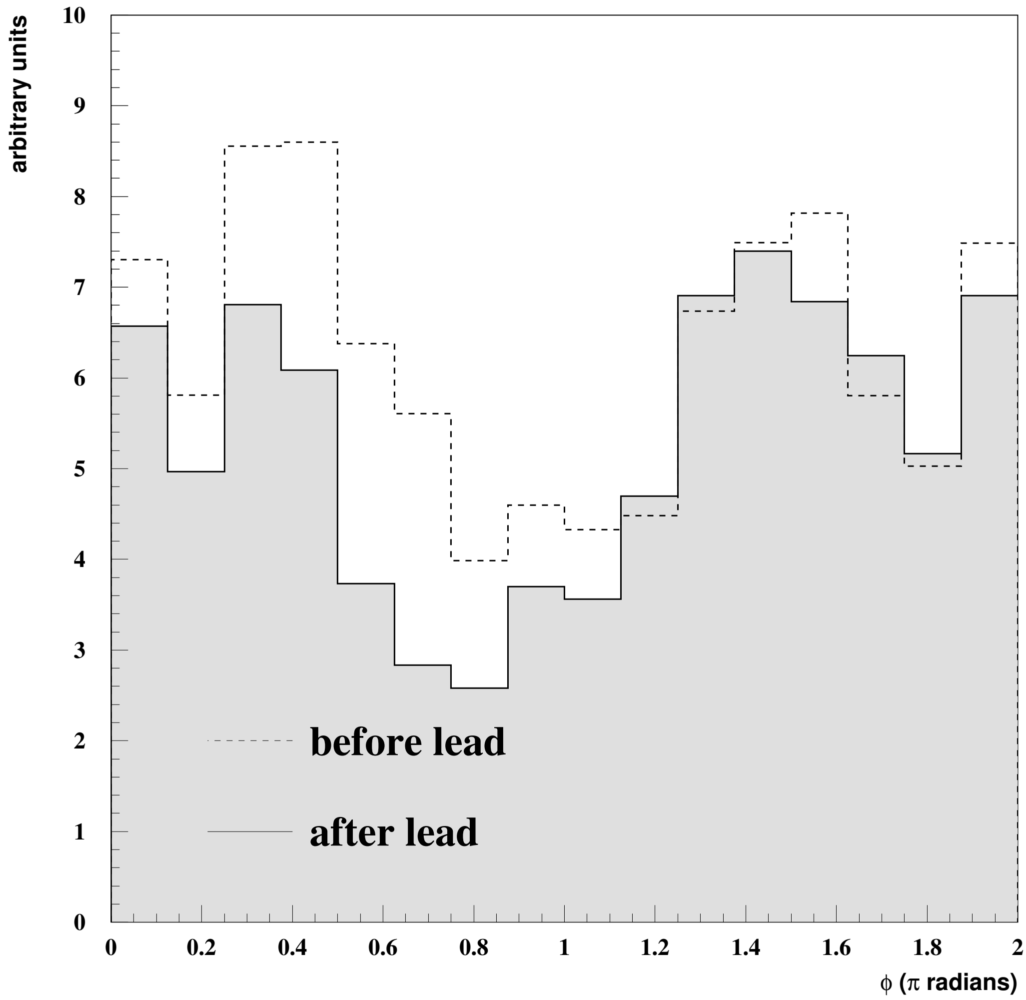

Figure A.7: Comparing the ϕ distribution before and after the insertion of the lead strips. The x axis gives the ϕ distribution in radians, the y axis the number of hits, normalised per 100 events. There was a further factor of 0.7 introduced to allow comparison – once the lead was introduced the total number of hits per event increased, an observation which is unrelated to the insertion of the lead. However, while there is almost no difference seen between the peak in the down direction, in the upwards direction, where the shielding was placed, there is a significant decrease. This peak in ϕ corresponds to the second high-voltage quadrant in figure A.6

background, radiation and particle. Data from before the lead was inserted was fitted into an equation derived from this assumption, to give the proportionality constants. This revealed that the lead was having an effect on the CTD currents of the order of 20%, which is too small to show up on the chart. The second calculation was from an in-depth simulation. This revealed that the lead was not covering a large enough area of the beampipe to make a substantial difference to the CTD currents. It was suggested that if the lead could be modified from lead sheets to a lead pipe, covering all ϕ, then the number of photons entering the rear of the CTD could be reduced by an order of magnitude. However, the sheet of lead served its purpose by protecting the CTD while background studies continued, and the insertion of a full lead pipe was not deemed necessary when other, more direct solution became apparent.

A.5 Solutions

By the methods described in previous sections, it is clear that there were, as hypothesised, three components to the background problem; synchrotron radiation, off-momentum positrons, and scattered proton background. A large proportion of the background was from synchrotron radiation. Investigation aided by simulation had confirmed two sources of unwanted synchrotron radiation which could be reduced.

Photons generated by the acceleration of the positron beam were being reflected by the absorber at -11m, and by striking the C5A collimator at $z = -1.7$m. They were then scattered into the rear of the detector. Since there was also a possible path between the C5A and the C5C collimators at $z = -0.8$m, photons were not prevented from entering the detector after reflection from the -11m absorber. The same flaws in the collimator and absorber system contributed to the particle background.

Both of these problems could be dealt with if careful modifications to the collimator structure were made. These modifications were shown by simulation to reduce the observed synchrotron radiation background by an order of magnitude. The main modifications suggested were:

- Close the hole between the C5a and C5c collimators by re-designing the C5a collimator to include a shield.

- Reduce the radiation reflected from the -11m absorber by coating it in thin layers of copper, gold, silver, and nickel to reduce diffusion.

- Insert a new moveable vertical collimator at -3.6m to come between the -11m absorber and the C5 collimators.

At the same time, several studies were carried out into the operation of the CTD, investigating whether the sensitivity of the chamber to high backgrounds could be lessened without causing long-term damage to the detector, and further without lowering the efficiency of the detector for physics analyses. During the continuation of the background studies, the CTD high voltage was lowered to 95% of its previous value, allowing the chamber to be used in beam conditions which were not optimal with minimum damage to the detector.

During a long shutdown in 2002-2003 the above modifications were carried out. The coating of the -11m absorber was not completed on time, and so was never used.

It was expected that further improvements could be made to the background by careful attention to the vacuum conditions in the beampipe, which improve with running time, and by careful beam tuning. To this end, new background monitors were designed providing the accelerator physicists with accurate information about the background conditions in the machine, whether they originate from the lepton or the proton beam and a comparison to predictions depending on the beam currents. This new monitor uses data from the C5 counter and the tracking detectors, and has been very successful in assisting the HERA crew to provide the required level of beam tuning. Such tools also indicate to the ZEUS crew the best time to turn on essential detector components, such as the CTD, without causing damage.

Since the end of the shutdown in July 2003 to May 2004, HERA has provided 41.35pb^{-1} luminosity, of which ZEUS has gated 18.06pb^{-1}. There has also been much progress in polarised lepton beam data, and HERA has provided electron beam luminosity since the autumn of 2004. The progress of the background post-shutdown is demonstrated in figure A.8, and has continued to improve since this plot was produced.

The background problems were unexpected and required a great deal of time and effort from a large number of people. The two colliding beam experiments and HERA provided people to study the problems and fully understand them, and there was some consultations with experts from other experiments to ensure that nothing was missed. With a huge concerted effort the problems were overcome, and have allowed HERA, ZEUS and H1 to continue taking data successfully.

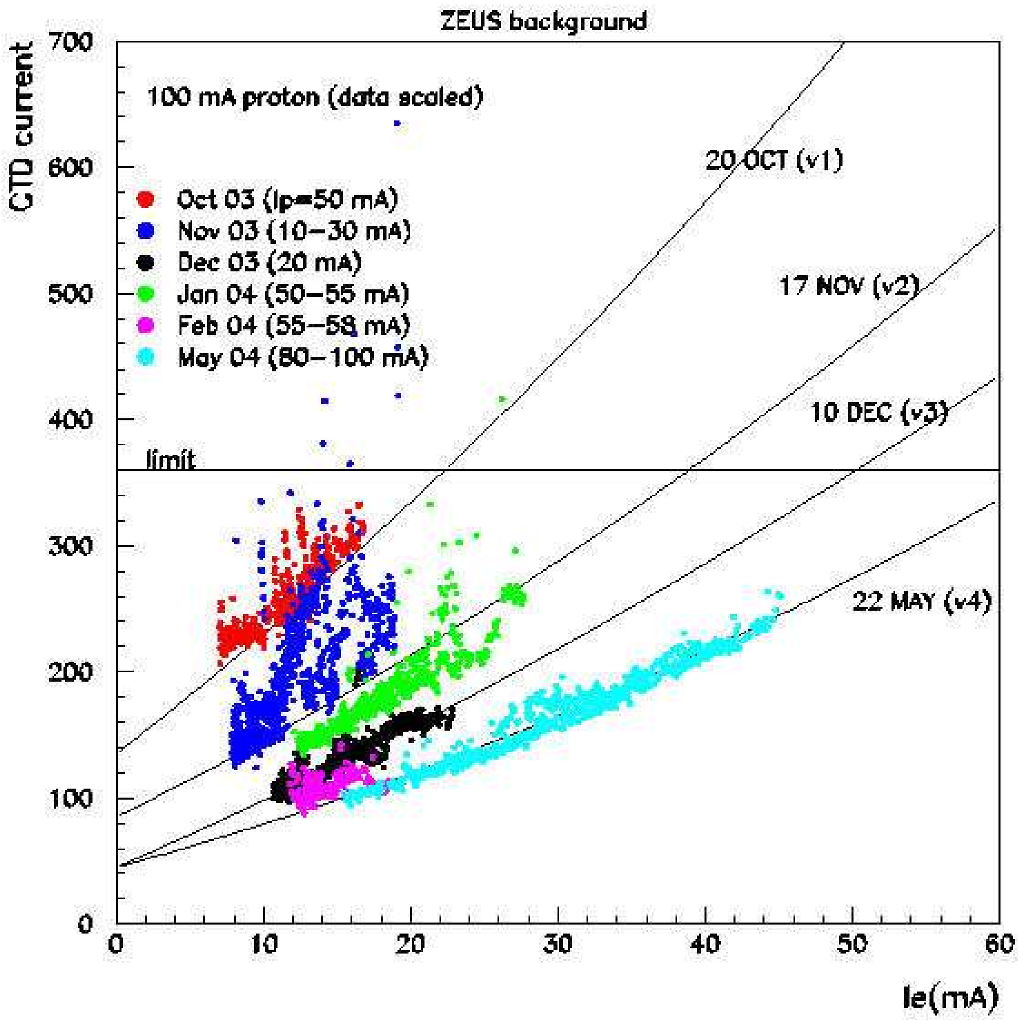

Figure A.8: The currents in the CTD are shown on the x-axis with the positron beam current on the y-axis. With the beginning of post-shutdown running, the currents generated by the CTD are already much improved. Continuous running with high luminosity improves the beam gas background from impure vacuum, and the improvement during the 2003-May 2004 running period is noticeable, bringing the resultant CTD current back within safe limits.

Appendix B

The π^0 correction

As described in subsection 6.6.2, after the comparison between single photon Monte Carlo and true photon data in the form of DVCS photons became available it became clear that a correction factor was necessary to bring the standard of the single π^0 and η distributions into line with the DVCS photons [34].

The algebra leading to the form of the correction is reproduced here in two stages.

B.1 The simplistic approach

The simplistic approach to the necessary correction follows a straightforward line of reasoning. It is clear that there is a necessity for correcting the π^0 and η distributions. In the case of the $f_{\max}$ plots, it is reasonable to treat π^0 and η mesons in the same way, since the application of the $\langle \delta Z \rangle < 0.65$ cut reduces the contribution from η-mesons with a wider decay-angle than π^0s. For simplicity, then, the correction method refers only to π^0 mesons, although the method is applied to both π^0- and η-mesons.

The simplistic approach is not used in the analysis, but it provides useful background as to the development of the more complicated approach which was actually used.

Assume that there are three main components to the π^0 contribution.

- Single photon like. These are mainly found in the $f_{\max} > 0.75$ region.

- Two photon like. These are clearly background and are mainly found in the $f_{\max} < 0.75$ region.

- Tail to single photon like. In this case it is less clear that the photons originate from a π^0. Such events are also in the $f_{\max} < 0.75$ region.

The correction will be necessary predominately for the third type, and should therefore be applied in the lower- $f_{\max}$ region.

The method is as follows.

Let n_+ be the number of events in a sample with $f_{\max} > 0.75$ and n_- be the number of events with $f_{\max} < 0.75$. Then we can define r such that $r = n_-/n_+$. This may be defined for all the single particle Monte Carlo samples, so we have r_γ, r_{π^0} and r_η, where r_γ may be split into r_γ^{MC} and r_γ^{DVCS}.

Since $r_\gamma^{\mathrm{MC}} \neq r_\gamma^{\mathrm{DVCS}}$, it is necessary to correct r_γ^{MC} by an amount δ, such that

$$r_\gamma^{\mathrm{MC}} = r_\gamma^{\mathrm{DVCS}} + \delta$$

Since the correction is applied only to n_-, we can then cross-multiply by n_+^γ (which is the same for Monte Carlo and DVCS photons) to get:

$$n_-^{\mathrm{MC}} = n_-^{\mathrm{DVCS}} + \delta n_+^\gamma$$

We can then assume that the necessary correction to $n_-^{\pi^0}$ will be $\delta n_+^{\pi^0}$.

B.2 The more rigorous approach

While the simplistic approach appears reasonable, there are one or two problems with the method. Most notably, the simplistic method will alter the total number of events measured rather than simply the ratio of poor to good events in f_{max}. A more rigorous approach is therefore required.

As in the simplistic method, r is defined as n_-/n_+ for each single particle sample. Consider first the case of single photon samples. We can say that $n_-^{\mathrm{MC}} = rn_+^{\mathrm{MC}}$ It follows that some correction to r is required such that

$$n_-^{\mathrm{true}} = r^{\mathrm{corr}} n_+^{\mathrm{true}} \tag{B.1}$$

Now,

$$\begin{aligned} n^{\mathrm{tot}} &= n_-^{\mathrm{MC}} + n_+^{\mathrm{MC}} \\ &= rn_+^{\mathrm{MC}} + n_+^{\mathrm{MC}} \\ &= (1+r)n_+^{\mathrm{MC}} \end{aligned} \tag{B.2}$$

and

$$\begin{aligned} n^{\mathrm{tot}} &= n_-^{\mathrm{MC}} + \tfrac{n_-^{\mathrm{MC}}}{r} \\ &= (1+\tfrac{1}{r})n_-^{\mathrm{MC}} \\ &= (\tfrac{r+1}{r})n_-^{\mathrm{MC}} \end{aligned} \tag{B.3}$$

From B.2, we have

$$n_+^{\mathrm{MC}} = \frac{n^{\mathrm{tot}}}{1+r} \tag{B.4}$$

and from B.3

$$n_-^{\mathrm{MC}} = \frac{rn^{\mathrm{tot}}}{1+r} \tag{B.5}$$

We can now define δ such that $r^{\text{corr}} = r + \delta$. From this and from equation B.1 it is clear that

$$n_-^{\text{corr}} = n_-^{\text{true}} = r^{\text{corr}} n_+^{\text{true}} = n_+^{\text{true}}(r+\delta)$$

By B.5, we see that

$$n_-^{\text{corr}} = \frac{n^{\text{tot}} r^{\text{corr}}}{1 + r^{\text{corr}}} = \frac{(r+\delta) n^{\text{tot}}}{1 + r + \delta}$$

and, using B.4, we therefore get

$$n_-^{\text{corr}} = \frac{n_+^{\text{MC}}(r+\delta)(1+r)}{1+r+\delta}$$

Also from B.4, we see that

$$n_+^{\text{corr}} = \frac{n^{\text{tot}}}{1+r+\delta} = \frac{n_+^{\text{MC}}(1+r)}{1+r+\delta} \tag{B.6}$$

recalling equation B.2.

By performing the correction, a total number of events $n_+^{\text{MC}} - n_+^{\text{corr}}$ are transferred from the upper $f_{\max}$ region to the lower. Thus:

$$\begin{aligned} n_+^{\text{MC}} - n_+^{\text{corr}} &= n_+^{\text{MC}} - \frac{n_+^{\text{MC}}(1+r)}{1+r+\delta} \\ &= n_+^{\text{MC}} \left(1 - \frac{1+r}{1+r+\delta}\right) \\ &= \frac{\delta n_+^{\text{MC}}}{1+r+\delta} \end{aligned}$$

We now move from the case of single photons to the case of single mesons. In this case, low-$f_{\max}$ mesons introduce a longitudinal component n_L which is absent from the high-$f_{\max}$ sample. Thus

$$n_-^{\text{MC}} = r_\gamma n_+^{\text{MC}} + n_L \tag{B.7}$$

where r_γ is the quantity previously referred to as r in the single photon Monte Carlo case. We also define r_π^{MC} as the uncorrected value of r for the π^0 case. Manipulating equation B.7, it follows that

$$\begin{aligned} n_L &= n_-^{\mathrm{MC}} - r_\gamma n_+^{\mathrm{MC}} \\ &= r^{\mathrm{MC}} n_+^{\mathrm{MC}} - r_\gamma n_+^{\mathrm{MC}} \quad = n_+^{\mathrm{MC}}(r^{\mathrm{MC}} - r_\gamma) \end{aligned}$$

As in the case of photons, the correction process transfers a fraction of the n_+ sample into the n_- region. We can say that

$$\begin{aligned} n_-^{\mathrm{corr}} &= n_-^{\mathrm{MC}} + \tfrac{n_+^{\mathrm{MC}}\delta}{1+r+\delta} + n_L \\ &= r_\gamma n_+^{\mathrm{MC}} + \tfrac{n_+^{\mathrm{MC}}\delta}{1+r+\delta} + n_+^{\mathrm{MC}}(r^{\mathrm{MC}} - r_\gamma) \end{aligned} \tag{B.8}$$

and from equation B.6 it follows that

$$n_+^{\mathrm{corr}} = \frac{n_+^{\mathrm{MC}}(1+r_\gamma)}{1+r_\gamma+\delta} \tag{B.9}$$

By definition, $r^{\mathrm{corr}} = n_-^{\mathrm{corr}}/n_+^{\mathrm{corr}}$. Dividing equation B.8 by equation B.9 and cancelling, we get

$$r^{\mathrm{corr}} = r^{\mathrm{MC}} + \delta\frac{(1+r^{\mathrm{MC}})}{1+r_\gamma} \tag{B.10}$$

Equation B.10 is the correction which is applied.

References

[1] S. Chekanov, S. Magill, private communication, 2004.

[2] C. Gwenlan, *Jets and Energy Flow in Photoproduction using the ZEUS detector at HERA*. Ph.D. Thesis, University College London, London, UK, 2003.

[3] F. Halzen and A.D. Martin, *Quarks and Leptons: An Introductory Course in Modern Particle Physics*. John Wiley & Sons, Inc, 1984.

[4] R.P. Feynman, Phys. Rev. Lett. **23**, 1415 (1969).

[5] Yu.L. Dokshitzer et al., *Basics of Perturbative QCD*. Editions Frontieres, 1991;
T. Muta, *Foundations of Quantum ChromoDynamics*. World Scientific, 1998.

[6] ZEUS Coll., J. Breitweg et al., Phys. Lett. **B 472**, 175 (2000);
ZEUS Coll., J. Breitweg et al., Phys. Lett. **B 413**, 201 (1997).

[7] H1 Coll., Aktas, A. et al., Eur. Phys. J. **C38**, 437 (2005).

[8] ZEUS Coll., S. Chekanov et al., Phys. Lett. **B 511**, 19 (2001).

[9] ZEUS Coll., S. Chekanov et al., Phys. Lett. **B 595**, 86 (2004);
M. Bell, *Prompt Photon Production in Deep Inelastic Scattering at HERA*. Ph.D. Thesis, Glasgow University, Glasgow, UK, 2003;

M.S. Bell,J. Hamilton, and D.H. Saxon, *Observation of isolated high-E_T photons in deep inelasic scattering* (unpublished). ZEUS-Note-03-014, 2003.

[10] D0 Coll., B. Abbott et al., Phys. Rev. Lett. **84**, 2786 (2000);
D0 Coll., V.M. Abazov et al., Phys. Rev. Lett. **87**, 251805 (2001).

[11] R. McNulty, Preprint hep-ex/0406069, 2004;
CDF Coll., F. Abe et al., Phys. Rev. **D57**, 67 (1998).

[12] CDF Coll., D. Acosta et al., Phys. Rev. **D65**, 112003 (2002).

[13] CDF Coll., D. Acosta et al., Preprint hep-ex/0404022, 2004.

[14] ZEUS Coll., U. Holm (ed.), *The ZEUS Detector*. Status Report (unpublished), DESY (1993), available on `http://www-zeus.desy.de/bluebook/bluebook.html`.

[15] A. Bamberger et al., Nucl. Inst. Meth. **A 382**, 419 (1996).

[16] J. Andruszków et al., Acta Phys. Pol. **B 32**, 2025 (2001);
S.D. Paganis, Preprint hep-ex/0011080, 2000. Talk at *9^{th} Int. Conf. on Calorimetry in Particle Physics, Annecy, France, Oct. 2000.*

[17] N. Harnew et al., Nucl. Inst. Meth. **A 279**, 290 (1989);
B. Foster et al., Nucl. Phys. Proc. Suppl. **B 32**, 181 (1993);
B. Foster et al., Nucl. Inst. Meth. **A 338**, 254 (1994).

[18] M. Derrick et al., Nucl. Inst. Meth. **A 309**, 77 (1991);
A. Andresen et al., Nucl. Inst. Meth. **A 309**, 101 (1991);
A. Caldwell et al., Nucl. Inst. Meth. **A 321**, 356 (1992);
A. Bernstein et al., Nucl. Inst. Meth. **A 336**, 23 (1993).

[19] T. Sjöstrand, PYTHIA 6.2 Physics and Manual, 2002. Hep-ph 0108264;
T. Sjöstrand, Comp. Phys. Comm. **39**, 347 (1986);
T. Sjöstrand and M. Bengtsson, Comp. Phys. Comm. **43**, 367 (1987).

[20] G. Corcella et al., Preprint hep-ph/0107071, 2001.

[21] Available on `http://www-zeus.desy.de/ZEUS_ONLY/analysis/Amadeus/index.html`.

[22] G.A. Schuler and T. Sjöstrand, Phys. Lett. **B 376**, 193 (1996).

[23] T. Sjöstrand, Comp. Phys. Comm. **82**, 74 (1994).

[24] Available on `http://www-zeus.desy.de/components/funnel/`.

[25] R. Brun et al., GEANT3, Technical Report CERN-DD/EE/84-1, CERN, 1987.

[26] Available on `http://www-zeus.desy.de/ZEUS_ONLY/analysis/zes/`.

[27] Available on `http://www-zeus.desy.de/zarah/programming/eaze/index.html`.

[28] Available on `http://www-zeus.desy.de/ZEUS_ONLY/analysis/orange/index.html`.

[29] S.Catani et al., Nucl. Phys. **B406**, 187 (1993).

[30] S.W. Lee, *Measurement of Prompt Photon photoproduction at HERA*. Ph.D. Thesis, Glasgow University, Glasgow, UK, 2000.

[31] S. Chekanov et al., Phys. Lett. **B 573**, 46 (2003).

[32] J. Hamilton, *Shower Shape Variables in Deeply Virtual Compton Scattering* (unpublished). ZEUS-Note-03-002, 2003.

[33] ZEUS Background Working Group, *Study of beam-induced backgrounds in the ZEUS detector from 2002 HERA running* (unpublished). ZEUS-Note-02-018, 2002;
ZEUS Background Working Group, *Addendum - Study of beam-induced backgrounds in the ZEUS detector from 2002 HERA running* (unpublished). ZEUS-Note-02-020, 2002;
ZEUS Background Working Group, *Addendum - Study of beam-induced backgrounds in the ZEUS detector from 2002 HERA running* (unpublished). ZEUS-Note-02-027, 2002.

[34] P.J. Bussey, D.H. Saxon, private communication, 2005.